2001

Active Control of Thermoacoustical Instabilities.

Daniel Ulises Campos-delgado
Louisiana State University and Agricultural & Mechanical College

INFORMATION TO USERS

This manuscript has been reproduced from the microfilm master. UMI films the text directly from the original or copy submitted. Thus, some thesis and dissertation copies are in typewriter face, while others may be from any type of computer printer.

The quality of this reproduction is dependent upon the quality of the copy submitted. Broken or indistinct print, colored or poor quality illustrations and photographs, print bleedthrough, substandard margins, and improper alignment can adversely affect reproduction.

In the unlikely event that the author did not send UMI a complete manuscript and there are missing pages, these will be noted. Also, if unauthorized copyright material had to be removed, a note will indicate the deletion.

Oversize materials (e.g., maps, drawings, charts) are reproduced by sectioning the original, beginning at the upper left-hand corner and continuing from left to right in equal sections with small overlaps.

Photographs included in the original manuscript have been reproduced xerographically in this copy. Higher quality 6" x 9" black and white photographic prints are available for any photographs or illustrations appearing in this copy for an additional charge. Contact UMI directly to order.

ProQuest Information and Learning
300 North Zeeb Road, Ann Arbor, MI 48106-1346 USA
800-521-0600

ACTIVE CONTROL OF THERMOACOUSTICAL INSTABILITIES

A Dissertation

Submitted to the Graduate Faculty of the
Louisiana State University and
Agricultural and Mechanical College
in partial fulfillment of the
requirements for the degree of
Doctor of Philosophy

in

The Department of Electrical and Computer Engineering

by
Daniel Campos-Delgado
B.S., Universidad Autonoma de San Luis Potosi, Mexico, 1996
M.S., Louisiana State University, 1999
May 2001

ACKNOWLEDGMENTS

First of all, I would like to thank my wife for all her encouragement throughout this five difficult years. I am especially grateful to my parents that always guide me for the path of excellence.

I would also like to express my gratitude to my advisor and teacher, Dr. Kemin Zhou, for his guidance and support during the development of this dissertation. Furthermore, I would like to thank Dr. Jorge Aravena for all his help during the process of my admission to Graduate Program of the Department.

I am thankful to Dr. Oliver Paschereit and Dr. Sumanta Acharya who trust me the development of active control strategies in their combustor test-rigs. Moreover, I want to thank everybody who was involved during the experimental testing, in particular Bruno Schuermans and Daniel Allgood.

In addition, I am very grateful to Dr. Peter Wolenski, Dr. Guoxiang Gu and Dr. Robert Downer for being on my doctoral committee.

I want also to acknowledge the financial support provided by CONACYT, ARO and AFOSR.

Finally but not the least, I want to thank my friend Paulo Mancilla for introducing me to the problem of thermoacoustic instabilities.

PREFACE

The control and analysis of thermoacoustic instabilities have been the topic chosen for my Ph.D. research. This dissertation presents some advancement in this field. In May of 1999, I started working in this area and right away caught my attention the possibilities that this field could offer for control applications. It also presented big challenges since this research field is usually adopted by graduate students with mechanical engineering background. In fact, control of thermoacoustic instabilities is a demanding field of work either for control or mechanical researchers since it requires the knowledge of both worlds. The control specialist needs to understand the physics behind the combustion process to be able to formulate viable control strategies for the system. On the other hand, the mechanical specialist needs to have a clear view of the control field and the general techniques based on abstract math to express the problem in a control framework.

Everything started from a collaboration with the Mechanical Engineering Department at LSU. This Department already had a group of students working in this area, with a huge emphasis in experimental work rather than theoretical development. The control strategies already applied for this group were very basic in terms of control complexity (phase-delay control), and a necessity of exploring more advanced techniques was evident.

By a lecture in Mechanical Department at LSU in November of 1999, I got in touch with the head of one of the research groups in the Thermo- and Aero- Dynamics Department of ABB Alstom Power Technology Research Center. His research group was investigating applications of $\mathcal{H}_\infty$ control in combustion chambers. A collaboration with this research center started in January of 2000. This collaboration

ended up with a research residency (May to August 2000), held at the Corporate Research Center of Alstom Power Ltd. (former ABB Alstom Power) in Baden, Switzerland. During this period of time, two active control strategies to suppress combustion instabilities were developed. These techniques were tested in a large-size gaseous fueled test-rig. First, a linear model based on experimental measurements was developed. $\mathcal{H}_\infty$ optimal control was used then in controllers synthesis. On the other hand, a controller whose parameters were optimized online was also investigated. An *evolution algorithm* performed this optimization process. In lab testing, both strategies were capable of attenuate effectively the pressure pulsations.

During the fall of 2000, the collaboration with the Mechanical Department at LSU continued. Acoustic and fuel modulation control were successfully implemented in a liquid fueled swirl stabilized combustor. It is important to mention that there were big differences between this setup and the test-rig used in the Alstom Power Research Center. One of them was the type of fuel used in the chamber and the geometry of the combustor. So, they were two completely different systems in terms of control. First, the tests for fuel modulation with automotive fuel injectors were carried out. Time domain identification was used to derive a linear model of the combustor. Model-based LQG and $\mathcal{H}_\infty$ Loop-Shaping controllers were tested with good attenuation factors. However, these techniques did not show clear improvements over classical phase-delay control. Next, acoustic control was investigated. This time, frequency domain techniques were used to develop the combustor model. LQG and $\mathcal{H}_\infty$ Loop-Shaping designs were tested again. Now, the improvements of the model-based techniques over a baseline phase-delay strategy were evident.

In summary, active control of thermoacoustic instabilities was successfully implemented in gaseous and liquid fueled combustors. The control methodology involved

mainly two steps: combustor modeling and controller synthesis. Linear identification techniques were used and they were able to capture the basics characteristic of the complex combustor system. So, optimal control strategies like LQG and $\mathcal{H}_\infty$ design were able to suppress the pressure pulsations inside of the combustion chamber effectively.

On the other hand, during the controller synthesis it was noticed that optimal control strategies could lead to unstable controllers. This is obviously not desirable in practical applications like this one. However, unstable controllers can sometimes be avoided by changing the parameters of the control synthesis algorithm. This point brought our attention to find a control methodology that could overcome this problem (strong stabilization), especially in the case of $\mathcal{H}_\infty$ design. Consequently, a new algorithm to design $\mathcal{H}_\infty$ controllers with strong stabilization capabilities was introduced.

Early in the spring of 2001, a new control setup (fuel modulation case) was suggested for the test-rig in the Mechanical Department at LSU. The objective of this modification was to investigate the importance of the location of the control actuator in the effectiveness of the active control algorithm. Thus the fuel control actuator was now focused on the region of major heat-release in the flame front. A preliminary study was carried out with simple phase-delay control. It was shown that with this new setup a large pressure attenuation could be attained with just a small percentage of control fuel.

TABLE OF CONTENTS

NOMENCLATURE

ARX	Auto Regression with eXtra inputs
ARMAX	Auto Regression Moving Average with eXtra inputs
CO	Carbon Monoxide
$H(s)$	transfer function
$\hat{H}(\omega)$	frequency response data
I_n	$n \times n$ identity matrix
K	controller
K_∞	controller resulting from $\mathcal{H}_\infty$ optimization
L	combustion chamber length
LQG	Linear Quadratic Gaussian
LFT	Linear Fractional Transformation
LTI	Linear Time Invariant
M	Mach number
NOx	Nitrogen Oxides
NRR	Noise Reduction Ratio
P	plant
PA	Peak Attenuation
$\mathcal{P}$	power
$Q_{primary}$	primary air flowrate
$Q_{secondary}$	secondary air flowrate
$\mathcal{R}$	field of real numbers
SISO	Single Input Single Output System
S_{uy}	cross-spectral density between u and y
S_{uu}	auto-spectral density of u
T	sampling period or evaluation time
T_a	air temperature
T_f	flame temperature
UHC	Unburned Hydro Carbons
c	speed of sound
cfm	cubic feet per minute

gph	gallons per hour
in	inches
p	pressure measurement
$\hat{p}$	Fourier Transform of p (frequency domain)
p_{mean}	mean pressure
p_{rms}	fluctuating pressure
q	heat release
q_c	control heat release
s	complex variable (continuous time)
$\hat{s}$	normalized complex variable s/ω_0
u	velocity of the flow or control signal
v_c	control signal
v_a	diaphragm velocity
v_b	burner velocity
w	white noise
z	complex variable (discrete time)
γ	ratio of specific heat capacities
λ	air/fuel ratio
ρ	density of the flow
ω	frequency (Hz)
ω_0	normalizing frequency
$\in$	belong to
$\bar{(\cdot)}$	mean value
$(\cdot)'$	oscillating component
A^T	transpose of A
A^{-1}	inverse of A
$Re\{\cdot\}$	real part of complex number
$\lambda(A)$	eigenvalue of A
$\sigma_i(A)$	ith singular value of A
$\left[\begin{array}{c\|c} A & B \\ \hline C & D \end{array}\right]$	shorthand for state space realization $C(sI - A)^{-1}B + D$
$\mathcal{F}_l(\cdot,\cdot)$	lower LFT
$\mathcal{F}_u(\cdot,\cdot)$	upper LFT

ABSTRACT

This dissertation presents some advances in active control of thermoacoustic instabilities in combustion chambers. Large-size gaseous and liquid fueled swirl stabilized combustors were used during the studies. Active control was implemented using different types of actuators. Proportional (loudspeakers and fuel valves) and discrete actuators (open-close automotive fuel injectors) were investigated. Acoustic and fuel modulation control were successfully applied.

In large-scale combustors, flame stabilization techniques such as swirl add three dimensional characteristics to the flow. Moreover, the induced turbulence creates highly nonlinear interactions in the system. Thus, in order to capture these characteristics nonlinear partial differential equations have to be used. Alternatively, the main dynamics of the combustion process can be modeled experimentally. This approach was chosen. Time and frequency domain linear identification techniques were used for this purpose. Several model-based control strategies such as LQG, $\mathcal{H}_\infty$ Disturbance Rejection and $\mathcal{H}_\infty$ Loop-Shaping techniques were tested experimentally with success. A simple controller whose parameters were optimized on-line is also introduced. An evolution algorithm was developed to perform its parameter optimization achieving good convergence to optimal values. The improvements with these proposed control techniques over classical phase-delay control are demonstrated experimentally.

A new control configuration was suggested from heat-release visualizations of the flame. In this new configuration, control actuation is directly focused onto the main area of heat-release in the flame front. Consequently, a more efficient actuation is

achieved. It is shown that with just a small amount of modulated fuel, phase-delay control can substantially attenuate the pressure oscillations.

Finally, during the development of $\mathcal{H}_\infty$ controllers, there were cases where the stability of the resulting controllers restricted the closed-loop performance. A control design strategy to solve the $\mathcal{H}_\infty$ Strong Stabilization problem is then presented. The proposed design strategy pursues to overcome the conservativeness of existing formulations. Examples show its potential for future applications.

CHAPTER 1

INTRODUCTION

The emission of pollutants is critical in modern combustion systems and strict regulations have been issued about this matter. The formation of pollutants such as NOx is largely dependent on the temperature profiles in the combustion process. On the other hand, it is desirable to operate the turbine at the highest permissible inlet temperature for high efficiency. Therefore, it is needed to have the highest allowable average temperature with the lowest possible maximum temperature, i.e. an homogeneous temperature distribution during combustion. For that purpose, a lean (in terms of stoichiometric balance) mixture between oxidizer (air) and fuel is required. However, a negative side effect is the increased combustion noise and the susceptibility to *thermoacoustic combustion instabilities.*

Thermoacoustic instabilities are created by interactions among fluctuations in acoustic pressure, velocity, heat release and the acoustic characteristics of the combustor and air supply, which can couple together and act as resonators. The first one to recognize this mechanism was Lord Rayleigh [62]. He observed that the effect of heat addition on the acoustic waves depends on the phase relationship. Consequently, if heat is added at the moment of highest pressure, the oscillations will be amplified. On the other hand, the oscillations will be damped if heat is added at the moment of lowest pressure or extracted at the moment of highest pressure.

Thermoacoustic instabilities in combustion chambers can lead to severe degradation of the combustion process, such as unacceptable noise pollution or even struc-

tural damage due to high pressure pulsations. These matters have received much attention of the research community. However, the complexity of the combustion process and the lack of suitable actuators make it a challenging problem.

The theory of combustion instabilities combines three main phenomena: acoustic properties, combustion interactions, and flame behavior. As a result, the three characteristics must be linked together in order to understand the origin of the instability coupling. Researchers have developed modeling techniques to describe the complex phenomena of thermoacoustic instabilities in simple setup systems. Culick in [17] reviewed the theoretical work in combustion instabilities applied to liquid-fueled propulsion systems. He explained the main mechanisms for combustion instabilities in these systems. In [8], Bloxsidge et al. developed a theoretical linear model to determine the frequency and mode shape of the instability and validate it by comparison with experimental data. A nonlinear combustor model was derived by Dowling in [19], where the acoustic dynamics are assumed to behave linearly and the heat release presents a nonlinear behavior which essentially 'saturates' according with the flow velocity. Similarly, Van Roon [73] derived a model based on acoustics coming from experimental measurements and on nonlinear burner and flame characteristics (saturation-like). He found that the reactants mixture does not arrive at the flame front at one specific time but over a distributed range of time (delay modeled). Peracchio and Proscia [61] presented a model whose instability agent is a fluctuating equivalent ratio. The acoustic pressure oscillations create a varying fuel/air ratio being delivered at the flame front which in return produces an oscillating heat release. This assertion was later corroborated by Lieuwen et al. [44] through experimental investigation. Furthermore, it was shown that the dominant characteristic time associated with the instability mechanism is the convective time

from the point of the formation of the reactive mixture to the point where it is actually burned at the flame. In addition, experimental work presented by Richards and Janus [64] showed that the nozzle reference velocity is an important factor in the development of instabilities. Emphasis has also been put in understanding the dynamic behavior of the flame since this is an important element in the instability mechanism. Fleifil et al. [23] analyzed and modeled the behavior of a laminar premixed flame with a perforated plate as flame holder; similarly in [20] Dowling studied the dynamics of a premixed ducted flame burning in the wake of a bluff-body flame holder. Moreover, Klein et al. [39, 38] developed a new measurement technique to assess the flame characteristics where the flame is represented either as an autonomous source of sound or as an amplifier of sound in the combustion interactions.

Models of large-scale combustors are far from being fully developed. In order to model accurately these complex combustion systems, partial differential equations must be used to describe the dynamic interactions inside of the combustion chamber. Besides, it is not always practical to consider all the elements affecting the combustion process. Although, some simplifications in the dynamic equations could be applied, the resulting models still present high complexity. A research trend in modeling combustion instabilities looked to identify the combustion system experimentally as a network of acoustic elements. Hence, the acoustics, flame and burner dynamics are modeled based on acoustic properties using experimental data. However, these models structure have their roots in physical characteristics. Most of this work has been carried out by Paschereit, Schuermans, Polifke, Gstohl and Van Room [30, 55, 59, 68], in the Alstom Power Research Center (former ABB Alstom Power Technology Center). Similarly, in [49] Murray et al. presented a study in sys-

tem identification for limit cycles systems with application to combustion processes; linear systems identification, time-delay estimation and describing function methods are employed in the modeling process. The combustor model structure is based on physical considerations. In this context, Smith et al. [70] addressed the problem of model validation of combustion models, and explained the necessity of new model validation techniques that takes into account nonlinear model perturbation and the effect of broad band disturbances.

In general there are two methods to attenuate combustion instabilities: *passive* and *active* control. Passive control involves redesigning the combustion chamber, including burner, fuel supply, etc., in such a way that the system as a whole provides enough damping to avoid the thermoacoustic interactions. Passive methods for controlling combustion instabilities in dump combustors have been studied by Gutmark et al. [32]. Their application typically requires modifications to the fuel injection or combustor hardware to eliminate the source of the variation in the heat release or to increase the acoustic damping; they include baffles, resonators, and acoustic liners. However, implementation of these passive approaches could be costly and time consuming, and sometimes not very effective.

The study of active control methods started in early 1950s with an application to rocket motor instabilities. Since the 1980s, the interest has raised due to strict pollutants regulations and new actuators and sensors development. The active control strategies employed to dampen or eliminate thermoacoustic oscillations vary widely, both in terms of the theoretical basis for the control system, as well as the actual hardware used. They are described in two important review papers by Candel [11] and McManus et al. [47]. In a recent paper [2], Annaswamy and Ghoniem reviewed the basic modeling techniques in combustion instabilities, as well as the

main problems faced by active control strategies. Hendricks and Schadow in [35] presented a survey of the research carried out at the Office of Naval Research (ONR) and summarized the progress achieved in this field.

Active control can be divided in two main streams: *acoustic* and *fuel modulation.* In acoustic modulation, an acoustic driver is used to modulate the pressure field inside of the chamber and then modify the mixing pattern fuel-air before entering the flame front. Consequently, the heat released by the flame is altered and the coupling in the instability mechanism could be suppressed. Meanwhile, fuel modulation modifies the fuel flow stream directly into the burner, such that the heat release is not coupled with the acoustic characteristics of the chamber. Moreover, active control can be classified in two main strategies: *open-loop* and *closed-loop.*

In open-loop systems, the control action is independent of the combustor's response to the control input. Essentially, they provide a fixed stimulus to the combustor in order to disrupt the instability mechanism. Usually, an oscillatory signal with a fixed amplitude and frequency is applied to the combustor by fuel or pressure modulation. The effectiveness of this technique is very dependent on their calibration, which is a difficult task. Following this philosophy, acoustic and fuel forcing applied to a liquid incinerator has been reported by Gutmark et al. [33]. In [58], Paschereit et al. applied open-loop control to suppress symmetric and helical thermoacoustic instabilities in an experimental swirl-stabilized combustor. In the Mechanical Department at LSU, Stephens et al. [71] presented the use of open-loop control methodologies in a liquid fueled swirl combustor.

The basic idea of active control in a continuous-flow combustion system is that, by monitoring a representative signal of the instability coupling, appropriate acoustic or fuel forcing can be applied such that the instability is suppressed. The feedback

signal is produced generally by a pressure transducer or by a heat-release sensor, which monitors one of these instability mechanisms at some position of the chamber. The basic control strategy is motivated by the Rayleigh's Criterion, where the pressure or heat release measurement is delayed and amplified (*phase-delay control*) by a specific amount, and fed back to the system by means of either a loudspeaker or a fuel valve. The attenuation factors obtained with phase-delay control are moderate and sensitive to changes in the operating conditions of the combustor. Pioneering work is due to Bloxsidge et al. [9], who tested this technique and explained its success using theoretical relations. In the same line of work, Langhorne et al. [41] used measured transfer functions describing the flame's response to predict the optimal time-delay that should be applied to the system. Gulati and Mani [31], and Paschereit et al. [56, 57] applied this kind of control using acoustic actuators in combustion test rigs. With respect to fuel modulation, Murugappan et al. [50] and Cohen et al. [15] presented applications of phase-delay control using fuel injectors as control actuators, the first one in a swirl stabilized combustor and the latter one in a lean, premixed combustor. A new approach was suggested by Neumeier and Zinn [52, 53, 54], an N-mode observer was used to track the frequency, amplitude and phase of the first N-unstable modes, the resulting decomposed signal was then delayed and amplified for feedback purpose. Applications of this technique to lean, premixed combustors have been reported by Sattinger et al.[66] and Hibshman et al. [36]. Another approach was taken by McManus et al. [48], he also investigated phase-delay control, but implemented a pulse-width modulation control scheme using an optical flame emission sensor to drive a control fuel injector. The algorithm was tested using a simple third-order combustor model, as well as experimentally.

Research on model-based techniques for control of combustion instabilities began mainly in the 1990s. In [76], Yang et al. were the first research group to develop linear theory to study active control of longitudinal pressure oscillations in a combustion chamber. Their model was used to design a digital observer-based controller. The control strategy was tested only in simulation but it showed its potential to suppress combustion instabilities. Continuing this work, Fung et al. [26] used this model assuming the control actuator was spatially distributed. The feedback control is produced by the injection of secondary fuel into the chamber, and the mass flow rate of this injected fuel is modulated by a PI controller. Again, the effectiveness of this strategy was shown only by simulation. In [27], Fung and Yang added nonlinear characteristics to the model and showed the existence and stability of limit cycles by using the time averaging method. An optimization process was suggested to select the gains of the PI controller. Recently, Krstic et al. [40] presented a self-tuning scheme for adapting the parameters of a PI controller applied to a nonlinear Culick-type [16] combustor model, a Lyapunov-based criterion is used in order to regulate the nonlinear pressure oscillations. The algorithm was simulated with successful results. On the other hand, Annaswamy, Fleifil and Hathout et al. [3, 24, 25, 34] have developed a model based on linear acoustics and nonlinear flame dynamics for a simple premixed laminar combustor. Linearization was applied to the nonlinear model in order to design an LQG controller. This LQG controller showed to be effective for a large class of initial conditions. In addition, it was also proposed a nonlinear controller, where the LQG linear controller was connected in parallel with a neural network to compensate for uncertainties in the system. Experimental testing was carried out in a small size combustion test-rig in MIT.

On the other hand, adaptive control has also been suggested as an alternative control strategy to suppress combustion instabilities. Evesque and Dowling in [22] proposed an adaptive controller based on an IIR filter, where the coefficients were optimized by an LMS algorithm.

In [37], Hong et al. proposed for the first time the use of robust feedback theory to the combustion instability problem. The control system was synthesized via structural singular values (μ-technique) in the $\mathcal{H}_\infty$ setting. However, the approach taken assumed that the nominal plant was expressed only by the acoustic dynamics and the flame characteristics were lumped in the feedback loop as an uncertainty block. This methods seems not to be the most appropriate since the flame characteristics are very important in the actual combustion system. Contrary to this approach, Chu et al. [14] proposed the use of linearization to derive the combustor linear dynamics from a nonlinear model for a premixed turbulent combustor. Finally, $\mathcal{H}_\infty$ Loop Shaping control design was applied. The results presented are only simulations and none experimental implementation was reported. Recently, Annaswamy et al. [4] reported experimental results of $\mathcal{H}_\infty$ controllers. However, the study was only carried out in a small combustor test-rig (1kW) with laminar flow.

It is important to point out that the $\mathcal{H}_\infty$ based design was mainly tested in simulation so far and no experimental test in a large size combustor chamber have been reported to our knowledge. Furthermore, the question of how well a single controller could perform for a set of different operating conditions was still an open question until now. This issue is extremely important in active control of combustion systems, since it is alway desirable to have a single controller that could provide

enough robustness to attenuate pressure oscillations for a wide range of operating conditions.

The rest of the dissertation is divided in 11 chapters. In Chapter 2, a brief overview of the basic principles of combustion chambers is presented. Chapter 3 gives a description of the dynamics involved in the thermoacoustic instability mechanism. In Chapter 4, the sensors and actuators commonly used in active combustion control are presented. Chapter 5 introduces the concept of Riemann Invariants to characterize the acoustic properties of combustion chambers. A brief introduction to optimal control is presented in Chapter 6. In Chapter 7, the modeling and control design procedures for a gaseous fueled combustor are fully described. Similarly, the application to a liquid fueled combustor is presented in Chapter 8. In Chapter 9, the new accomplishments and perspectives of future work in the Mechanical Engineering Department at LSU are outlined. An alternative control design procedure for the $\mathcal{H}_\infty$ strong stabilization problem is introduced in Chapter 10 and finally some concluding remarks are given in Chapter 11.

CHAPTER 2

COMBUSTION CHAMBER BASICS

In this introductory chapter, the basic concepts surrounding combustion chambers are presented. Their role in gas turbines and their main operational features are introduced for a complete understanding of their complex dynamics. Most of the material presented in this chapter was summarized from the references [29, 42, 65].

2.1 Gas Turbines

A simple gas turbine is comprised of three main sections: a compressor, a combustor chamber and a power turbine. The gas turbine operates on the principle of the Brayton cycle, where compressed air is mixed with fuel and burned under constant pressure conditions. The resulting hot gas is then allowed to expand through a turbine to perform work.

The turbojet (turbines used in jet engines) uses a series of fan-like compressor blades to bring air into the engine and compress it. In this section, there are a series of rotor and stator blades. Rotor blades perform somewhat like propellers since they gather and push air backward into the engine. The stator blades serve to straighten the air flow as it passes from one set of rotor blades to the next. As the air continues to be forced further into the engine, it travels from the low-compression set of rotors and stators to the high-compression set. This last set puts what it might be the final squeeze of the air. The *combustion chamber* receives the high pressure air, and mixes fuel with it, and burns the mixture to increase its temperature. The resulting hot and very high-velocity gases strike the blades of

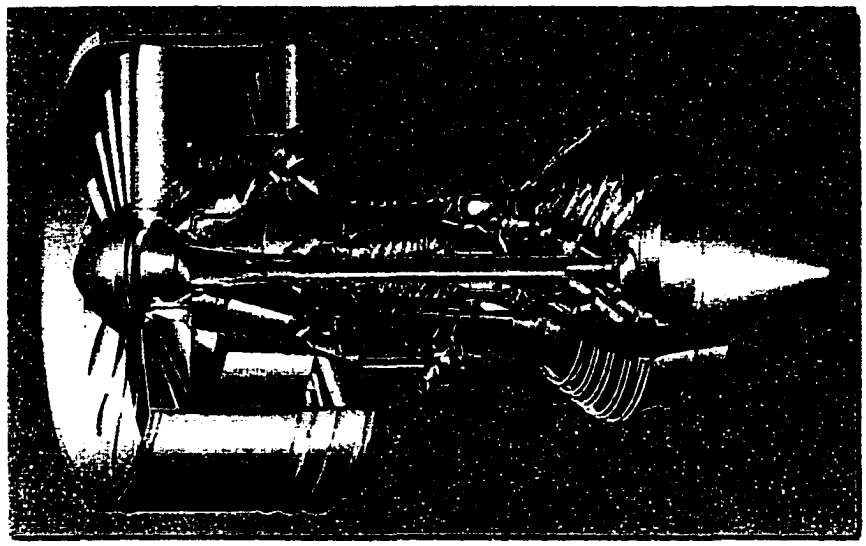

Figure 2.1: GP7000 Turbofan Engine Developed by GE and P&W (http:// www.pratt-whitney.com/3a/html/products_gp7000.html).

the turbine and causes it to spin rapidly. The turbine is mounted on a shaft which is connected to the compressor. Thus, the spinning is what causes the compressor sections to function. After passing the turbine blades, the hot and highly accelerated gases go into the engine's exhaust section. The exhaust section of the jet engine is designed to give additional acceleration to the gases and thereby increase thrust. The exhaust section also serves to straighten the flow of the gases as they come from the turbine. Basically, the exhaust section is a cone mounted in the exhaust duct. This duct is also referred as the tailpipe. Figure 2.1 shows the turbofan engine GP7000, commonly used for propulsion systems, manufactured by GE and P&W.

Nowadays gas turbines have many applications: power generation, mechanical drives, propulsion systems, etc. Each application demands changes in the operating configuration of the turbine. However, the overall basic principles are still preserved.

On the other hand, a gas turbine combustor has to satisfy some basic requirements related with its working operation:

- High combustion efficiency (the fuel should be completely burned so that all its chemical energy is liberated as heat);
- Wide stability limits (the flame should stay alight over a wide range of pressure and air/fuel ratios);
- Low emissions of gaseous pollutant species;
- Durability and
- Maintainability.

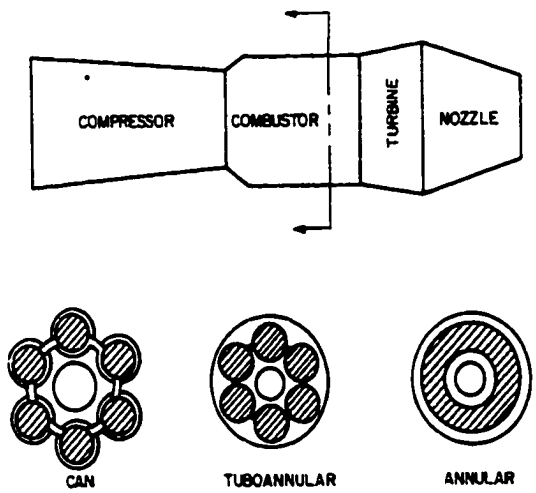

Figure 2.2: Three Main Combustor Types [42].

In a gas turbine, the choice of a particular combustor type and layout is determined largely by the overall engine design and by the need to use the available space as effectively as possible. There are two basic types of combustors, tubular and annular, see Figure 2.2. A tubular (or "can") combustor is comprised of a cylindrical

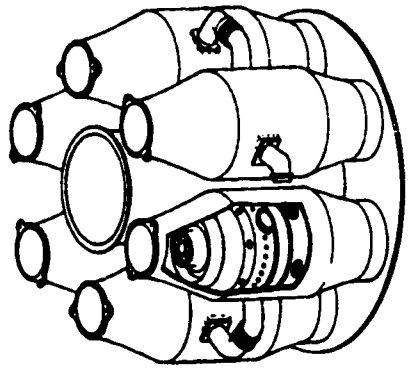

Figure 2.3: Multi-can Combustor Arrangement [42].

liner mounted concentrically inside a cylindrical casing. A multi-can combustor is shown in Figure 2.3. In an annular combustor, an annular liner is mounted concentrically inside an annular casing. In many ways, it is an ideal form of chamber, because its clean aerodynamics layout results in a compact unit of lower pressure loss than other combustor types. A compromise between these two extremes is the "tuboannular" or "can-annular" combustor, in which a number of equispaced tubular liners are placed within an annular air casing.

2.2 Stoichiometric Mixture

Although the combustion of a hydrocarbon fuel is an extremely complex process, it may be analyzed on the assumption that combustion can be fully described by a single global reaction in which fuel and air react at certain rate to form combustion products. In order to achieve complete combustion enough air must be provided to convert the fuel completely to carbon dioxide and water vapor. *Stoichiometric* mixtures, by definition, contain sufficient oxygen for complete combustion; thus, operation at the stoichiometric fuel/air ratio will release all the latent heat of the

combustion fuel. If the fuel is burned at a numerically lower fuel/air ratio, the mixture is referred to as *lean* or *weak*. Combustion at a fuel/air ratio larger than the stoichiometric value implies a deficiency of oxygen, this case is called *rich* mixture. For rich mixtures, the combustion is incomplete and partially burned fuel will escape from the combustion zone. In the combustion field, it is common to express the mixture strength in terms of an *equivalent ratio* ϕ. The equivalent ratio is the actual fuel/air ratio divided by the corresponding stoichiometric ratio. Thus, for all fuels, $\phi = 1$ denotes a stoichiometric mixture. Furthermore, a value of $\phi > 1$ indicates a rich mixture, meanwhile $\phi < 1$ denotes a lean mixture.

2.3 Swirl Stabilization

In combustion the term "stability" is often used rather to describe either the range of fuel/air ratios over which controlled combustion can be achieved, or as a measure of the maximum air velocity that the system can tolerate before the flame is extinct. Hence, the notion of "good stability performance", applied to a combustor, could mean either that it is capable of burning over a wide range of mixture strengths or that its blowout velocity is high.

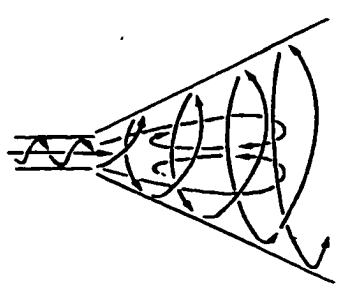

Figure 2.4: Flow Recirculation Induced by Swirl [42].

The primary-zone airflow pattern in the burner influences considerably the stability properties of the flame. Many different types of airflow patterns are employed in practice, but one feature common to all is the creation of a toroidal reversal flow that entrains and recirculates a portion of the hot combustion products in order to mix with the incoming fuel and air. The property of having a flow recirculation in the primary zone is denoted as *swirl stabilization.* In burners that use fuel injectors the most effective way of achieving this effect is either by fitting a swirler (swirl vanes) in the dome around the injectors or supplying a tangential flow to the oxidant. This type of recirculation pattern provides a better mixing than is normally obtained by other means, because swirl components produce *high turbulence and rapid mixing rates.* These characteristics of swirling burners are preferred to control the stability and intensity of combustion, and the size and shape of the flame region. For a review of the role of swirling flows in combustion refer to [72].

2.4 Types of Flames

Most fundamental studies of flame combustion are performed using gaseous or pre vaporized fuels. Moreover, although a flame can propagate through a static gas mixture, it is usual to stabilize the flame at a fixed point and supply it with a continuous flow of combustible mixture. Under these conditions, a flame can be divided into two main classes - *premixed flames* and *diffusion flames* - depending on whether the fuel and the air are mixed before combustion, or mixed by diffusion in the flame zone. Depending on the prevailing flow profile and velocity, both types of flame can be further classified as *laminar* or *turbulent.* Turbulence is of prime importance because most flowing fuel-air mixtures are turbulent and turbulence is known to enhance mixing and flame speeds considerably.

In practical liquid-fueled systems, the fuel is injected into the reaction zone following the principle of diffusion flames. Here, the evaporation of the fuel droplets in the spray is of prime importance for homogeneous combustion. The overall rate of evaporation depends on the pressure, temperature and diameter and relative velocity of the drops.

CHAPTER 3

THERMOACOUSTICAL INSTABILITIES

First, an introduction to the driving mechanisms of thermoacoustical instabilities in combustion chambers is presented in this chapter. Next, the derivation of two analytical combustor models, previously presented in literature, is introduced for better understanding of the instability coupling in combustion systems.

3.1 Instability Mechanisms

What is a thermoacoustic instability? In a gas turbine, the combustion chamber receives the air flow coming from the compressor and increase its temperature by a combustion process. In the turbine, this process is carried out inside an inclosing volume. This inclosing volume has inherited acoustic properties that depend mainly on temperature and boundary conditions. In addition, the dynamics of the combustion process depend on different parameters: mixing between fuel and oxidizer, chemical reactions and heat-transfer to the system and surroundings. All these phenomena have their own time and length scales associated with their intrinsic characteristics. Moreover, in large-scale combustors turbulence is introduced as a stabilization method of the flame; in some cases this turbulence creates periodic structures that liberate heat, *vortex structures*, with certain frequency associated. Thus, for some operating conditions of the combustor, the acoustic characteristics of the chamber can match the time-scales associated with the liberation of heat in

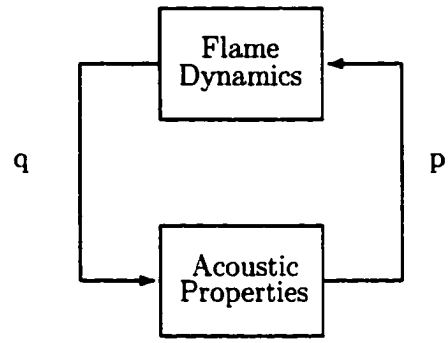

Figure 3.1: Thermoacoustic Instability Mechanism.

the flame front. As a result, a coupling could be generated between the pressure waves and the heat release properties, *thermoacoustic instability*. These two phenomena interact and enhance mutually producing a feedback loop linking these two dynamics as shown in Figure 3.1. Consequently, strong pressure pulsations might develop inside of the combustor. However, the growth of these oscillations is limited since the fluctuations cannot increase infinitely due to the energy limitations in the combustor. This phenomena is usually related to nonlinear characteristics of the system (saturation-like). Thus, thermoacoustic instabilities are represented by a *limit-cycle* type of oscillations [19].

In liquid-fueled combustors extra parameters are also considered in the development of combustion instabilities. In this type of combustors the fuel and air are mixed by diffusion in the burner. Thus the burning rate depends on the instantaneous vaporization rate of the fuel spray, which depends in turn on the droplet size distribution of the spray. Therefore, the convective time from the fuel nozzle to the flame front plays an important role in the instabilities appearance. Moreover, pulsations in the air or fuel supply can also trigger an instability [65].

The first one to understand and explain this coupling phenomena in combustion processes was L. Rayleigh in [62]. He noticed that vibrations inside a cylinder can be maintained by heat when the resonating body is gaseous. "If heat be periodically communicated to, and abstracted from a mass of air vibrating, the effect produced will depend upon the phase of vibration at which the transfer of heat takes place. If heat be given to the air at the moment of the greatest condensation, or be taken from it at the moment of greatest rarefaction, the vibration is encouraged. On the other hand, if heat be given at the moment of greatest rarefaction, or abstracted at the moment of greatest condensation, the vibration is discouraged". In addition due to this feedback loop, the frequency characteristics can be altered. So L. Rayleigh explained also the pitch behavior due to the instability coupling. "If the air be at its normal density at the moment when the transfer of heat takes place, the vibration is neither encouraged nor discouraged, but the pitch is altered. Thus the pitch is *raised* if heat be communicated to the air a quarter of period before the phase greatest condensation; and the pitch is *lowered* if the heat be communicated a quarter period after the phase of greatest condensation". Consequently, the relative phase between the acoustic vibrations and the addition of heat can have two main effects:

- Enhance or attenuate the oscillations and
- Raise or lower the pitch.

Analytic modeling approaches have been developed to pursue a general understanding of combustion instabilities. However some assumptions have to be made in order to simplify the dynamics and be able to derive analytical representations of the combustion process. Nevertheless, these assumptions are not restrictive and allow to capture valuable insight about the driving mechanisms of the instabilities.

Linear theory can determine the frequencies and the growth rate of the possible oscillations. Meanwhile, nonlinear analysis can determine its limiting amplitudes. The analytical models developed in literature represent the thermoacoustic instabilities as a feedback cycle among linear dynamics, process delays and nonlinear characteristics. Mainly the linear dynamics represent the acoustic response of the chamber, the process delays are associated with convective delays in the flame front and the nonlinear characteristics are linked to the flame behavior [49].

3.2 Combustor Models

In large size combustors, flame stabilizing mechanisms such as swirl or bluff-body recirculation create turbulence in the reaction zone to enhance the mixing between reactants and improve the lean blow-out limits of the flame. Furthermore, the induced turbulence creates chaotic interactions in the flow which can only be tracked by nonlinear partial differential equations [18]. Therefore modeling these types of combustors is extremely complicated. On the other hand, understanding the dynamics of simple small size-combustors can give valuable insight about the instability coupling that can help to extend these notions to more complex systems.

To our understanding, only two analytical combustor models have been developed in literature to be used for control applications. These two models were derived by research groups in

- MIT (USA) and
- Cambridge (England).

These two models are based on small-size combustors with rather simple (compared to large-scale combustors) dynamics. Both models correspond to premixed combustors and assume that the driving mechanism of instability is the coupling between

the velocity fluctuations at the flame holder (u'_G) and the heat release rate (q'_G). However, the flame stabilization process and active control strategy are different for both models. The dynamics presented by these two models clearly are not as complicated as in large-scale combustors where flame stabilization mechanisms, like *swirl*, add three dimensional characteristics to the flow interactions. But the knowledge that can be obtained by analyzing the instability mechanism, flame-acoustics interaction, is important. The derivation of these two models is given next.

The following assumptions are taken in order to obtain the combustor models:

- One-dimensional flow. in the longitudinal direction of the combustor;
- Inviscid flow, i.e. the duct has negligible dissipation effect on the acoustic waves;
- Negligible thermal conductivity to the surroundings;
- Perfect gas and
- Stationary flow

In order to keep a consistent notation, let $\bar{(\cdot)}$ denote a mean component and $(\cdot)'$ a fluctuating component for the quantities considered in the next derivations.

3.2.1 Cambridge Combustor Model

The derivation of this model was carried out by Dowling, Chu and Glover in [14] and [20]. A premixed ducted flame, burning in the wake of a bluff-body flameholder is considered as shown in Figure 3.2. The combustor consists mainly of two sections, upstream and downstream of the flame holder. For simplicity, the inlet is choked, so a constant mass flow rate is present at that point, and the end of the chamber is open. Thus, oncoming flow distorts the flame surface and thereby

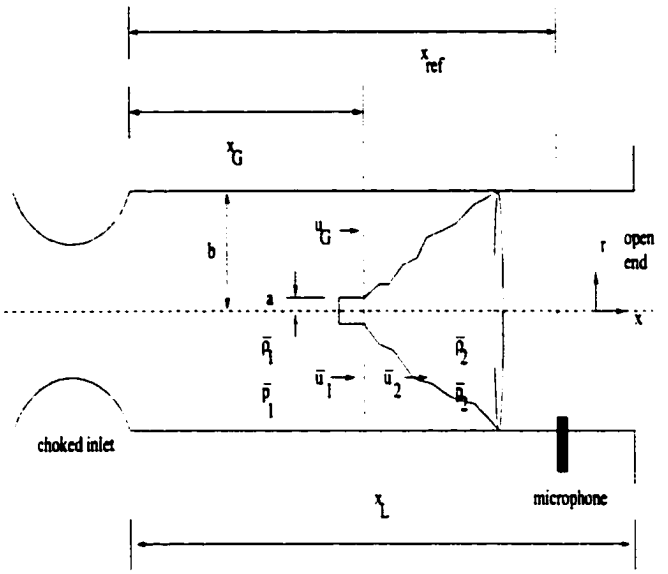

Figure 3.2: Cambridge Model: Combustor Setup.

alters the rate of combustion, while this unsteady heat release generates acoustic waves which reflect from the ends of the duct and disturb the flame in a cyclic process. Therefore the possibility of self-excited oscillations is present at certain flow conditions. The acoustic waves are assumed to behave linearly and the main nonlinearity is identified in the rate of heat release, which essentially 'saturates' once the amplitude of the velocity fluctuation exceeds its mean. For control purpose, a fuel injector is assumed to provide an extra source of heat at the flame front (fuel modulation). The derivations for the acoustics and flame models are presented next.

3.2.1.1 Acoustic Model

Consider Figure 3.2 and assume that the heat-release is spatially localized at $x = x_G$, in other words

$$q(x,t) = \bar{q}_G + \frac{q'_G(t)}{\pi b^2}\delta(x - x_G) \tag{3.1}$$

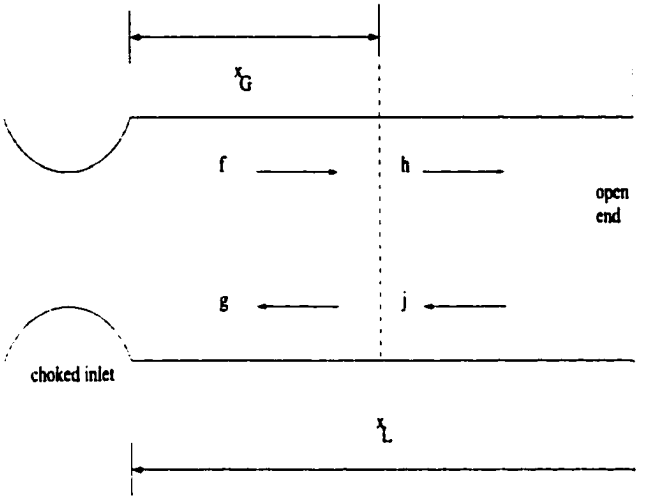

Figure 3.3: Cambridge Model: Acoustic Waves.

where q_G denotes the heat release rate, b the radius of the shield and $\delta(\cdot)$ represents the Dirac delta function. Under this assumption, it can be proved [3] that the mean variables are essentially constant over the length of the combustor except for a step change at x_G. Note that this discontinuous behavior at x_G can be represented by a normal shock relation. Hence, for flow through a normal shock with no direction and area change, the equations of conservation of mass, momentum and energy can be combined with the perfect gas equation.

$$\rho_2 u_2 - \rho_1 u_1 = 0 \tag{3.2}$$

$$p_2 + \rho_2 u_2^2 - p_1 - \rho_1 u_1^2 = 0 \tag{3.3}$$

$$\frac{\gamma}{\gamma - 1}\left(p_2 u_2 - p_1 u_1\right) + \frac{1}{2}\rho_1 u_1 \left(u_2^2 - u_1^2\right) = \frac{q}{\pi b^2} \tag{3.4}$$

where ρ stands for the density, γ for the ratio of specific heat capacities (property of the fuel), p for the pressure, u for the velocity of the flow, T for the temperature and the sub-indexes 1 and 2 stand for the conditions $x = x_G^-$ and $x = x_G^+$ respectively.

Next, assume that the pressure perturbations are the summation of two acoustics waves, *Riemann Invariants*, downstream ($0 \leq x \leq x_G$) and upstream ($x_G \leq x \leq x_L$) of the combustion zone respectively, with their phase referenced at $x = x_G$ as shown in Figure 3.3. An analytical explanation for this assumption will be given in Chapter 5. Hence, let for the upstream region

$$p(x,t) = \bar{p}_1 + f\left(t - \frac{x - x_G}{\bar{c}_1 + \bar{u}_1}\right) + g\left(t + \frac{x - x_G}{\bar{c}_1 - \bar{u}_1}\right) \tag{3.5}$$

$$u(x,t) = \bar{u}_1 + \frac{1}{\bar{\rho}_1 \bar{c}_1}\left[f\left(t - \frac{x - x_G}{\bar{c}_1 + \bar{u}_1}\right) - g\left(t + \frac{x - x_G}{\bar{c}_1 - \bar{u}_1}\right)\right] \tag{3.6}$$

$$\rho(x,t) = \bar{\rho}_1 + \frac{1}{\bar{c}_1^2}\left[f\left(t - \frac{x - x_G}{\bar{c}_1 + \bar{u}_1}\right) + g\left(t + \frac{x - x_G}{\bar{c}_1 - \bar{u}_1}\right)\right] \tag{3.7}$$

and downstream (neglecting the influence of the entropy)

$$p(x,t) = \bar{p}_2 + h\left(t - \frac{x - x_G}{\bar{c}_2 + \bar{u}_2}\right) + j\left(t + \frac{x - x_G}{\bar{c}_2 - \bar{u}_2}\right) \tag{3.8}$$

$$u(x,t) = \bar{u}_2 + \frac{1}{\bar{\rho}_2 \bar{c}_2}\left[h\left(t - \frac{x - x_G}{\bar{c}_2 + \bar{u}_2}\right) - j\left(t + \frac{x - x_G}{\bar{c}_1 - \bar{u}_1}\right)\right] \tag{3.9}$$

By the two boundary conditions: chocked inlet (at $x = 0$ constant mass-flow rate, i.e. $u'(0,t)\rho'(0,t) = constant$) and open end ($p'(x_L,t) = 0$), it is deduced that

$$f(t) = \frac{1 - \bar{M}_1}{1 + \bar{M}_1} g\left(t - \tau_U\right), \quad \tau_U = \frac{2x_G}{\bar{c}_1(1 - \bar{M}_1^2)} \tag{3.10}$$

and

$$j(t) = -h\left(t - \tau_D\right), \quad \tau_D = \frac{2(x_L - x_G)}{\bar{c}_2(1 - \bar{M}_2^2)} \tag{3.11}$$

where

$$\bar{M} = \frac{\bar{u}}{\bar{c}}, \quad \bar{c}^2 = \frac{\gamma \bar{p}}{\bar{\rho}} \tag{3.12}$$

On the other hand, the pressure sensor is assumed to be located at $x = x_{ref}$ downstream of the flame burner. Thus, from (3.8) the pressure signal at this location can be calculated

$$p_{ref}(t) = \bar{p}_2 + h(t - \tau_{ref}^h) + j(t + \tau_{ref}^j) \tag{3.13}$$

where

$$\tau_{ref}^{h} = \frac{x_{ref} - x_G}{\bar{c}_2 + \bar{u}_2}$$
$$\tau_{ref}^{j} = \frac{x_{ref} - x_G}{\bar{c}_2 - \bar{u}_2}$$

Also, the velocity at the flame holder u_G is an important factor related to the flame dynamics. Furthermore, it will be the feedback mechanism for the instability as will be seen later. So, it is calculated from (3.6)

$$u_G(t) = \bar{u}_1 + \frac{1}{\bar{\rho}_1 \bar{c}_1}[f(t) - g(t)] \tag{3.14}$$

Thus substituting back into equations (3.2), (3.3) and (3.4), a transfer function representation can be obtained for p'_{ref} and u'_G in terms of q'_G

$$\begin{bmatrix} G(s) \\ H(s) \end{bmatrix} = \left[\mathbf{X} - \mathbf{Y}\begin{pmatrix} e^{-\tau_U s} & \\ & e^{-\tau_D s} \end{pmatrix}\right]^{-1} \begin{bmatrix} 0 \\ \frac{1}{\bar{c}_1 \pi b^2} \end{bmatrix} Q_G(s) \tag{3.15}$$

$$\begin{bmatrix} P_{ref}(s) \\ U_G(s) \end{bmatrix} = \begin{bmatrix} 0 & e^{-\tau_{ref}^{h} s} - e^{-(\tau_D - \tau_{ref}^{j})s} \\ \frac{1}{\bar{\rho}_1 \bar{c}_1}\left(\frac{1-\bar{M}_1}{1+\bar{M}_1} e^{-\tau_U s} - 1\right) & 0 \end{bmatrix} \begin{bmatrix} G(s) \\ H(s) \end{bmatrix}$$

where

$$\mathbf{X} = \begin{bmatrix} -1 + \bar{M}_1\left(2 - \frac{\bar{u}_2}{\bar{u}_1}\right) - \bar{M}_1^2\left(1 - \frac{\bar{u}_2}{\bar{u}_1}\right) & 1 + \bar{M}_1 \frac{\bar{\rho}_1 \bar{c}_1}{\bar{\rho}_2 \bar{c}_2} \\ \frac{1-\gamma\bar{M}_1}{\gamma-1} + \bar{M}_1^2 - \frac{1}{2}\bar{M}_1^2(1-\bar{M}_1)\left(\frac{\bar{u}_2^2}{\bar{u}_1^2} - 1\right) & \frac{\bar{c}_2}{\bar{c}_1}\frac{1+\gamma\bar{M}_2}{\gamma-1} + \frac{\bar{\rho}_1}{\bar{\rho}_2}\bar{M}_1\bar{M}_2 \end{bmatrix}$$

$$\mathbf{Y} = \begin{bmatrix} \frac{1-\bar{M}_1}{1+\bar{M}_1}\left[1 + \bar{M}_1\left(2 - \frac{\bar{u}_2}{\bar{u}_1}\right) + \bar{M}_1^2\left(1 - \frac{\bar{u}_2}{\bar{u}_1}\right)\right] & 1 - \bar{M}_1 \frac{\bar{\rho}_1 \bar{c}_1}{\bar{\rho}_2 \bar{c}_2} \\ \frac{1-\bar{M}_1}{1+\bar{M}_1}\left[\frac{1+\gamma\bar{M}_1}{\gamma-1} + \bar{M}_1^2 - \frac{1}{2}\bar{M}_1^2(1+\bar{M}_1)\left(\frac{\bar{u}_2^2}{\bar{u}_1^2} - 1\right)\right] & -\frac{\bar{c}_2}{\bar{c}_1}\frac{1+\gamma\bar{M}_2}{\gamma-1} - \frac{\bar{\rho}_1}{\bar{\rho}_2}\bar{M}_1\bar{M}_2 \end{bmatrix}$$

Finally, denote the overall acoustics model as $T_{acoustic}$, i.e.

$$\begin{bmatrix} P_{ref}(s) \\ U_G(s) \end{bmatrix} = T_{acoustic} \cdot Q_G(s) \tag{3.16}$$

3.2.1.2 Flame Dynamics

The concept of a time-invariant turbulent flame speed is used to develop a kinematic model of the flame response to flow disturbances. This model applies to the case where oncoming flow is related to the heat release rate at any time instant. Moreover, the heat release rate is assumed to be proportional to the flame surface. First, the flow inside the combustor is considered axisymmetric and combustion assumed to begin on a surface $G(x, r, t) = 0$ whose axial position at radius r is given by $x = \xi(r, t)$ as shown in Figure 3.4.

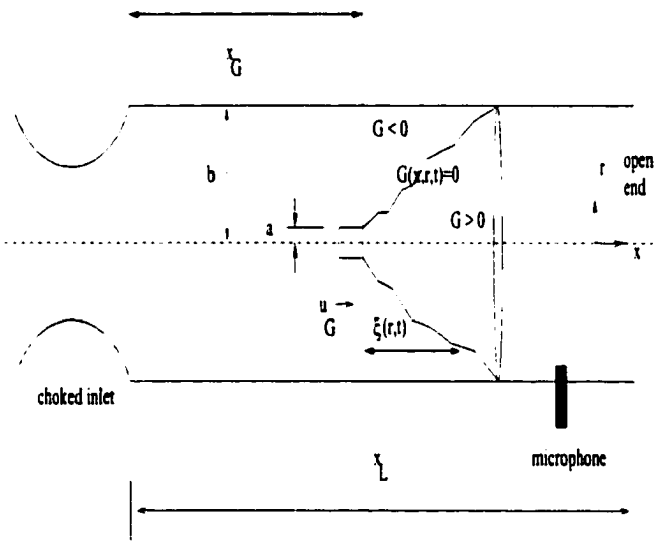

Figure 3.4: Cambridge Model: Flame Interaction.

In this way, the flame initiation surface is given by $G(x, r, t) = x - \xi(r, t)$. This surface is assumed to propagate normal to itself at constant speed S_u, relative to the unburnt fluid. In other words, the surface $G(x, r, t) = 0$ moves in the direction of its normal $\mathbf{n}$ with speed $\mathbf{u} \cdot \mathbf{n} - S_u$, where $\mathbf{u} = (u, v)$ is the unburnt fluid particle

velocity and $\mathbf{n}$ points downstream. This is equivalent to saying

$$\frac{\tilde{D}G}{Dt} = \frac{\partial G}{\partial t} + (\mathbf{u} - S_u\mathbf{n}) \cdot \nabla G = 0$$

where $\tilde{D}/Dt$ represents the convected derivative with velocity $\mathbf{u} - S_u\mathbf{n}$. Note that rewriting $\mathbf{n} = \nabla G/|\nabla G|$, the familiar G-equation [46] is obtained

$$\frac{\partial G}{\partial t} + \mathbf{u} \cdot \nabla G = S_u|\nabla G|$$

Substitute the expression for $G(x, r, t)$

$$-\frac{\partial \xi}{\partial t} + u - v\frac{\partial \xi}{\partial r} = S_u\sqrt{1 + \left(\frac{\partial \xi}{\partial r}\right)^2} \tag{3.17}$$

When the density change across the initiation surface $G(x, r, t)$ is negligible, the particle velocity in last equation is given by that in the oncoming flow $(u, v) = (u_G, 0)$, where u_G denote the velocity at the flame holder. So, we have

$$\frac{\partial \xi}{\partial t} = u_G - S_u\sqrt{1 + \left(\frac{\partial \xi}{\partial r}\right)^2} \tag{3.18}$$

For simplicity the oncoming velocity is assumed to depend only on time, $u_G = u_G(t)$. Hence, given u_G at any time the flame location $\xi(r, t)$ can be obtained solving (3.18). Now, once $\xi(r, t)$ is known, the instantaneous flame surface area $A(t)$ can be computed from

$$A(t) = \int_a^b 2\pi r\sqrt{1 + \left(\frac{\partial \xi}{\partial r}\right)^2}\, dr \tag{3.19}$$

where b and a are the chamber and flame holder radius respectively. Finally, the heat-release rate q_G in the flame spreading region is taken proportional to the instantaneous flame surface with certain time delay τ_f

$$\frac{q_G}{\bar{q}_G} = \frac{A(t - \tau_f)}{\bar{A}}, \quad \tau_f = 0.4\frac{x_L}{\bar{u}_1} \tag{3.20}$$

where τ_f is chosen experimentally according to [19]. Consequently, the set of equations (3.18), (3.19) and (3.20) represents the nonlinear mapping from u_G to q_G under axisymmetric flow assumption. In fact, this set of equations can be linearized around certain operating point to obtain a transfer function that describes the flame dynamics.

Thus, in order to obtain the linear flame dynamics, (3.18) is linearized around the working point $\left(\bar{u}_G, \frac{\partial \bar{\xi}}{\partial r}\right)$ and (3.19) around $\left(\bar{A}, \frac{\partial \bar{\xi}}{\partial r}\right)$. As a result, the next two equations are derived for the oscillating components

$$\frac{\partial \xi'}{\partial t} = u'_G - S_u \sqrt{1 - \left(\frac{S_u}{\bar{u}_G}\right)^2}\, \frac{\partial \xi'}{\partial r} \tag{3.21}$$

and

$$\frac{A'(t)}{\bar{A}} = \frac{u'_G(t)}{\bar{u}_G} - \frac{2}{\bar{u}_G(b^2 - a^2)} \int_a^b r \frac{\partial \xi'}{\partial t} dr \tag{3.22}$$

Therefore by combining (3.21) and (3.22) a relation between A' and u'_G is derived, which is finally used with (3.20) to construct a mapping between q'_G and u'_G

$$\frac{Q_G(s)}{U_G(s)} = \frac{\bar{q}_G}{\bar{u}_G} \frac{2}{s\, t_\Omega\, (b+a)} \left[a - b\, e^{-t_\Omega s} + \frac{b-a}{s\, t_\Omega} \left(1 - e^{-t_\Omega s}\right) \right] e^{-\tau_f s} = T_{flame}(s) \tag{3.23}$$

where

$$t_\Omega = \frac{b-a}{S_u \sqrt{1 - \left(\frac{S_u}{\bar{u}_G}\right)^2}}$$

3.2.1.3 Control Model

A fuel injector is used in this model for control. This actuator is modeled as an external source of heat release q'_C at the flame front. In this setup, the fuel injector is assumed to have a linear and continuous response, which in fact is not very realistic. Nevertheless, as any actuator has bandwidth limitations that are

modeled as a second order transfer function

$$T_{fuel-injector} = \frac{Q_c(s)}{V_c(s)} = \frac{k_a e^{-\tau_a s}}{(1/\omega_a)^2 s^2 + 2(\zeta/\omega_a)s + 1} \tag{3.24}$$

where v_c' represents its injector input voltage, k_a is a calibration constant, ζ is the damping coefficient, ω_a is the bandwidth and τ_a the associated time delay. Hence, using the acoustic model (3.16), flame dynamics (3.23) and the fuel-injector response, the overall combustor control feedback system can be constructed as shown in Figure 3.5.

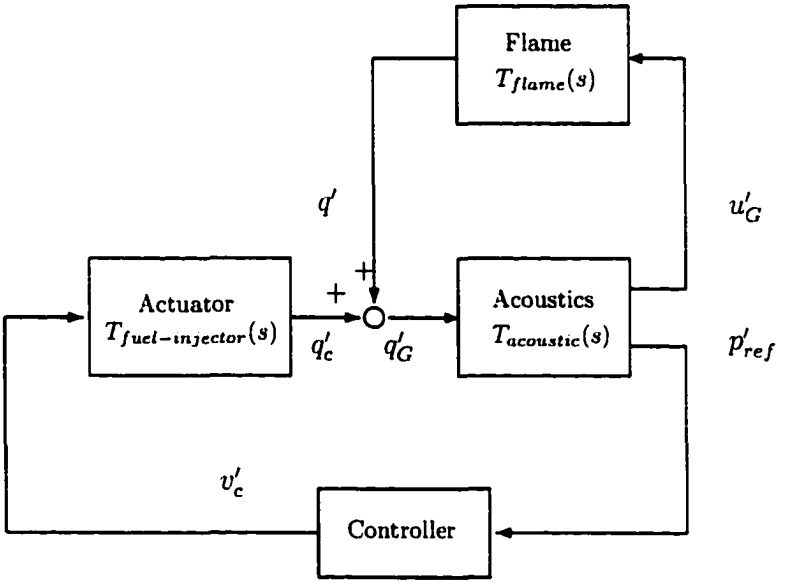

Figure 3.5: Camdrigde Model: Control Feedback Configuration

3.2.2 MIT Combustor Model

This model was derived by Annaswamy, Fleifil, Ghoneim, Ghoniem and Hathout in [3, 23, 24]. A laminar premixed combustor is assumed where the flame is stabilized by a perforated plate as shown in Figure 3.6. Active control is applied by a loudspeaker flush-mounted on the wall of the combustor shield upstream of the

flame. The acoustics are governed by the combustor geometry, boundary conditions, and thermal properties of the working medium. Meanwhile, the heat release dynamics are governed by the perturbations in the flow field around the flame surface, the flame stabilization mechanism, and the inhomogeneity in the reactive flow.

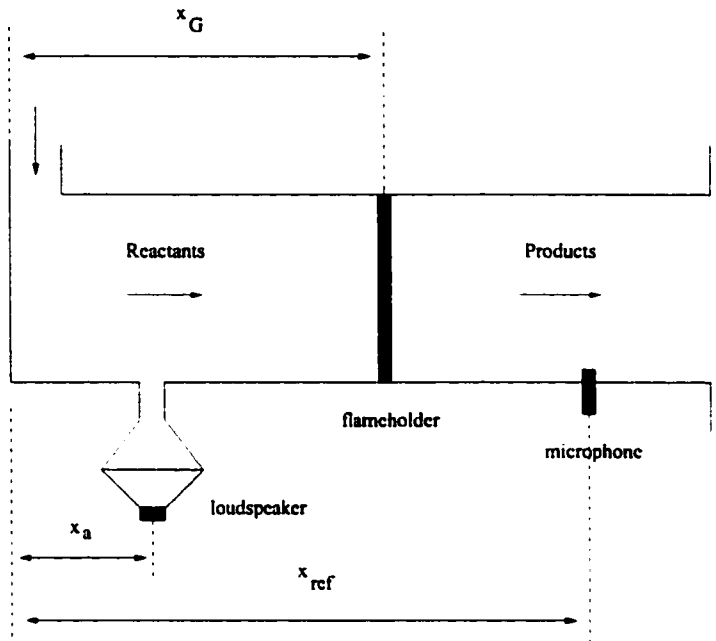

Figure 3.6: MIT Model: Combustor Setup.

3.2.2.1 Acoustic Model

For reactive-gas dynamics, the conservation equations can be stated under the assumptions given earlier

$$\frac{\partial \rho}{\partial t} + \frac{\partial (u\rho)}{\partial x} = 0 \tag{3.25}$$

$$\rho \frac{\partial u}{\partial t} + \rho u \frac{\partial u}{\partial x} + \frac{\partial p}{\partial x} = 0 \tag{3.26}$$

$$\frac{\partial p}{\partial t} + \gamma p \frac{\partial u}{\partial x} + u \frac{\partial p}{\partial x} = (\gamma - 1) q \tag{3.27}$$

where p is the pressure, u the velocity of the flow, ρ the density, γ the ratio of specific heat capacities and q the heat-release rate per unit volume. Now, assuming that the quantities in equations (3.25), (3.26) and (3.27) can be separated in mean $\bar{(\cdot)}$ and fluctuating $(\cdot)'$ components

$$\begin{aligned} \rho(x,t) &= \bar{\rho}(x) + \rho'(x,t) \\ p(x,t) &= \bar{p}(x) + p'(x,t) \\ u(x,t) &= \bar{u}(x) + u'(x,t) \\ q(x,t) &= \bar{q}(x) + q'(x,t) \end{aligned} \tag{3.28}$$

The next equations are derived for the fluctuating components

$$\frac{\partial \rho'}{\partial t} + \bar{\rho}\frac{\partial u'}{\partial x} + \bar{u}\frac{\partial \rho'}{\partial x} + \frac{\partial \bar{\rho}}{\partial x}u' + \frac{\partial \bar{u}}{\partial x}\rho' = 0$$

$$\bar{\rho}\frac{\partial u'}{\partial t} + \bar{\rho}\bar{u}\frac{\partial u'}{\partial x} + \bar{\rho}\frac{\partial \bar{u}}{\partial x}u' + \bar{u}\frac{\partial \bar{u}}{\partial x}\rho' + \frac{\partial p'}{\partial x} = 0 \tag{3.29}$$

$$\frac{\partial p'}{\partial t} + \gamma\bar{p}\frac{\partial u'}{\partial x} + \gamma\frac{\partial \bar{u}}{\partial x}p' + \frac{\partial \bar{p}}{\partial x}u' + \bar{u}\frac{\partial p'}{\partial x} = (\gamma - 1)q' \tag{3.30}$$

In addition, assume again that the heat released by the flame is localized at $x = x_G$, in other words

$$q'(x,t) = \frac{q'_G(t)}{\pi b^2}\delta(x - x_G) \tag{3.31}$$

So, under this assumption the mean variables are essentially constant over the length of the combustor except for a step change at x_G, meanwhile the derivatives will be of the order of $\bar{M}^2$. Therefore for low-Mach-number flows these derivatives can be neglected. Thus substituting in equation (3.31) and manipulating equations (3.29) and (3.30), it is obtained

$$\frac{\partial^2 p'}{\partial t^2} + [\bar{u}^2 - \bar{c}^2]\frac{\partial^2 p'}{\partial x^2} + 2\bar{u}\frac{\partial^2 p'}{\partial t \partial x} = \frac{(\gamma - 1)}{\pi b^2}\left[\frac{dq'_G}{dt}\delta(x - x_G) + \bar{u}q'_G(t)\frac{d\delta(x - x_G)}{dx}\right] \tag{3.32}$$

From last equation p' can be solved in terms of q'_G, and finally from (5.9) u' can be obtained from the computed p'. Note that (3.32) describes a second order hyperbolic partial differential equation whose solution is in nature infinite dimensional. So, an approximated solution is used, for this reason Galerkin method [51] is applied. This method is commonly employed to study combustion instability problems, for instance see [16]. Hence, assume the following solution to (3.32)

$$p'(x,t) = \bar{p}\sum_{i=1}^{N} \psi_i(x)\lambda_i(t) = \bar{p}\Psi^T(x)\Lambda(t) \tag{3.33}$$

where

$$\Psi^T = [\psi_1(x) \cdots \psi_N(x)]$$

$$\Lambda^T = [\lambda_1(t) \cdots \lambda_N(t)]$$

Here $\Psi(x)$ is chosen to satisfy the boundary conditions. In this case, from Figure 3.6, the boundary conditions are $\frac{dp'}{dx}(x_L,t) = 0$ and $p'(0,t) = 0$ (close-open condition). Therefore, the basis functions $\{\psi_i(x)\}$ are of the form

$$\psi_i(x) = \sin(k_i x + \phi_i)$$

where k_i and ϕ_i represents the wave numbers and the spatial mode shapes. Moreover, the following relations hold

$$k_i = \frac{1}{x_L}\left[\frac{\pi}{2} + (i-1)\pi\right] \quad i = 1, 2, \ldots, N \tag{3.34}$$

$$\phi_i = n\pi \quad \forall n \geq 0,\ i \geq 1$$

In fact, from the definition of $\{\psi_i(x)\}$, they satisfy

$$\frac{\partial^2 \Psi}{\partial x^2} = -K^2\,\Psi \tag{3.35}$$

where

$$K = \begin{bmatrix} k_1 & & \\ & \ddots & \\ & & k_N \end{bmatrix}$$

Thus, substitute equation (3.33) in (3.32)

$$\Psi^T \ddot{\Lambda} + [\bar{u}^2 - \bar{c}^2] \frac{d^2\Psi^T}{dx^2}\Lambda + 2\bar{u}\frac{d\Psi^T}{dx}\dot{\Lambda} = \frac{(\gamma-1)}{\bar{p}\pi b^2}\left[\frac{dq'_G}{dt}\delta(x-x_G) + \bar{u}q'_G(t)\frac{d\delta(x-x_G)}{dx}\right] \tag{3.36}$$

and by multiplying Ψ and integrating with respect to x from 0 to x_L, the next relation is derived

$$\int_0^{x_L} \Psi\Psi^T dx\ddot{\Lambda} + [\bar{u}^2 - \bar{c}^2]\int_0^{x_L} \Psi\frac{d^2\Psi^T}{dx^2}dx\Lambda + 2\bar{u}\int_0^{x_L}\Psi\frac{d\Psi^T}{dx}dx\dot{\Lambda} =$$

$$\frac{(\gamma-1)}{\bar{p}\pi b^2}\left[\frac{dq'_G}{dt}\int_0^{x_L}\Psi\delta(x-x_G)\,dx + \bar{u}q'_G(t)\int_0^{x_L}\Psi\frac{d\delta(x-x_G)}{dx}dx\right] \tag{3.37}$$

Now, let

$$\begin{aligned} \Gamma_1 &= \int_0^{x_L}\Psi\Psi^T dx \\ \Gamma_2 &= \int_0^{x_L}\Psi\frac{d\Psi^T}{dx}dx \end{aligned} \tag{3.38}$$

So, simplifying equation (3.37) and substituting (3.38), we have

$$\ddot{\Lambda}(t) + 2\bar{u}\Gamma_1^{-1}\Gamma_2\dot{\Lambda}(t) - [\bar{u}^2 - \bar{c}^2]K^2\Lambda(t) = \frac{(\gamma-1)}{\bar{p}\pi b^2}\Gamma_1^{-1}\left[\Psi(x_G)\,\frac{dq'_G}{dt}(t) + \bar{u}\,\Psi'(x_G)\,q'_G(t)\right] \tag{3.39}$$

Note that equation (3.39) represents a linear mapping from the perturbation of heat-release rate q'_G to the amplitudes of the acoustics modes $\{\lambda_i(t)\}$. Once $\Lambda(t)$ is given, the pressure fluctuation can be computed from (3.33) since $\{\psi_i(t)\}$ are already known. Finally, the pressure measurement is taken downstream of the flame

at certain location $x = x_{ref}$, so

$$p'_{ref}(t) = p'(x_{ref}, t) = \bar{p}\Psi^T(x_{ref})\Lambda(t) \tag{3.40}$$

On the other hand, based on p' and q'_G a relation can be derived to the velocity of the flow at the flame holder u'_G by (3.29)

$$u'_G(t) = \frac{1}{\gamma}\frac{d\Psi^T}{dx}(x_G)K^{-2}\dot{\Lambda}(t) - \frac{\bar{u}}{\gamma}\Psi^T(x_G)\Lambda(t) + \sigma\frac{\gamma-1}{\gamma}\frac{q'_G(t)}{\bar{p}\,\pi b^2} \tag{3.41}$$

Therefore, the final state-space acoustic mapping is derived

$$\begin{bmatrix} \dot{x}_1 \\ \dot{x}_2 \end{bmatrix} = \begin{bmatrix} -\Upsilon_1 & I_N \\ -\Upsilon_2 & 0_N \end{bmatrix}\begin{bmatrix} x_1 \\ x_2 \end{bmatrix} + \begin{bmatrix} \Upsilon_3 \\ \Upsilon_4 \end{bmatrix} q'_G(t)$$

$$\begin{bmatrix} p'_{ref}(t) \\ u'_G(t) \end{bmatrix} = \begin{bmatrix} \bar{p}\Psi^T(x_{ref}) & 0 \\ \Omega_2 - \Omega_1\Upsilon_1 & \Omega_1 \end{bmatrix}\begin{bmatrix} x_1 \\ x_2 \end{bmatrix} + \begin{bmatrix} 0 \\ \Omega_1\Upsilon_3 + \Omega_3 \end{bmatrix} q'_G(t) \tag{3.42}$$

where

$$\begin{aligned} \Omega_1 &= \frac{1}{\gamma}\frac{d\Psi^T}{dx}(x_G)K^{-2} \\ \Omega_2 &= -\frac{\bar{u}}{\gamma}\Psi^T(x_G) \\ \Omega_3 &= \sigma\frac{\gamma-1}{\gamma}\frac{1}{\bar{p}\,\pi b^2} \end{aligned} \tag{3.43}$$

and

$$\begin{aligned} \Upsilon_1 &= 2\bar{u}\Gamma_1^{-1}\Gamma_2 \\ \Upsilon_2 &= (\bar{c}^2 - \bar{u}^2)K^2 \\ \Upsilon_3 &= \frac{\gamma-1}{\bar{p}\,\pi b^2}\Gamma_1^{-1}\Psi(x_G) \\ \Upsilon_4 &= \frac{\bar{u}(\gamma-1)}{\bar{p}\,\pi b^2}\Gamma_1^{-1}\Psi'(x_G) \end{aligned} \tag{3.44}$$

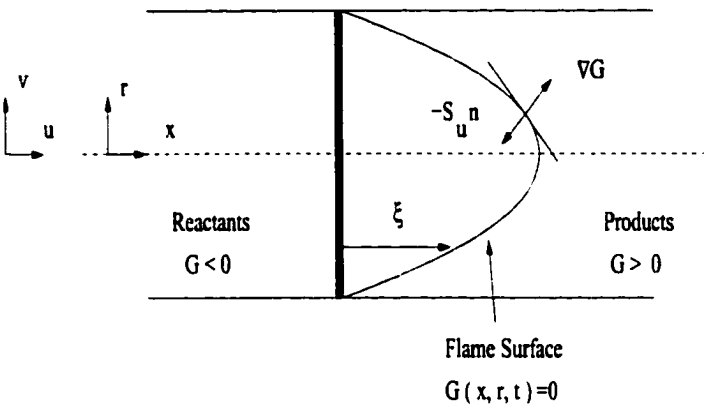

Figure 3.7: MIT Model: Flame Interaction.

3.2.2.2 Flame Dynamics

The flame dynamics are obtained under the following assumptions

- The flame is a thin interface separating reactants and products;
- The flame moves at a constant velocity with respect to the reactants in the direction normal to its surface;
- The effects of expansion and vorticity generation across the flame front on the flow are negligible;
- The flow field and the flame wrinkling are axisymmetric; and
- The flame is insensitive to pressure perturbations.

With these assumptions, the previous derivation for the Cambridge Flame Model holds. However, the flame shape is different in this setup as shown in Figure 3.7; due to a different stabilization mechanism of the flame (perforated plate). Thus the flame initiation surface is given by $G(x, r, t) = x - \xi(r, t)$, recall equation (3.17)

$$-\frac{\partial \xi}{\partial t} + u - v\frac{\partial \xi}{\partial r} = S_u\sqrt{1 + \left(\frac{\partial \xi}{\partial r}\right)^2} \tag{3.45}$$

where (u, v) are the axial and radial velocity components, S_u is the laminar burning velocity, and ξ is the axial flame location. Similarly, the heat release rate q_G is expressed proportional to the flame area

$$q_G = \rho_u S_u \Delta h_r A \tag{3.46}$$

where ρ_U is the mixture density, Δh_r is the heat of reaction per unit mass of the mixture, and A is the flame area. Now the instantaneous flame area is given by

$$A = 2\pi \int_0^b r \sqrt{1 + \left(\frac{\partial \xi}{\partial r}\right)^2} dr \tag{3.47}$$

where b is the flame base radius. Assuming no change of density across $G(x, r, t)$, the oncoming flow is given by $(u, v) = (u_G, 0)$, where u_G denotes the flow velocity at the flame holder. Linearizing equation (3.45), and assuming that $Su << \bar{u}_G$, the flame is nearly parallel to the streamlines and the oscillating components are small compared to the mean values, hence it is obtained

$$\frac{\partial \xi'}{\partial t} = u'_G + S_u \frac{\partial \xi'}{\partial r} \tag{3.48}$$

and

$$A' = 2\pi \int_0^b r \frac{\partial \xi'}{\partial r} dr = 2\pi \int_0^b \xi'(r, t) dr \tag{3.49}$$

with boundary conditions

$$\begin{aligned} \xi'(b, t) &= 0 \quad \forall t \\ \xi'(r, 0) &= 0 \quad \forall r \end{aligned} \tag{3.50}$$

. Substituting (3.48) and (3.49) in (3.46) leads to the next result

$$\begin{aligned} \dot{q'_G} &= \eta \int_0^b \left\{ S_u \frac{\partial \xi'}{\partial r} + u'_G \right\} dr \\ &= \eta \left\{ -S_u \xi'(0, t) + b u'_G(t) \right\} \end{aligned} \tag{3.51}$$

where $\eta = 2\pi\rho_u S_u \Delta h_r$. Next, solving equation (3.48) directly (Laplace Method [51]) by using the previous boundary conditions (3.50), the next relation is obtained

$$\xi'(r,t) = \int_{t-t_r}^{t} u'_G(\tau)d\tau \tag{3.52}$$

where

$$t_r = \frac{b-r}{S_u}$$

Since the effect of high frequency on the flame dynamics is negligible [23], $u'_G(t)$ is assumed to vary slowly, therefore

$$\xi'(r,t) = \int_{t-t_r}^{t} u'_G(\tau)d\tau \approx \frac{b-r}{S_u}u'_G \tag{3.53}$$

Consequently, by equations (3.49) and (3.46), it is deduced that

$$q'_G(t) = \eta\int_0^b \xi'(r,t)dr \approx \eta\frac{b}{2}\xi'(0,t) \tag{3.54}$$

Substituting in equation (3.51), the flame model can be expressed in terms of q'_G and u'_G

$$\dot{q}'_G + \frac{2S_u}{b}q'_G = \eta\frac{b}{4}u'_G \tag{3.55}$$

So, the linear transfer function representing the flame model is given by

$$\frac{Q_G(s)}{U_G(s)} = \frac{\pi\rho_u S_u \Delta h_r \frac{b}{2}}{s + \frac{2S_u}{b}} \tag{3.56}$$

3.2.2.3 Control Configuration

Finally the combustor feedback control system, see Figure 3.6, uses a loudspeaker upstream of the flame holder for active control. Now, the acoustics dynamics (3.42) and flame interactions (3.56) can be linked together with the loudspeaker characteristics to describe the closed-loop control system as shown in Figure 3.8.

Neglecting magnetic inductance, the response of the loudspeaker is assumed to be linear. In general, it can be represented by a second order system:

$$v'_a = \frac{k_a e^{-\tau_a s} s^2}{m_l s^2 + b_l s + k_l} v'_c \tag{3.57}$$

where m_l, b_l and k_l represents the mass, friction and stiffness properties, respectively, of the loudspeaker, k_a the calibration gain, τ_a the associated process delay, v'_a the diaphragm velocity and v'_c the applied voltage. Consequently, two extra terms in the right-hand side of equations (3.29) and (3.30) arise when the acoustic impact of the loudspeaker is modeled. Thus two source terms are added to the momentum and energy equations and hence the acoustic dynamics are altered. Therefore, the actuation of the loudspeaker affects the energy rate at the flame front by altering the mixing process.

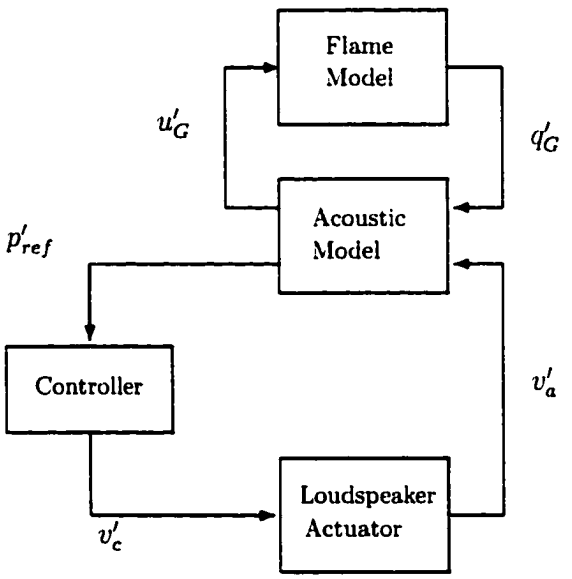

Figure 3.8: MIT Model: Control Feedback Configuration

CHAPTER 4

SENSORS AND ACTUATORS FOR COMBUSTION CONTROL

A review of the most common sensors and actuators used in the control of thermoacoustic instabilities is presented in this chapter. Their basic principles, limitations and advantages are described.

The principle behind active control is to make use of sensors and actuators to disrupt the coherence that brought the instability coupling. Thus, sensors are used to measure representative signals of the instability mechanism, and according to these signals actuators modify the pressure field or the heat release pattern. Nowadays in large-scale gas turbines, passive techniques are preferred to damp thermoacoustical instabilities. Thus acoustic resonators are tuned to match the unstable frequencies seen during the normal operating conditions of the turbine. Active control is still not considered a viable solution in large-scale systems; mainly because of the lack of long-lasting sensors and actuators that could stand the harsh conditions presented in the interior of gas turbines. Therefore, the development of suitable sensors and actuators is a limiting factor in the success of combustion active control. Nevertheless, new technologies are emerging constantly, so robust and long-lasting sensors and actuators that could stand the demand of high performance turbines are just some steps away.

4.1 Sensors

According to the *Rayleigh Criterion* [62], the triggering factor in combustion instabilities is the coupling between acoustic waves and heat-release pattern. In addition, the velocity of the flow at burner, that is related to the pressure oscillations, has also been considered as another possible agent causing the instabilities. Hence, the following quantities are important factors in the development of combustion instabilities:

- Pressure,
- Heat-Release and
- Flow Velocity.

Consequently, a description of the instability can be obtained by sensing the previous signals.

4.1.1 Pressure Sensors

Pressure sensors are employed to measure the acoustic field inside of the combustion chamber; this measurement is usually preferred for feedback control purposes due to the reliability of the sensors. There are two main types of pressure sensors used in control applications:

- **Microphones**: these devices have large bandwidth and high sensitivity. They can measure a wide variety of frequency components with high accuracy. However, they are not designed for harsh working conditions.
- **Pressure Transducers**: these transducers are especially designed for combustion control; so they are internally water-cooled to stand the high temperatures

Figure 4.1: KISTLER Water Cooled Transducer (http://www.kistler.com/combustion_randd_highprec_water.htm).

inside of the combustion chamber. Their sensitivity is not as good as the microphone's but they still provide enough bandwidth to capture low and high frequency instabilities. Figure 4.1 shows a water-cooled pressure transducer manufactured by KISTLER.

4.1.2 Heat-Release Sensors

The heat-released by the flame has been recognized as an important instability agent in combustors. However, there is no method to measure this quantity directly; its estimation is based on readings of chemical radicals liberated by the flame, like CH and OH. So, two basic sensors are commonly used:

- **OH-transducer**: it captures the liberation of the OH-radical based on the emission of light at certain frequency bandwidth. These sensors are especially designed to be mounted along the walls of the combustor chamber, so they are water-cooled for proper operation. The measurement of this sensor is localized, in other words, the reading is done just over certain area window (the surface of the sensor).

- **CH-Photodiode**: this sensor measures the emission of CH by reading a particular light wavelength that this radical emits. Compared with the measurement of the OH-transducer, this sensor measures in a global scale. Unfortunately, this kind of sensor is not designed to be placed in the combustor, it

cannot resist high temperatures. So it is located at certain distance of the combustion chamber and it should have a clear visual path to the flame by a window in the combustor chamber.

4.1.3 Flow Velocity Sensors

Before the reaction zone, the velocity of the flow is related to the pressure waves in the chamber. In addition, oscillations on the oncoming flow to the flame front causes perturbations on the heat-release. Thus a measurement of this quantity will give a good indication of the instability coupling. The sensor used for this purpose is the *anemometer*. The working principle of this sensor is based on the cooling effect of a flow on a heated body. The anemometer measures velocity at a point (one-dimensional) and provides continuous velocity time series. Nevertheless, the sensor-probe can be configurated in such a way that two or three dimensional velocity components are measured. The disadvantage of this sensor is that it is not pretty robust and cannot be located near the reaction zone. More advanced measurement techniques for three-dimensional flow velocity, like PIV (particle imaging velocimetry) and PDPA (phase doppler particle anemometry), are available, however they are only applied for diagnostics purpose since the measurement cannot be processed in real time.

4.2 Actuators

Actuators are the most limiting factor in the development of active control strategies. Their objective is to modify certain property of the thermoacoustic coupling in such a way that the instability loop is disrupted. According to the quantity that they modify in the chamber, they can be divided into two main categories:

- Acoustic Modulation and
- Fuel Modulation.

4.2.1 Acoustic Modulation Control

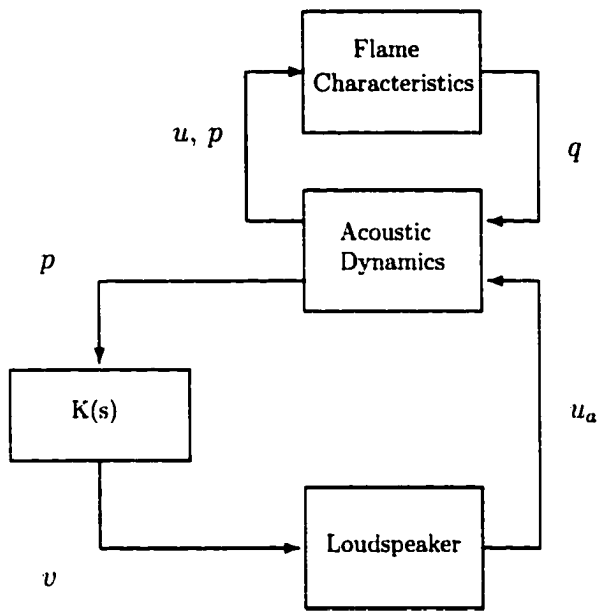

Figure 4.2: Diagram of Control with Acoustic Actuator

The objective of acoustic modulation is to alter the pressure field in such a way that the mixture fuel-air is modulated before entering the reaction zone in the flame front. Therefore, the heat-release is affected and the instability coupling could be broken. Generally the instability frequencies are in the range 50 to 400Hz, thus standard low-frequency loudspeakers can be used as actuators for this task. A nice feature of loudspeakers is that they have a fairly linear response neglecting the effects of magnetic inductance. So they can be modeled by a simple second order transfer function (as shown in the previous chapter).

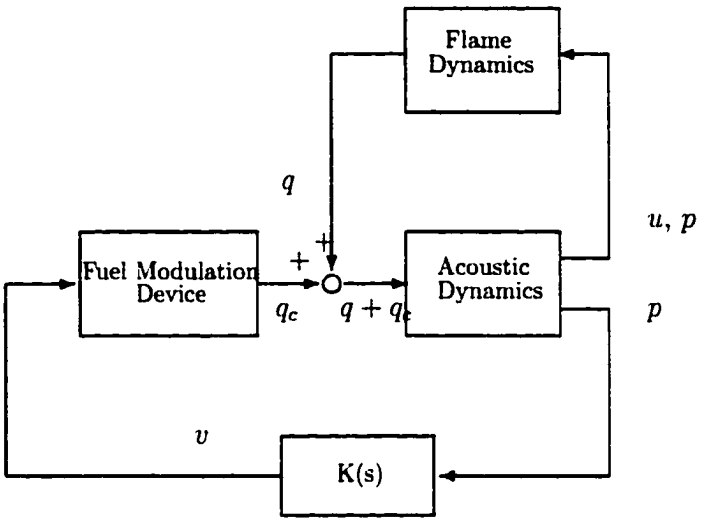

Figure 4.3: Diagram of Control with Fuel Actuator

Loudspeakers present two main disadvantages: the space required which is crucial in modern combustors and the necessity of cooling mechanisms during normal combustor operation. However, their linear response makes them suitable to explore initially new control strategies in test-rigs. The combustor diagram with acoustic control is shown in Figure 4.2.

4.2.2 Fuel Modulation Control

The idea behind fuel modulation is to oscillate part of the fuel stream to the reaction zone, so that the burning rate at the flame front is altered, hence the characteristics of the heat release can be decoupled from the pressure waves oscillations. The combustor interactions with fuel modulation control are depicted in Figure 4.3.

Now, the modulation of the fuel can be achieved basically with two types of actuators:

- Open-Closed Valve (Automotive Fuel Injector) or
- Proportional Valve (DDV Moog Valve).

Figure 4.4: BOSCH Fuel Injector (http://www.boschusa.com/Business/ Automotive/ Gasoline/InjectorEV14/).

4.2.2.1 Fuel Injector

All commercial fuel injectors are designed mainly for automotive design and none for combustion control. So, their response obeys to the requirements given by the automobile industry. Consequently, fuel injectors do not have a proportional response, their response is just fully open or fully closed (discrete). Therefore the fuel injectors have only two control parameters to adjust: frequency and duty-cycle.

Fuel injectors have certain characteristics that make them attractive for combustion control. Since they are originally designed to work in cars, they are particularly suited to run in liquid-fueled combustors. Moreover, they provide a fairly large frequency response (roughly 50 to 700Hz) compared to proportional valves. However, their response is dependent also on the duty-cycle; the frequency bandwidth changes according with the duty-cycle. Thus the best response is generally given from a 30 to 75 % duty-cycle [1]. A widely used automotive fuel injector produced by BOSCH is shown in Figure 4.4.

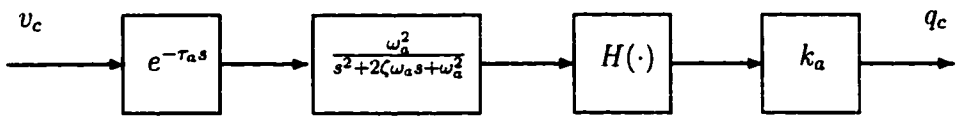

Figure 4.5: Nonlinear Dynamics of Fuel Injector

The dynamics of a fuel injector can be modeled by a second order transfer function in series with a nonlinear block. The nonlinear behavior of the fuel injectors can be characterized by a relay-type nonlinearity, i.e., above certain threshold voltage the fuel injector is completely open, below it the injector is closed. Thus a representation of this nonlinearity can be given by

$$H(v) = \begin{cases} 1 & v \geq v_{th} \\ 0 & v < v_{th} \end{cases}$$

where v_{th} is a specified threshold voltage. The linear dynamics can be modeled by a second order transfer function between the voltage applied v_c and the heat release produced q_c

$$q_c = \frac{k_a e^{-\tau_a s}}{(1/\omega_a)^2 s^2 + 2(\zeta/\omega_a)s + 1} v_c \tag{4.1}$$

where k_a is a calibration constant, ζ the damping coefficient, ω_a the bandwidth and τ_a the associated time delay. So, the complete nonlinear model for the fuel injector is described in Figure 4.5.

4.2.2.2 Proportional Valves

Proportional valves for combustion control have many advantages, they can modulate continuously the fuel into the burner and the space that they require is usually small, so there is no problem locating them inside of the combustor. However, the main problem with proportional valves is its frequency response limitation. In general, these valves cannot go higher than 200Hz, which is very restricting since in

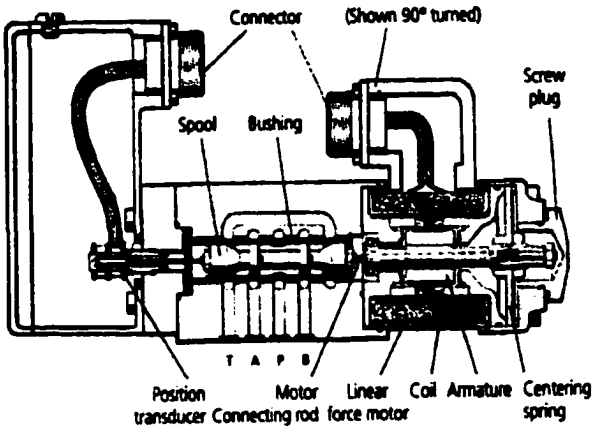

Figure 4.6: Moog DDV Schematic (http://www.moog.com/imc/literature /hydraulic/d633and4.pdf).

some cases the instability frequencies are located around 200 to 350Hz. Thus, these valves cannot respond adequately for these cases. Moreover, these valves are extremely costly and their life-span is also limited.

The only company that manufactures these valves is the *Moog* Corporation in Germany. This company has two kinds of valves available: Servo-valves and DDV (direct driven valves). The servo-valve is generally slower than the DDV, since the first one has an intrinsic control loop to position the piston cylinder. The DDV operation is relatively simple: a linear force motor is the driving mechanism of the valve; the armature of the motor is connected to the spool (piston cylinder); depending on the polarity of the input current the armature/spool is driven either side. The schematic of the DDV is shown in Figure 4.6. On the other hand, the Moog company has already a complete system set for active combustion control. However, this control set uses only simple phase-delay control.

CHAPTER 5

ACOUSTIC PROPERTIES OF COMBUSTION CHAMBERS

The objective of this chapter is to introduce the notion of the *Riemann Invariants* to characterize the acoustic properties of the combustion chamber. This characterization is essential in the development of the experimental combustor model in Chapter 7. Using this concept, the pressure and velocity fluctuations are represented by two-waves traveling along the combustion chamber. The characteristics of the Riemann Invariants are obtained from solving the Euler equations describing the conservation, momentum and energy relations inside of the chamber. A detailed derivation of this concept is presented in this chapter.

5.1 Basic Assumptions

The acoustic dynamics inside the combustor shield are complex and basically governed by the Euler (conservation) equations. These equations describe the relations among quantities as pressure, density, velocity and energy. In order to simplify the acoustic derivation, the following assumptions were made:

- **Isentropic and homentropic flow**: the assumption of homentropic flow has two underlying assumptions, the entropy of each particle remains constant and the entropy is the same for each particle. The first condition, isentropy, is violated in a gas turbine, because the flame adds heat to the fluid. However, if the flame front is treated as a discontinuity, the flow in front of and behind

the flame may be considered to be isentropic. Homentropy is equivalent to a uniform temperature distribution on both sides of the flame. This is not true, but for premixed, turbulent flame the temperature differences are sufficiently low.

- **Perfect Gas**: the pressure in a gas turbine combustion chamber is significantly higher than atmospheric, ranging from 15 to 30 bar, but still low enough to maintain the relation for a perfect gas as a good approximation for the state equation.

- **One dimensional flow**: there is no reason to assume that the flow is strongly rotational in front of the burners. In annular combustion chambers the burners are configured with an alternative positive and negative sense of rotation, creating a nearly irrotational flow in the chamber. This assumption means that acoustic perturbations are planar waves. The wave front (defined as a surface at which all points have the same amplitude and phase of the acoustic pressure and velocity) is a plane normal to the direction of wave propagation.

- **Negligible viscosity and heat conduction**: laminar viscosity and heat conduction can be neglected, simply because the turbulent exchange of heat and momentum is several orders of magnitude larger.

- **Negligible body forces**: gravity forces are small enough to be neglected.

- **No interaction with boundaries**: the combustion chamber is assumed to be rigid walled, therefore there is no interaction between structural and fluidic oscillations.

5.2 Acoustic Dynamics

With the assumptions given in the last section, the Euler equations can be written down as

Conservation of mass

$$\frac{\partial \rho}{\partial t} + \frac{\partial (u\rho)}{\partial x} = 0 \tag{5.1}$$

Conservation of momentum

$$\rho \frac{\partial u}{\partial t} + \rho u \frac{\partial u}{\partial x} + \frac{\partial p}{\partial x} = 0 \tag{5.2}$$

Energy equation

$$\frac{\partial p}{\partial t} + \gamma p \frac{\partial u}{\partial x} + u \frac{\partial p}{\partial x} = (\gamma - 1) q \tag{5.3}$$

where p is the pressure, u the velocity of the flow, ρ the density, γ the ratio of specific heat capacities and q the heat-release rate per unit volume. Since only one dimensional flow is assumed, the coordinate x is related to the axial displacement along the combustion chamber. On the other hand, assume that the gases on both sides of the combustor behave as perfect gases, and the quantities in equations (5.1), (5.2) and (5.3) can be separated in mean $\bar{(\cdot)}$ and fluctuating $(\cdot)'$ components

$$\begin{aligned} \rho(x,t) &= \bar{\rho}(x) + \rho'(x,t) \\ p(x,t) &= \bar{p}(x) + p'(x,t) \\ u(x,t) &= \bar{u}(x) + u'(x,t) \\ q(x,t) &= \bar{q}(x) + q'(x,t) \end{aligned} \tag{5.4}$$

To have a tractable problem, assume that the perturbation components are small variations about the mean flow. Next, substitute (5.4) into equations (5.1), (5.2) and (5.3) to get

$$\frac{\partial \rho'}{\partial t} + \frac{\partial (\bar{u} + u')(\bar{\rho} + \rho')}{\partial x} = 0$$

$$(\bar{\rho}+\rho')\frac{\partial u'}{\partial t}+(\bar{\rho}+\rho')(\bar{u}+u')\frac{\partial(\bar{u}+u')}{\partial x}+\frac{\partial(\bar{p}+p')}{\partial x}=0$$

$$\frac{\partial p'}{\partial t}+\gamma(\bar{p}+p')\frac{\partial(\bar{u}+u')}{\partial x}+(\bar{u}+u')\frac{\partial(\bar{p}+p')}{\partial x}=(\gamma-1)(\bar{q}+q')$$

Expanding the terms inside of the brackets and neglecting second order terms, two sets of equations are obtained. First, for mean values

$$\bar{\rho}\frac{\partial\bar{u}}{\partial x}+\bar{u}\frac{\partial\bar{\rho}}{\partial x}=0$$

$$\bar{\rho}\bar{u}\frac{\partial\bar{u}}{\partial x}+\frac{\partial\bar{p}}{\partial x}=0$$

$$\gamma\bar{p}\frac{\partial\bar{u}}{\partial x}+\bar{u}\frac{\partial\bar{p}}{\partial x}=(\gamma-1)\bar{q}$$

and then for the fluctuations

$$\begin{aligned}
&\frac{\partial\rho'}{\partial t}+\bar{\rho}\frac{\partial u'}{\partial x}+\bar{u}\frac{\partial\rho'}{\partial x}+\frac{\partial\bar{\rho}}{\partial x}u'+\frac{\partial\bar{u}}{\partial x}\rho'=0\\
&\bar{\rho}\frac{\partial u'}{\partial t}+\bar{\rho}\bar{u}\frac{\partial u'}{\partial x}+\bar{\rho}\frac{\partial\bar{u}}{\partial x}u'+\bar{u}\frac{\partial\bar{u}}{\partial x}\rho'+\frac{\partial p'}{\partial x}=0\\
&\frac{\partial p'}{\partial t}+\gamma\bar{p}\frac{\partial u'}{\partial x}+\gamma\frac{\partial\bar{u}}{\partial x}p'+\frac{\partial\bar{p}}{\partial x}u'+\bar{u}\frac{\partial p'}{\partial x}=(\gamma-1)q'
\end{aligned}\tag{5.5}$$

Now, also assume that the heat released by the flame is spatially localized at a specific point in the flame front $x=x_G$, in other words

$$q'(x,t)=\frac{q'_G(t)}{\pi b^2}\delta(x-x_G)\tag{5.6}$$

where q'_G denotes the heat release rate, b the radius of the shield and $\delta(\cdot)$ represents the Dirac delta function. Under this assumption, it can be proved [3] that the mean variables are essentially constant over the length of the combustor except for a step change at $x=x_G$, meanwhile the derivatives will be of the order of $M^2=\bar{u}^2/\bar{c}^2$. Therefore for low-Mach-number flows these derivatives can be neglected. Also, for this condition the effect of step change in the pressure is negligible compared to the

change in the mean velocity or mean density. So, the set of equations (5.5) can be simplified as

$$\frac{\partial \rho'}{\partial t} + \bar{\rho}\frac{\partial u'}{\partial x} + \bar{u}\frac{\partial \rho'}{\partial x} = 0 \tag{5.7}$$

$$\bar{\rho}\frac{\partial u'}{\partial t} + \bar{\rho}\bar{u}\frac{\partial u'}{\partial x} + \frac{\partial p'}{\partial x} = 0 \tag{5.8}$$

$$\frac{\partial p'}{\partial t} + \gamma\bar{p}\frac{\partial u'}{\partial x} + \bar{u}\frac{\partial p'}{\partial x} = \frac{(\gamma-1)}{\pi b^2} q'_G(t)\delta(x - x_G) \tag{5.9}$$

It is important to mention that (5.9) has a discontinuity at $x = x_G$, so the solutions to the set of linear partial differential equations at $x = x_G$ must be treated as a limit case. Finally, equations (5.8) and (5.9) are combined together to obtain a single partial differential equation relating p' to q'_G. Now, differentiate equation (5.9) with respect to t to obtain

$$\frac{\partial^2 p'}{\partial t^2} + \gamma\bar{p}\frac{\partial^2 u'}{\partial x \partial t} + \bar{u}\frac{\partial^2 p'}{\partial x \partial t} = \frac{(\gamma-1)}{\pi b^2}\frac{dq'_G}{dt}\delta(x - x_G) \tag{5.10}$$

Next, differentiate equation (5.9) with respect to x

$$\frac{\partial^2 p'}{\partial t \partial x} + \gamma\bar{p}\frac{\partial^2 u'}{\partial x^2} + \bar{u}\frac{\partial^2 p'}{\partial x^2} = \frac{(\gamma-1)}{\pi b^2} q'_G \frac{d\delta(x - x_G)}{dx}$$

Multiply last equation by $\bar{u}$ and add to (5.10)

$$\frac{\partial^2 p'}{\partial t^2} + 2\bar{u}\frac{\partial^2 p'}{\partial t \partial x} + \bar{u}^2\frac{\partial^2 p'}{\partial x^2} + \bar{c}^2\left[\bar{\rho}\frac{\partial^2 u'}{\partial x \partial t} + \bar{\rho}\bar{u}\frac{\partial^2 u'}{\partial x^2}\right] =$$

$$\frac{(\gamma-1)}{\pi b^2}\left[\frac{dq'_G}{dt}\delta(x - x_G) + \bar{u}q'_G(t)\frac{d\delta(x - x_G)}{dx}\right] \tag{5.11}$$

Take now equation (5.8) and differentiate it with respect to x

$$\frac{\partial^2 p'}{\partial x^2} + \bar{\rho}\frac{\partial^2 u'}{\partial t \partial x} + \bar{\rho}\bar{u}\frac{\partial^2 u'}{\partial x^2} = 0$$

Substitute the last equation in (5.11) and group terms to get

$$\frac{\partial^2 p'}{\partial t^2} + [\bar{u}^2 - \bar{c}^2]\frac{\partial^2 p'}{\partial x^2} + 2\bar{u}\frac{\partial^2 p'}{\partial t \partial x} = \frac{(\gamma-1)}{\pi b^2}\left[\frac{dq'_G}{dt}\delta(x - x_G) + \bar{u}q'_G(t)\frac{d\delta(x - x_G)}{dx}\right] \tag{5.12}$$

Thus, equation (5.12) describes a second order hyperbolic partial differential equation whose solution is in nature infinite dimensional.

5.3 Riemann Invariants

Now, only the homogeneous part of equation (5.12) will be analyzed

$$\frac{\partial^2 p'}{\partial t^2} + [\bar{u}^2 - \bar{c}^2]\frac{\partial^2 p'}{\partial x^2} + 2\bar{u}\frac{\partial^2 p'}{\partial t \partial x} = 0 \tag{5.13}$$

Last equation can be factored as

$$\left(\frac{\partial}{\partial t} + (\bar{c} + \bar{u})\frac{\partial}{\partial x}\right)\left(\frac{\partial}{\partial t} - (\bar{c} - \bar{u})\frac{\partial}{\partial x}\right) p' = 0 \tag{5.14}$$

This one dimensional homogeneous differential equation with constant coefficients can be solved using the method of d'Alembert [51]. According to d'Alembert, a new coordinate system is introduced

$$\begin{aligned} \xi &= t - \frac{1}{\bar{c} + \bar{u}} x \\ \eta &= t + \frac{1}{\bar{c} - \bar{u}} x \end{aligned} \tag{5.15}$$

So, instead of solving for $p'(x,t)$, the solution is give for $p'(\xi,\eta)$. Rewriting the derivatives in terms of ξ and η gives

$$\begin{aligned} \frac{\partial p'}{\partial t} &= \frac{\partial p'}{\partial \xi}\frac{\partial \xi}{\partial t} + \frac{\partial p'}{\partial \eta}\frac{\partial \eta}{\partial t} = \frac{\partial p'}{\partial \xi} + \frac{\partial p'}{\partial \eta} \\ \frac{\partial^2 p'}{\partial t^2} &= \frac{\partial^2 p'}{\partial \xi^2} + 2\frac{\partial^2 p'}{\partial \xi \partial \eta} + \frac{\partial^2 p'}{\partial \eta^2} \\ \frac{\partial p'}{\partial x} &= \frac{\partial p'}{\partial \xi}\frac{-1}{\bar{c} + \bar{u}} + \frac{\partial p'}{\partial \eta}\frac{1}{\bar{c} - \bar{u}} \\ \frac{\partial^2 p'}{\partial x^2} &= \frac{\partial^2 p'}{\partial \xi^2}\left(\frac{-1}{\bar{c} + \bar{u}}\right)^2 - \frac{\partial^2 p'}{\partial \xi \partial \eta}\frac{2}{\bar{c}^2 - \bar{u}^2} + \frac{\partial^2 p'}{\partial \eta^2}\left(\frac{1}{\bar{c} - \bar{u}}\right)^2 \qquad (5.16) \\ \frac{\partial^2 p'}{\partial x \partial t} &= \frac{\partial^2 p'}{\partial \eta^2}\frac{-1}{\bar{c} + \bar{u}} - \frac{\partial^2 p'}{\partial \xi \partial \eta}\frac{2\bar{u}}{\bar{c}^2 - \bar{u}^2} + \frac{\partial^2 p'}{\partial \eta^2}\frac{1}{\bar{c} - \bar{u}} \qquad (5.17) \end{aligned}$$

Substituting these equations into equation (5.13) yields

$$\frac{\partial^2 p'}{\partial t^2} + [\bar{u}^2 - \bar{c}^2]\frac{\partial^2 p'}{\partial x^2} + 2\bar{u}\frac{\partial^2 p'}{\partial t \partial x} = 0 \quad \Longrightarrow \quad \frac{\partial^2 \tilde{p}}{\partial \xi \partial \eta} = 0 \tag{5.18}$$

This means that $\frac{\partial \tilde{p}}{\partial \eta}$ is independent of ξ. Therefore, $\frac{\partial \tilde{p}}{\partial \eta}$ is just a function of η

$$\frac{\partial \tilde{p}}{\partial \eta} = G^*(\eta) \tag{5.19}$$

where G^* denotes an unknown function of η. After integrating equation (5.19) a solution for $\tilde{p}(\xi, \eta)$ is obtained

$$\tilde{p}(\xi, \eta) = G(\eta) + F(\xi) \tag{5.20}$$

Note that the constant of integration may depend on ξ, therefore a function $F(\xi)$ is used as constant of integration. Hence, the homogeneous solution to (5.12) is given by

$$p'(x,t) = F\left(t - \frac{x}{\bar{c} + \bar{u}}\right) + G\left(t + \frac{x}{\bar{c} - \bar{u}}\right) \tag{5.21}$$

where the so called *Riemann Invariants* F and G are arbitrary functions of their arguments. Looking at the arguments it can be seen that F represents a *disturbance traveling downstream and* G *a disturbance going upstream* in the flow. In a similar way the wave equation for $u'(x,t)$ can be solved. Replacing the Riemann Invariants by new ones which only differ by the constant factor $\bar{\rho}\bar{c}$, the pressure and velocity fluctuations can be written as

$$p'(x,t) = \bar{\rho}\bar{c}\left[f\left(t - \frac{x}{(1+M)\bar{c}}\right) + g\left(t + \frac{x}{(1-M)\bar{c}}\right)\right] \tag{5.22}$$

$$u'(x,t) = f\left(t - \frac{x}{(1+M)\bar{c}}\right) - g\left(t + \frac{x}{(1-M)\bar{c}}\right) \tag{5.23}$$

Although, it would not be completely correct physically, we could consider the Riemann Invariants as *two waves going in opposite directions.* Apart from the $\bar{\rho}\bar{c}$

factor, the *acoustic pressure is found by adding both waves and the acoustic velocity by subtracting the waves.* These easy transitions between the Riemann Invariants and the fluctuating pressure and velocity are very useful in practice.

On the other hand, if time dependence is assumed to be of the exponential form $e^{i\omega t}$, then equation (5.22) becomes

$$\frac{p'(x,t)}{\bar{\rho}\bar{c}} = \hat{f}_0 exp\left[i\omega\left(t - \frac{x}{(1+M)\bar{c}}\right)\right] + \hat{g}_0 exp\left[i\omega\left(t + \frac{x}{(1-M)\bar{c}}\right)\right] \tag{5.24}$$

where $\hat{f}_0$ and $\hat{g}_0$ are the Fourier transforms of the Riemann Invariants at location $x = 0$. Using the wave number defined as $k_{x+} = \frac{\omega/\bar{c}}{1+M}$ and $k_{x-} = \frac{-\omega/\bar{c}}{1-M}$ the pressure and the velocity can be written as:

$$\begin{aligned} \frac{p'(x,t)}{\bar{\rho}\bar{c}} &= \hat{f}_0 e^{i(\omega t - k_{x+}x)} + \hat{g}_0 e^{i(\omega t - k_{x-}x)} \\ u'(x,t) &= \hat{f}_0 e^{i(\omega t - k_{x+}x)} - \hat{g}_0 e^{i(\omega t - k_{x-}x)} \end{aligned} \tag{5.25}$$

The values of $\hat{f}_0$ and $\hat{g}_0$ can be found if the boundary conditions are known. Note that in these equations:

$$f(x,t) = \hat{f}_0 e^{i(\omega t - k_{x+}x)} \tag{5.26}$$

$$g(x,t) = \hat{g}_0 e^{i(\omega t - k_{x-}x)} \tag{5.27}$$

Thus, equations (5.25) can also be written as:

$$\begin{aligned} \frac{p'(x,t)}{\bar{\rho}\bar{c}} &= \left[\hat{f}_0 e^{-ik_{x+}x} + \hat{g}_0 e^{-ik_{x-}x}\right] e^{i\omega t} \\ u'(x,t) &= \left[\hat{f}_0 e^{-ik_{x+}x} - \hat{g}_0 e^{-ik_{x-}x}\right] e^{i\omega t} \end{aligned} \tag{5.28}$$

or,

$$\begin{aligned} \frac{p'(x=x_j,t)}{\bar{\rho}\bar{c}} &= \left[\hat{f}_j + \hat{g}_j\right] e^{i\omega t} \\ u'(x=x_j,t) &= \left[\hat{f}_j - \hat{g}_j\right] e^{i\omega t} \end{aligned} \tag{5.29}$$

with

$$\begin{aligned} \hat{f}_j &= \hat{f}_0 e^{-ik_{z+}x_j} \\ \hat{g}_j &= \hat{g}_0 e^{-ik_{z-}x_j} \end{aligned} \tag{5.30}$$

Hence, it can be concluded that for a fixed time, *the difference between the Riemann Invariants at two different axial locations is just a phase shift.*

In the case of an unstable condition of the combustion chamber, the pressure oscillations present a periodic behavior (limit-cycle oscillation). Therefore, the properties presented for the Riemann Invariants can be applied to obtain the $\hat{f}$ and $\hat{g}$ waves from pressure measurements; this method is called Multi-Microphone Method [59, 68].

CHAPTER 6

OPTIMAL CONTROL

In this chapter a brief overview of optimal control theory is presented. First, the basic modern control concepts are introduced. Guidelines for robust and performance control design are outlined, as well as Linear Fractional Transformation benchmark for control synthesis. In addition, controller reduction by Balance Truncation is also summarized. Finally, optimal control designs such as LQG and $\mathcal{H}_\infty$ are briefly introduced. This chapter was constructed using the following references [43, 80].

6.1 Control Basics

A finite dimensional linear time invariant system can be represented by the following linear constant coefficient differential equations:

$$\begin{aligned} \dot{x} &= Ax + Bu,\ x(t_0) = x_0 \\ y &= Cx + Du \end{aligned} \tag{6.1}$$

where $x(t) \in \mathcal{R}^n$, $u(t) \in \mathcal{R}^m$, $y(t) \in \mathcal{R}^p$, and the A,B,C and D are real constant matrices. The corresponding transfer function from u to y is defined as

$$Y(s) = G(s)U(s)$$

where $Y(s)$ and $U(s)$ are the Laplace transformation of $y(t)$ and $u(t)$ respectively, and

$$G(s) = C(sI - A)^{-1}B + D \tag{6.2}$$

Moreover, the following notation is used:

$$G(s) = \left[\begin{array}{c|c} A & B \\ \hline C & D \end{array}\right] \tag{6.3}$$

Definition 6.1 *The dynamical system (6.1) is said to be stable if all the eigenvalues of A are in the open left half plane; that is, $Re\lambda(A) < 0$*

Controllability and observability are two important concepts for modern control, each of them represents physical capabilities of our system which can be linked to the state-space representation.

Definition 6.2 *The dynamical system (6.1) is said to be controllable if, for any initial state $x(0) = x_0$, $t_1 > 0$ and final state x_1, there exists an input $u(\cdot)$ such that the solution of (6.1) satisfies $x(t_1) = x_1$.*

This concept, when the system is stable, can be related to the existence of a positive definite solution of following Lyapunov equation

$$AP + PA^T + BB^T = 0, \quad P > 0 \tag{6.4}$$

where P is called *controllability Gramian.*

Definition 6.3 *The dynamical system (6.1) is said to be observable if, for any $t_1 > 0$, the initial state $x(0) = x_0$ can be determined from the time history of the input $u(t)$ and the output $y(t)$ in the interval $[0, t_1]$.*

Similarly, observability, when A is stable, is achieved if and only if there exists $Q > 0$ such that

$$A^TQ + QA + C^TC = 0 \tag{6.5}$$

where Q is called *observability Gramian.*

Assume that $G(s)$ is a real rational transfer matrix that is proper. Then a state-space model (A, B, C, D) such that

$$G(s) = \left[\begin{array}{c|c} A & B \\ \hline C & D \end{array}\right]$$

is called a realization of $G(s)$. Note that $G(s)$ can have many different realizations which can be obtained through a coordinate transformation $\hat{x} = Tx$

$$G(s) = \left[\begin{array}{c|c} TAT^{-1} & TB \\ \hline CT^{-1} & D \end{array}\right]$$

where T is a square nonsingular matrix with compatible dimensions. Of especial interest is a realization that has the smallest dimension possible, which is called "minimal realization". This kind of realization is related to the characteristics of the system.

Definition 6.4 *A state-space description (A, B, C, D) of $G(s)$ is said to be minimal realization of $G(s)$ if and only if the system is both controllable and observable.*

6.2 LQG Control Technique

Suppose that the plant model is given by

$$\begin{aligned} \dot{x} &= Ax + Bu + \Gamma w \\ y &= Cx + Du + v \end{aligned} \tag{6.6}$$

where $w(t)$ and $v(t)$ represent probabilistic knowledge about the plant disturbances, and Γ is a constant matrix. The disturbances w and v are assumed to be zero mean Gaussian white noises with covariance matrices:

$$\mathrm{E}\{w(t)w^T(t)\} = Q_n \geq 0 \tag{6.7}$$

$$\mathrm{E}\{v(t)v^T(t)\} \;=\; R_n \;\geq 0 \tag{6.8}$$

and uncorrelated

$$\mathrm{E}\{v(t)w^T(t+\tau)\} = 0 \quad \forall t,\ \tau \tag{6.9}$$

where $\mathrm{E}\{\cdot\}$ is the probabilistic expectation operator.

The Linear Quadratic Gaussian (LQG) control problem is then defined as to devise a control law that minimizes the cost function:

$$J = \mathrm{E}\left\{\int_0^\infty \left[x^T Q x + u^T R u\right] dt\right\} \tag{6.10}$$

for the plant given in (6.6). Using the separation principle the LQG control problem can be decomposed into two subproblems:

- Application of the standard deterministic LQR (Linear Quadratic Regulator) control problem

$$\min_u \int_0^\infty \left[x^T Q x + u^T R u\right] dt \tag{6.11}$$

  whose solution is a state feedback control law.

- Obtaining of an optimal estimate $\hat{x}$ of states x minimizing

$$\mathrm{E}\left\{(x-\hat{x})^T(x-\hat{x})\right\} \tag{6.12}$$

  using the Kalman filter theory.

Hence, the control design requires to specify the parameters Q and R related to the LQR problem, and Q_n and R_n parameters needed to compute the optimal Kalman estimator.

6.3 Transfer Function Norms

In general, the main goal of a control system is to guarantee certain performance specifications while keeping internal stability. This performance can be translated by means of looking at characteristics of the controlled system. One way to 'measure' this performance is by using a *norm* of the feedback system. The norm election obviously depends on each particular situation, since each norm represents different physical properties. In this way, the L_2 norm of a transfer function $G(s)$ is defined as

$$\|G\|_2 = \sqrt{\frac{1}{2\pi}\int_{-\infty}^{\infty} trace\{G^*(j\omega)G(j\omega)\}d\omega} \tag{6.13}$$

This norm is usually associated with "energy" according to Parseval's Theorem. On the other hand, a different measure for a transfer function $G(s)$ is in terms of the L_∞ norm

$$\|G\|_\infty = \sup_\omega \bar{\sigma}\{G(j\omega)\} \tag{6.14}$$

This norm can be interpreted for a scalar transfer function G as the distance in the complex plane from the origin to the farthest point on the Nyquist plot of G, in other words, the peak value on the Bode magnitude plot. Similarly, the L_∞ norm has another interpretation

$$\|G\|_\infty^2 = \sup_{u\neq 0} \frac{\int_0^\infty y^T y\, dt}{\int_0^\infty u^T u\, dt}, \quad y = Gu$$

i.e. it is the maximum amplification factor for signals with finite energy.

6.4 Model Reduction

Suppose that $G(s) = \left[\begin{array}{c|c} A & B \\ \hline C & D \end{array}\right]$ is a stable and minimal realization. Let P and Q denote the controllability and observability Gramians (6.4) and (6.5) respectively.

A *balance realization* of $G(s)$ is a realization such that both P and Q are equal and diagonal. This can be achieved through a similarity transformation T that is constructed using the eigenvectors of the product PQ. Moreover, it can be proved that the new Gramians $\hat{P}$ and $\hat{Q}$ have the following structure

$$\hat{P} = \hat{Q} = \begin{bmatrix} \sigma_1 I_{s_1} & & & \\ & \sigma_2 I_{s_2} & & \\ & & \ddots & \\ & & & \sigma_N I_{s_N} \end{bmatrix}$$

where the decreasingly ordered numbers, $\sigma_1 > \sigma_2 > \cdots > \sigma_N > 0$, are called the *Hankel singular values* of the system, and s_i denotes their multiplicity. After the system is balanced the Hankel singular values can characterize the weight of each state in the system. Following this idea, by comparing among the singular values some states could be disregarded without affecting the overall characteristics of the system.

Theorem 6.1 *Suppose that $G(s)$ is a stable and minimum realization of order n. Moreover,*

$$G(s) = \left[\begin{array}{cc|c} A_{11} & A_{12} & B_1 \\ A_{21} & A_{22} & B_2 \\ \hline C_1 & C_2 & D \end{array}\right]$$

is a balanced realization with Gramian $\Sigma = diag(\Sigma_1, \Sigma_2)$

$$\Sigma_1 = diag(\sigma_1 I_{s_1}, \sigma_2 I_{s_2}, \cdots, \sigma_r I_{s_r})$$

$$\Sigma_2 = diag(\sigma_{r+1} I_{s_{r+1}}, \sigma_{r+2} I_{s_{r+2}}, \cdots, \sigma_N I_{s_N})$$

and

$$\sigma_1 > \sigma_2 > \cdots > \sigma_r > \sigma_{r+1} > \sigma_{r+2} > \cdots > \sigma_N$$

where σ_i *has multiplicity* $s_i, i = 1, 2, \cdots, N$ *and* $s_1 + s_2 + \cdots + s_N = n$. *Then the truncated system*

$$G_r(s) = \left[\begin{array}{c|c} A_{11} & B_1 \\ \hline C_1 & D \end{array}\right]$$

is balanced and stable. Furthermore,

$$\|G(s) - G_r(s)\|_\infty \leq 2(\sigma_{r+1} + \sigma_{r+2} + \cdots + \sigma_N)$$

So, according with this theorem a good approximation in the frequency domain can be obtained if some singular values are small enough to be neglected.

6.5 Performance Specifications

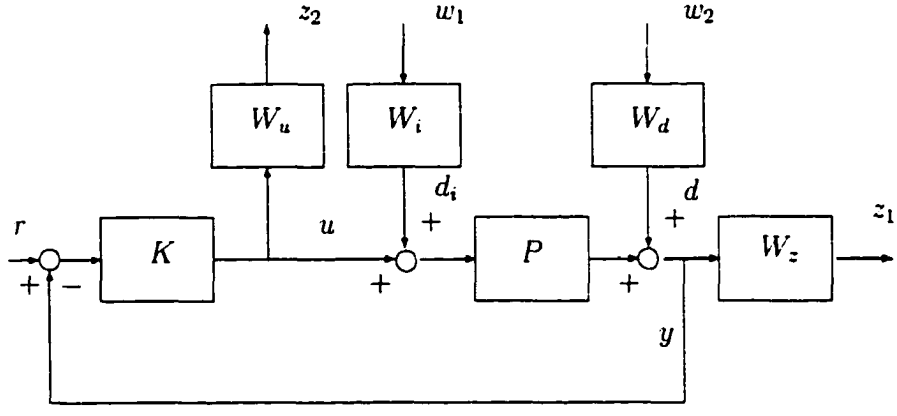

Figure 6.1: Performance Feedback Configuration.

Given any control system, the first step in the control synthesis is to identify the performance requirements that are going to be imposed on the controlled system. Consider for example Figure 6.1, the performance can be translated to minimizing

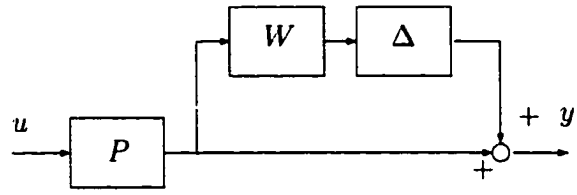

Figure 6.2: Multiplicative Uncertainty Description

the impact of the disturbances w_1 and w_2 on the output, where W_i and W_d are transfer functions that stress the frequency content of the disturbances. In addition, W_u is commonly used to reflect some restrictions on the control or actuator signals, and W_z reflects the requirements on the shape of the closed-loop system. Thus, an optimal controller $K(s)$ minimizes, in some sense, the transfer function from the disturbances $\begin{bmatrix} w_1 \\ w_2 \end{bmatrix}$ to the outputs $\begin{bmatrix} z_1 \\ z_2 \end{bmatrix}$. Now, a 'measure' for this transfer function must be chosen. Usually, the $\|\cdot\|_\infty$ gives a good physical interpretation since it is linked to frequency domain specifications.

Moreover, if our model presents differences or errors due to simplifications or assumptions in the mathematical modeling, an uncertainty description could be chosen to represent this fact. This uncertainty description depends entirely on the designer experience and description of unmodeled dynamics. Commonly, a way to describe the 'size' of the uncertainty Δ is by the $\|\cdot\|_\infty$ norm. The following uncertainty descriptions are usually used

$$\begin{aligned} &\textit{Additive} && P = P_0 + \Delta \\ &\textit{Multiplicative} && P = P_0(I + \Delta) \\ &\textit{Coprime Factor} && P = (N + \Delta_N)(M + \Delta_M)^{-1},\ P_0 = NM^{-1} \end{aligned} \tag{6.15}$$

where P is the true plant, P_0 the nominal plant, Δ modeling errors, and N and M stable transfer functions. Take for example Figure 6.2, this representation is

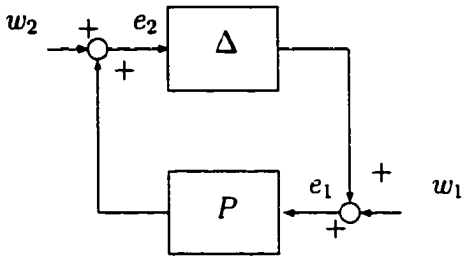

Figure 6.3: Small-Gain Theorem Configuration

chosen in case of actuator errors, neglected high-frequency dynamics and uncertain right-half-plane poles. This kind of uncertainty representation is linked to controller synthesis by the so called 'Small Gain Theorem'.

Theorem 6.2 *Suppose that $P(s)$ is a real rational stable transfer function and let $\gamma > 0$. Then the interconnected system shown in Figure 6.3 is internally stable for all real-rational stable $\Delta(s)$ with*

1. $\|\Delta\|_\infty \leq 1/\gamma$ *if and only if* $\|P\|_\infty < \gamma$
2. $\|\Delta\|_\infty < 1/\gamma$ *if and only if* $\|P\|_\infty \leq \gamma$

Therefore, if $P(s)$, in Figure 6.3, represents the interconnection between plant and controller, a controller designed to maximize uncertainty or perturbation tolerance while keeping stability, *robust stability*, has to minimize $\|P\|_\infty$. If in addition to robust stability, performance specifications are included in the design strategy (i.e. *robust performance* is required), a more involving controller is needed. One of the available design techniques to track this kind of problems is $\mu - synthesis$, which is based on minimizing an upper bound of the robust performance criterion.

6.6 Linear-Fractional-Transformation Framework

In general, robust performance and robust stability criteria can be treated in an unified framework using the Linear-Fractional-Transformation (LFT) description. It can be shown that any interconnected system may be rearranged to fit the general framework in Figure 6.4, where the interconnection system G has the form

$$G(s) = \begin{bmatrix} G_{11}(s) & G_{12}(s) & G_{13}(s) \\ G_{21}(s) & G_{22}(s) & G_{23}(s) \\ G_{31}(s) & G_{32}(s) & G_{33}(s) \end{bmatrix}$$

Thus, the closed-lop system is an LFT on the perturbation and the controller given by

$$\begin{aligned} z &= \mathcal{F}_u(\mathcal{F}_l(G, K), \Delta)\omega \\ &= \mathcal{F}_l(\mathcal{F}_u(G, \Delta), K)\omega \end{aligned}$$

where $\mathcal{F}_u$ and $\mathcal{F}_l$ represent lower and upper LFT. Denote this closed-loop transfer function as $T_{zw} = \mathcal{F}_u(\mathcal{F}_l(G, K), \Delta)$. So from Figure 6.4, $\mathcal{F}_u(P, \Delta)$ is the transformation obtained by closing the upper loop, similarly $\mathcal{F}_l(P, K)$ is the transformation obtained by closing the lower loop.

6.7 $\mathcal{H}_\infty$ Design

Suppose that the LFT interconnection system characterizing the disturbances and control signals be given in Figure 6.4, the goal of the $\mathcal{H}_\infty$ optimal control is to obtain a stabilizing controller $K(s)$ such that

$$\min_K \|T_{zw}\|_\infty$$

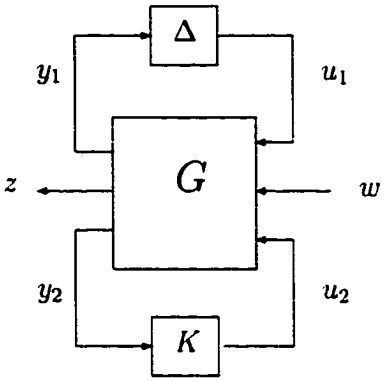

Figure 6.4: General LFT Framework

where T_{zw} represents the closed-loop transfer function from disturbances to weighted output signals. Next, the main steps to design an $\mathcal{H}_\infty$ controller are outlined:

1. Identify control objective: Performance or Robust stability;
2. Select weighting functions;
3. Obtain LFT representation of the system;
4. Compute optimal controller;
5. Apply model reduction to the resulting controller, if it is necessary (Balance Truncation).

Remark 6.1 *The computation of the $\mathcal{H}_\infty$ optimal controllers can be done using MATLAB (μ-Analysis and Synthesis Toolbox [5]). Thus, the computation process can be completely automatized since from the LFT representation the optimal controller can be obtained using just one MATLAB command, hinfsyn. This command (hinfsyn) uses the formulae described in the Doyle et al. [21] paper for the solution to the optimal $\mathcal{H}_\infty$ control design problem, see also [80].*

6.8 $\mathcal{H}_\infty$ Loop Shaping Technique

This design technique incorporates the classical loop-shaping methods to obtain performance/robust stability tradeoffs, and a particular $\mathcal{H}_\infty$ optimization problem to guarantee closed-loop stability and a level of robustness at all frequencies. The design methodology uses only basic concepts of loop-shaping methods, commonly used in classical frequency based designs like lead-lag controllers, and a robust stabilization controller for a *normalized coprime factor* perturbed system is used to construct the final controller.

It is important to mention that this approach in contrast to the classical loop-shaping method is done without explicit regard for the nominal plant phase information. That is, closed-loop stability requirements are disregarded at this stage. Therefore, the design procedure is both simple and systematic and only assumes knowledge of elementary loop-shaping principles on the part of the designer.

The basic assumption of this procedure is that the open-loop plant is a *coprime factor* perturbed plant (6.15), under this assumption the robust stability problem is stated as

$$\min_K \left\| \begin{bmatrix} K \\ I \end{bmatrix} (I + PK)^{-1} \begin{bmatrix} I & P \end{bmatrix} \right\|_\infty \tag{6.16}$$

by the 'Small Gain' theorem. So, define the parameter b_{opt} as the inverse of the minimum $\| \cdot \|_\infty$ after the optimization procedure, i.e.

$$b_{opt} = \left(\left\| \begin{bmatrix} K_\infty \\ I \end{bmatrix} (I + PK_\infty)^{-1} \begin{bmatrix} I & P \end{bmatrix} \right\|_\infty \right)^{-1}$$

Design Procedure (SISO):

1. Loop-shaping: the frequency response of the open-loop plant is shaped using a compensator $W(s)$ to give the desired open-loop shape. The nominal plant $P(s)$ and the shaping compensator W are combined to form the shaped plant P_s, where $P_s = PW$. It is assumed that there is no pole-zero cancellation of unstable modes of P.

2. Synthesize a stabilizing controller $K_\infty(s)$ for P_s, through solving

$$1/b_{opt} = \min_K \left\| \begin{bmatrix} K \\ I \end{bmatrix} (I + P_s K)^{-1} \begin{bmatrix} I & P_s \end{bmatrix} \right\|_\infty \tag{6.17}$$

3. Check the resulting parameter b_{opt}, if $b_{opt} \ll 1$ then return to (1) and adjust W(s).

4. The final feedback controller $K(s)$ is then constructed by combining the $\mathcal{H}_\infty$ controller K_∞ and the shaping compensator W such that

$$K = K_\infty W$$

5. If it is necessary apply model reduction (Balance Truncation) to the resulting controller K.

CHAPTER 7

ACTIVE CONTROL OF A GASEOUS-FUELED COMBUSTOR

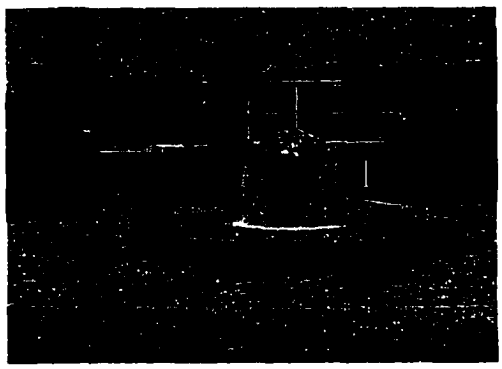

Figure 7.1: Alstom Power Research Center.

The results presented in this chapter are part of a collaboration with the Alstom Power Research Center in Baden, Switzerland. This collaboration started in January of 2000 and successfully ended with a 3 months summer residency from May to August of 2000. During this time, the basic acoustic modeling techniques developed in [30, 59, 68] were used to derive an experimental approximation of the combustor test-rig. Two approaches were developed for active control:

- $\mathcal{H}_\infty$ model-based control and
- Controllers based on Evolution optimization.

Both approaches were capable to attenuate the pressure pulsations in the test-rig by using proportional fuel modulation.

Remark 7.1 *Due to regulations of Alstom Power Ltd. no specific reference to working conditions of the combustor test-rig can be made in the dissertation. Moreover, it is not possible to show explicitly the frequency content of measured signals. Therefore, all the plots showing frequency information were normalized by a constant factor* ω_0.

7.1 Experimental Test-Rig

The experimental set-up, shown in Figure 7.2, is an atmospheric test-rig that consists of a plenum and a circular chambers located upstream and downstream of the burner respectively. The plenum chamber contains perforated plates to reduce the turbulence level of the flow. The circular combustion chamber is composed of an air-cooled double wall quartz glass to provide full visual access to the flame. The exhaust system is an air-cooled tube with the same cross-section as the combustion chamber to avoid acoustic reflections and area discontinuities. The exit of the exhaust has a variable geometry that can be set from (almost) fully reflecting to an acoustic absorption of 60%.

Figure 7.2: Alstom Power Experimental Test Rig.

A swirl stabilized premixed burner is used during the experiments. The flame was stabilized in a recirculation region near the burner outlet. The burner was operated at atmospheric conditions. Controlled excitation of the burner flow was accomplished by four loudspeakers mounted with radial symmetry in the chamber. This type of forcing was applied only during modeling the downstream of the burner. Pressure fluctuations were measured using Brüel & Kjær water-cooled pressure transducers.

In turbines, the space is usually limited; thus acoustic control is not a very practical control strategy due to the large space that loudspeakers require. On the other hand, fuel valves are usually small and they can easily be fitted inside of the turbine. Consequently, fuel modulation control is more appropriate for real applications. Hence, fuel modulation was the strategy chosen for active control. For this purpose, two direct driven solenoid valves, *Moog-DDV* valves, were selected as control actuators. These fuel valves have linear responses according with the voltages applied to their terminals. In the burner, the fuel distribution tubes were divided into two sections, the bottom part was kept constant and the upper part was modulated using the fuel valves. The solenoid valves were configurated such that without control the valves were at their mean aperture. Thus, the control modulation was achieved around a mean fuel flow. This configuration proved to give enough control authority to suppress the combustion instability and did not change the operating condition since the mean value of the modulated control signal was zero. The control strategies were implemented using the dSpace system 'DS1103', which contains a DSP data-acquisition board with analog inputs/outputs. This system contains a direct interface with MATLAB/Simulink that lets the user design control systems using block diagram descriptions.

7.2 Experimental Combustor Model

A brief description of the methodology to obtain the experimental combustor model is presented. This model is based on frequency domain identification and captures the linear dynamics of the combustor for a given operating condition of the chamber. Moreover, it is assumed that the main characteristics (pressure, velocity, density and heat release) of the combustor fluctuate around a mean value. So, the experimental model *represents the dynamics of the fluctuation components in the system.* Generally, the linearity assumption will not hold for the system under consideration, especially at the operating conditions were high amplitude oscillations occur and strong non-linear effects are present. The linearized model is nevertheless useful for controller synthesis, because a controller that stabilizes the linearized model will also stabilize the non-linear model near the linearization point; under the assumption that the model is continuous and continuously differentiable. Moreover, if the controller suppresses the pulsations to sufficiently low levels, the model will be in the linear range.

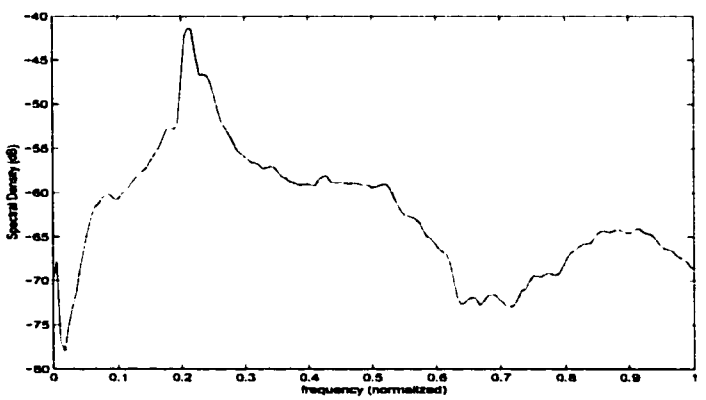

Figure 7.3: Baseline Pressure Measurement.

For the identification process, a baseline working condition (λ, v_b, $\mathcal{P}$, T_a and T_f) of the combustion chamber was chosen such that the thermoacoustic instability was dominant in the pressure field. Thus, for the baseline condition the instability frequency was located at $\omega/\omega_0 \approx 0.205$, where ω_0 represents the normalizing frequency used throughout this chapter. The spectral density plot of the pressure measurement for the baseline condition is shown in Figure 7.3.

7.2.1 Identification Technique

The identification strategy used flow excitation during the combustion process with pure frequency tones. For this purpose, pressure and fuel modulation were applied in sequence. The forcing acoustical signal was driven by water cooled loudspeakers situated downstream of the burner. Meanwhile, the fuel was modulated by two proportional valves that modify the flow pattern into the burner. In Figure 7.4, the experimental combustion test-rig is shown. The voltage signal to the fuel valves (*Moog*) could not be arbitrarily large. In fact, it is limited between -1.8V and $+1.8$V, which corresponds to the case where the valve is completely closed and completely open respectively.

In order to apply the frequency domain identification technique it is assumed that the acoustic field in the downstream of the combustion zone can be described by the 1-D convective wave equation. This enables to express the acoustic field in the combustion chamber by Riemann Invariants (refer to Chapter 5 for a detailed explanation). The Riemann Invariants can be considered as waves (f and g) propagating in opposite axial direction. The acoustic pressure p' is proportional to the sum of both waves while the acoustic velocity u' is given by the difference between

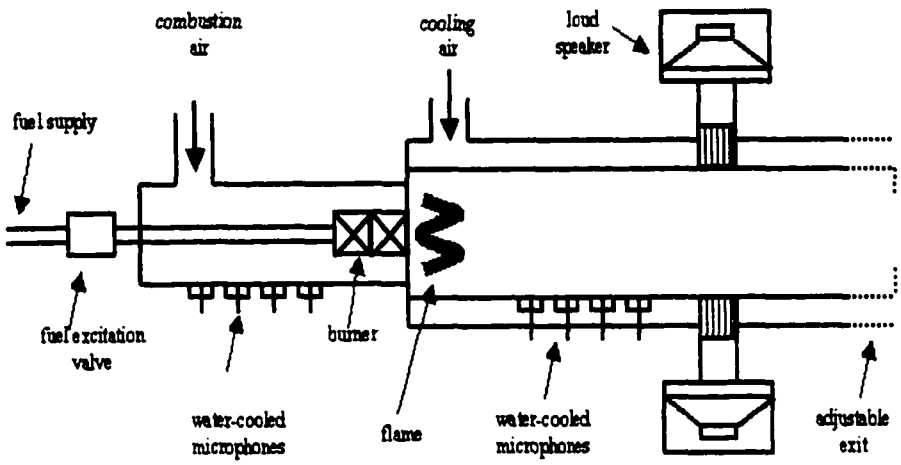

Figure 7.4: Combustor Test Setup.

these two waves:

$$p'(t) = \bar{\rho}\bar{c}(f+g)$$

$$u'(t) = (f-g)$$

where $\bar{\rho}$ and $\bar{c}$ represent mean density and velocity of sound respectively. The entire thermoacoustic system can now be described by applying two boundary conditions and two source terms to the 1-D wave equation.

Boundary conditions:

- Upstream (H_{up}): The upstream boundary condition includes the flame dynamics and reflection coefficient of the burner and plenum.
- Downstream (H_{down}): the boundary reflection dynamics at the chamber exit.

Source Terms:

- Control Actuator (H_{moog}): acoustic properties of the control actuators (fuel *Moog* valves) and their influence on the combustion process.
- Flame (H_{source}): acoustic noise generated by the flame.

The basic idea of this proposed identification process is to identify the above-mentioned boundary conditions and sources. Of particular interest is to capture the dynamics of the control actuators and verify that they provide enough control authority at the instability frequency. Thus, the acoustic waves traveling downstream and upstream of the combustor were extracted from the pressure signal first. Hence, the method called *Multi-Microphone* (an extension to the Two-Microphone) was used [68]. This method uses the pressure signal given by five microphones situated downstream to determine the Riemann Invariants precisely at one reference location. This reference location will be used later as feedback signal during the control process.

7.2.2 Acoustic Blocks Identification

Next, the method to obtain the 4 blocks H_{up}, H_{down}, H_{moog} and H_{source} describing the combustor is outlined.

1. Downstream Model (H_{down}), see Figure 7.5,
   - The variable geometry at the exhaust is set to fully reflecting.
   - The fuel is modulated sequentially with pure tones using the *Moog* valves.
   - At each forcing frequency the pressure Fourier coefficients are calculated for each microphone location.
   - The $\hat{f}$ and $\hat{g}$ waves are computed at each frequency using the *Multi-Microphone* method.

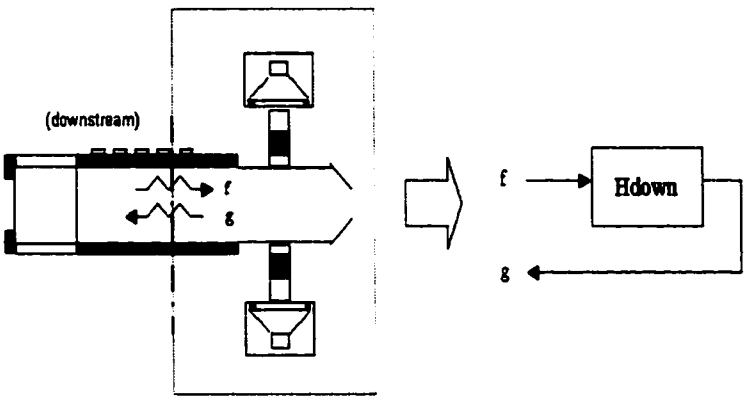

Figure 7.5: Downstream Interaction and Modeling.

- Thus, collecting the data at all the forcing frequencies, the experimental frequency response of the downstream dynamics is constructed by $\hat{H}_{down} = \hat{g}/\hat{f}$.
- Finally, a real rational transfer function $H_{down}(s)$ is fitted to $\hat{H}_{down}$.

2. Upstream Model (H_{up}), see Figure 7.6,

   - The variable geometry at the exhaust is now set to maximum absorption. This is to ensure low acoustic pressure levels and thus linear behavior of the system.
   - Now, the pressure field is modulated upstream with pure tones by downstream loudspeakers.
   - At each forcing frequency the pressure Fourier coefficients are calculated for each microphone location.
   - The $\hat{f}$ and $\hat{g}$ waves are computed at each frequency using the *Multi-Microphone* method.

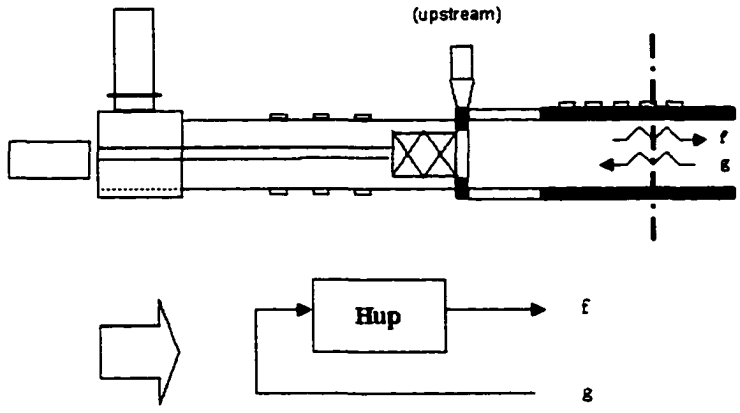

Figure 7.6: Upstream Modeling.

- Again, collecting the data at all forcing frequencies, the experimental frequency response of the upstream block is obtained from $\hat{H}_{up} = \hat{f}/\hat{g}$.
- A real rational transfer function $H_{up}(s)$ is fitted to $\hat{H}_{up}$.

3. Control Actuator (H_{moog}), see Figure 7.7,

   - The variable geometry is set to maximum absorption.
   - Using the data acquired during the fuel modulation stage, the corresponding Riemann Invariants $\hat{f}$ and $\hat{g}$ are extracted.
   - The output response of the control actuator is computed by $\hat{n}_{moog} = \hat{f} - \hat{H}_{up}\hat{g}$ at each forcing frequency.
   - Given the input forcing signal $\hat{u}$, the frequency response of the control actuator is constructed by $\hat{H}_{moog} = \hat{n}_{moog}/\hat{u}$.
   - A real rational transfer function $H_{moog}(s)$ is fitted to $\hat{H}_{moog}$.

4. Flame Model (H_{flame}), see Figure 7.8,

   - The variable geometry is set to maximum absorption.

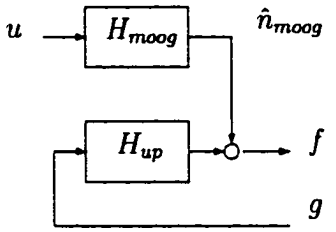

Figure 7.7: Upstream Control Actuator Interaction.

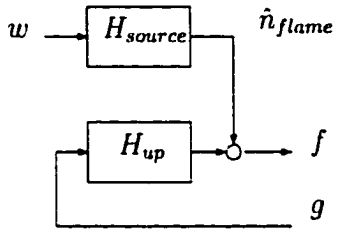

Figure 7.8: Upstream Flame Interaction.

- Take the pressure measurement without forcing.
- Transform the microphone signals from time domain to frequency domain (Fourier Transform).
- Calculate $\hat{f}$ and $\hat{g}$ from microphone data using the Multi Microphone Method.
- Calculate the flame acoustic characteristics by $\hat{n}_{flame} = \hat{f} - \hat{H}_{up}\hat{g}$.
- Since this block is modeled as a sound source, it is assumed that its input w is white noise. So, finally fit a real rational transfer function $H_{source}(s)$ to the frequency data $\hat{H}_{source} = \hat{n}_{flame}/\hat{w}$.

Note that the upstream interaction is quite complex since it consists of 3 blocks as shown in Figure 7.9. Thus, it is necessary to follow the procedure in the correct sequence to obtain the correct overall model. Moreover, it is intended to control the

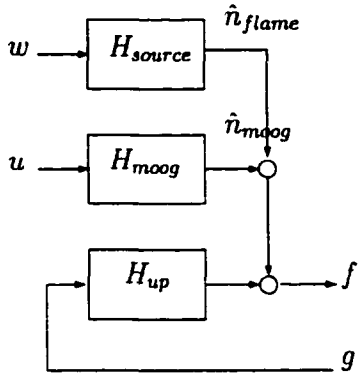

Figure 7.9: Upstream Interactions.

combustor using fuel flow modulation, so of particular interest is to obtain the right description for the solenoid fuel valves.

The extraction of the Riemann-Invariants from the pressure measurements was completely automatized in the test-rig. For this purpose, a master program coded in LabView first generated all the signals needed in the initial part of identification strategy, and then processed the measurements to obtain the frequency characteristics of the Riemann-Invariants using the Multi-Microphone Method [68]. The rest of the processing was carried out in MATLAB. The *signal processing* and *μ-synthesis toolboxes* were used [5]. The final transfer function fittings were computed by using the commands *fitsys* and *invfreqs* which use a least-square approximation.

Finally, using the relation between the Riemann Invariant waves f and g and the pressure fluctuations at some fixed axial point

$$p'(t) = \bar{\rho}\bar{c}(f+g)$$

the final model describing the complete combustor process from the input control voltage to the microphone measurements is given in Figure 7.10. Clearly from the model, the objective of the controller is to attenuate the effects of the disturbance, flame acoustic dynamics, on the system.

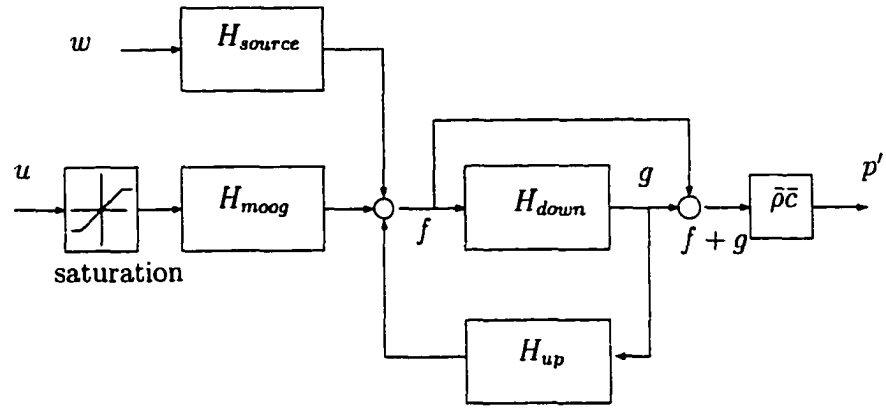

Figure 7.10: Combustor Experimental Model.

7.3 Open-Loop Experimental Model Analysis

Now, the experimental model obtained through the identification process is reviewed. Each block of the model is analyzed independently, as well as the overall open-loop system. Hence, a clear picture of the instability mechanism could be drawn.

7.3.1 Downstream Interaction

The downstream dynamics of the combustion chamber are modeled by H_{down}. It mainly represents the acoustic reflection characteristics of the Riemann Invariants due to the boundary conditions in the chamber. The identified block H_{down} is a 6^{th} order stable and non-minimum phase transfer function. The frequency response of H_{down} is shown in Figure 7.11. The frequency gain is almost constant for $\omega/\omega_0 < 0.205$, but beyond that frequency it is decaying continuously. Hence, the f wave is almost perfectly reflected in the interval $0 < \omega/\omega_0 < 0.205$.

$$H_{down}(\hat{s}) = \frac{-0.1644(\hat{s}-1.447)(\hat{s}-0.2944)(\hat{s}^2+0.03392\hat{s}+0.04509)}{(\hat{s}^2+0.4571\hat{s}+0.08457)(\hat{s}^2+0.03556\hat{s}+0.04449)}$$

$$\cdot\frac{(\hat{s}^2 - 0.4368\hat{s} + 0.5549)}{(\hat{s}^2 + 0.4022\hat{s} + 0.5423)}$$

where $\hat{s} = s/\omega_0$.

7.3.2 Upstream Interaction

The block H_{up} represents the dynamics of the combustion chamber upstream of the reference position. It contains the acoustic burner dynamics due to the reflection of the Riemann Invariants, wave propagation and interaction with the combustion process. H_{up} is an 8^{th} order transfer function with stable and non-minimum phase characteristics. In Figure 7.12, the frequency response is plotted. From this plot, the response is almost flat for $\omega/\omega_0 < 0.20$. Hence, the g wave is reflected constantly into f with certain attenuation factor in the range $0 < \omega/\omega_0 < 0.20$. Above that frequency range, there are three peaks in descending magnitude at $\omega/\omega_0 \approx 0.21$, 0.24 and 0.80. Moreover, in the frequency range $0.20 < \omega/\omega_0 < 0.25$ there is an amplification factor. Note that the frequency response is decaying slowly in the high frequency range ($\omega/\omega_0 > 1.2$).

$$H_{up}(\hat{s}) = \frac{-0.36259(\hat{s} - 0.3602)(\hat{s} + 0.4925)(\hat{s}^2 + 0.04713\hat{s} + 0.03387)}{(\hat{s}^2 + 0.02812\hat{s} + 0.04346)(\hat{s}^2 + 0.4069\hat{s} + 0.08826)}$$

$$\cdot\frac{(\hat{s}^2 + 0.03674\hat{s} + 0.05057)(\hat{s}^2 - 0.6811\hat{s} + 0.5111)}{(\hat{s}^2 + 0.3566\hat{s} + 0.6485)(\hat{s}^2 + 0.04443\hat{s} + 0.05441)}$$

7.3.3 Control Actuator

The control actuator modulates the fuel flow into the burner affecting the heat release fluctuations and consequently modifying the pressure field. Thus, the block H_{moog} represents the mapping from the fuel valves input voltage to the pressure measurement. H_{moog} is an 8^{th} order stable and non-minimum phase system. The frequency response of this block is shown in Figure 7.13. From this plot it is evident

that the control actuator has a limited working range, roughly from $0 < \omega/\omega_0 < 0.35$. However, the instability frequency is located roughly at $\omega/\omega_0 \approx 0.205$. Therefore, it is clear that the control actuator can provide enough control authority at this frequency to suppress the instability. Note that in this working range, there are three resonant peaks $\omega/\omega_0 \approx 0.1$, 0.17 and 0.21.

$$H_{moog}(\hat{s}) = \frac{-0.0023903(\hat{s}-5.331)(\hat{s}-0.1571)(\hat{s}^2+0.05491\hat{s}+0.01558)}{(\hat{s}^2+0.0424\hat{s}+0.007558)(\hat{s}^2+0.03568\hat{s}+0.02032)}$$
$$\cdot\frac{(\hat{s}^2-0.1364\hat{s}+0.0419)(\hat{s}^2-0.211\hat{s}+0.181)}{(\hat{s}^2+0.07795\hat{s}+0.09263)(\hat{s}^2+0.05564\hat{s}+0.04459)}$$

7.3.4 Flame Source

Finally, the property of the flame to act as a source of sound is modeled by the block H_{source}. Furthermore, it contains all the acoustic interactions of the turbulent flow due to the swirl stabilization process. H_{source} is a 10^{th} order stable and minimum phase transfer function. From the frequency response in Figure 7.14, the flame response has two resonant peaks, one at approximately $\omega/\omega_0 \approx 0.22$ and the largest at $\omega/\omega_0 \approx 0.24$.

$$H_{source}(\hat{s}) = \frac{0.028279(\hat{s}+0.09691)(\hat{s}^2+0.2692\hat{s}+0.04425)}{(\hat{s}+2)(\hat{s}+0.13)(\hat{s}^2+0.05696\hat{s}+0.0338)}$$
$$\cdot\frac{(\hat{s}^2+0.04824\hat{s}+0.04123)(\hat{s}^2+0.01565\hat{s}+0.04817)(\hat{s}^2+0.689\hat{s}+0.5027)}{(\hat{s}^2+0.01065\hat{s}+0.04658)(\hat{s}^2+0.02946\hat{s}+0.05775)(\hat{s}^2+0.309\hat{s}+0.2062}$$

7.3.5 Open Loop Model

Now, the open-loop transfer functions will be analyzed. From the experimental model description, see Figure 7.10, the combustor system could be considered with two inputs: the disturbance w coming from the flame dynamics and the control actuator signal u, and one output measurement p': the pressure transducer. So,

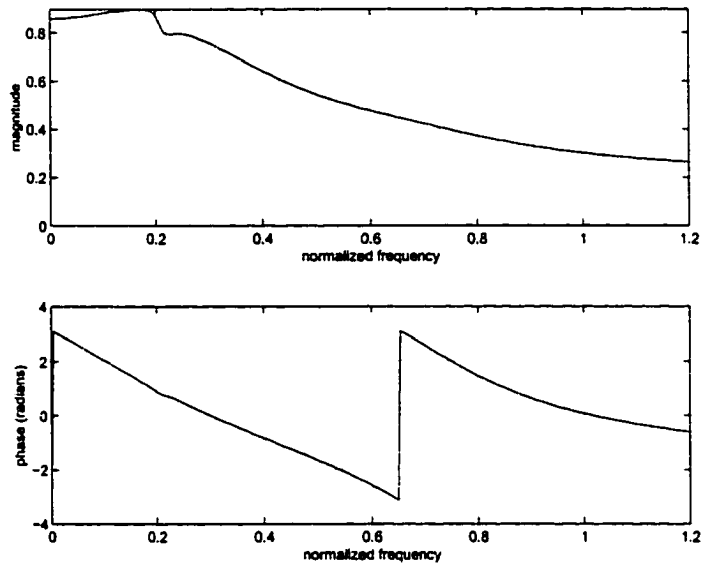

Figure 7.11: Downstream Block Frequency Response.

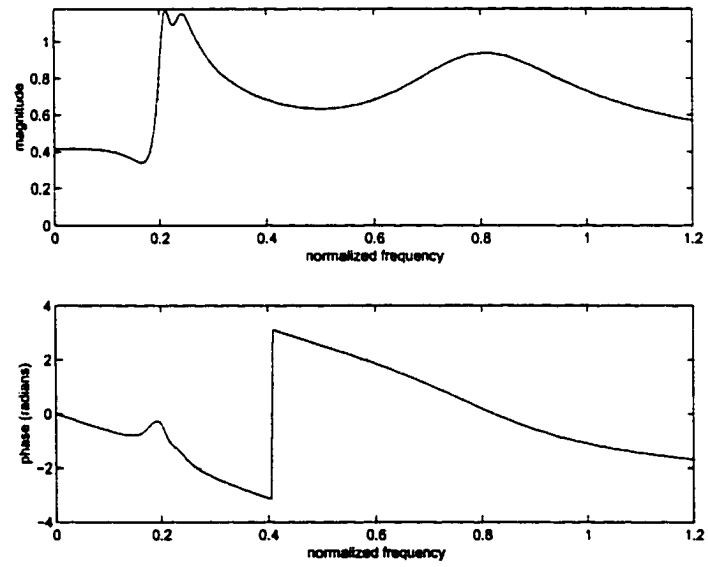

Figure 7.12: Upstream Block Frequency Response.

two open-loop models could be identified P_1 (disturbance w to pressure p') and P_2 (control signal u to pressure p'):

$$P_1 = \frac{1 + H_{down}}{1 - H_{up}H_{down}} \cdot H_{source} \tag{7.1}$$

and

$$P_2 = \frac{1 + H_{down}}{1 - H_{up}H_{down}} \cdot H_{moog} \tag{7.2}$$

After substituting the realizations for H_{down}, H_{up}, H_{moog} and H_{flame} into equations (7.1) and (7.2) the transfer functions for P_1 and P_2 were obtained. P_1 is a stable and minimum-phase system, meanwhile, P_2 is a stable but non-minimum phase system. They both have a lightly damped complex pair of poles close to the imaginary axis, which *represent the instability dynamics.* Now, the frequency responses for both systems P_1 and P_2 are shown in Figures 7.15 and 7.16 respectively. From the frequency response, it is clear the peak due to the thermoacoustic instability, related to the lightly damped complex poles, located at $\omega/\omega_0 \approx 0.205$. Thus, the objective of the control strategy is to give enough damping to suppress this peak. In addition, P_1 has a small bump in the frequency response at $\omega/\omega_0 \approx 0.24$ due to the flame response. Similarly, P_2 has also a small bump but at $\omega/\omega_0 \approx 0.15$ due to the actuator dynamics. Note also that the frequency response of P_2, shown in Figure 7.16, has a large roll-off in phase mainly due to time-delays associated with the actuation of the control fuel and the combustion process.

Finally, since the flame also acts as a source of sound, this represents a continuous excitation to the system, as shown in Figure 7.10. The experimental model with this self-excitation was simulated with no control signal $u = 0$, see Figure 7.17. It is important to mention that the pressure trace obtained from simulation resembles the pressure measurements obtained in the test-rig without forcing, see Figure 7.3.

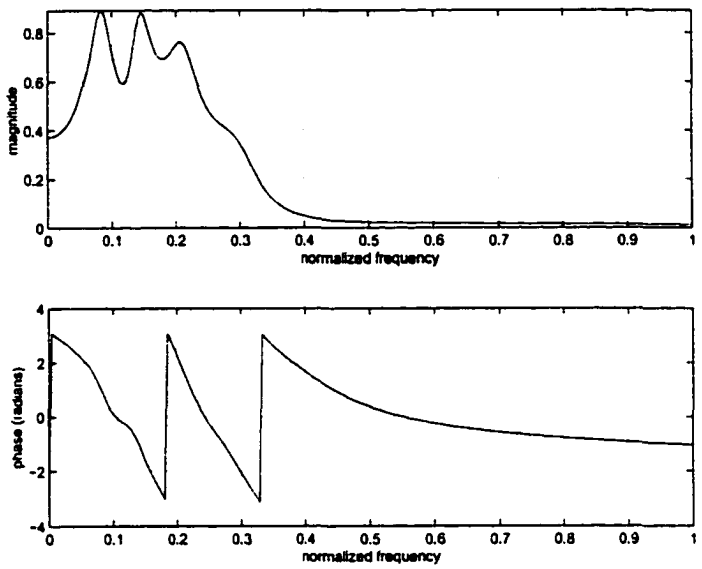

Figure 7.13: Control Actuator Block Frequency Response.

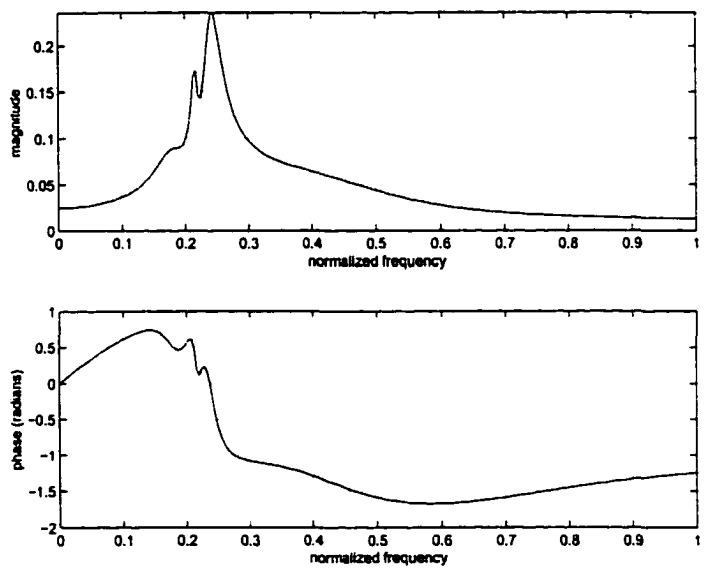

Figure 7.14: Flame Block Frequency Response.

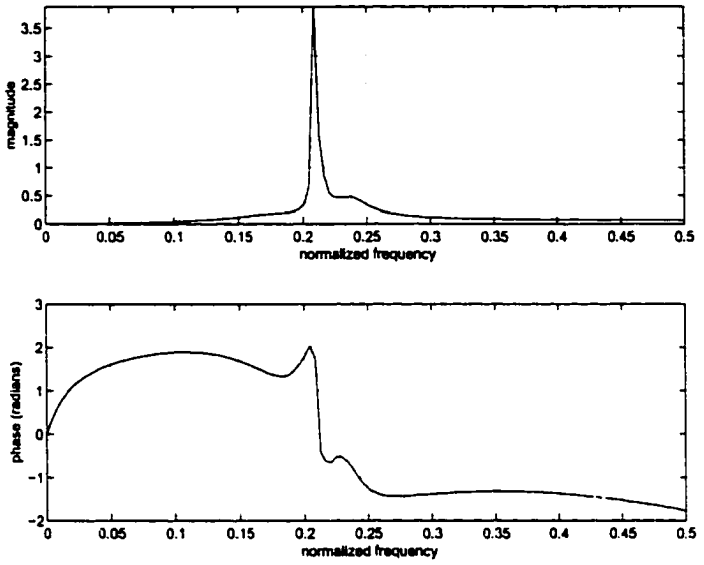

Figure 7.15: Open-Loop Block P_1 (disturbance-to-pressure) Frequency Response.

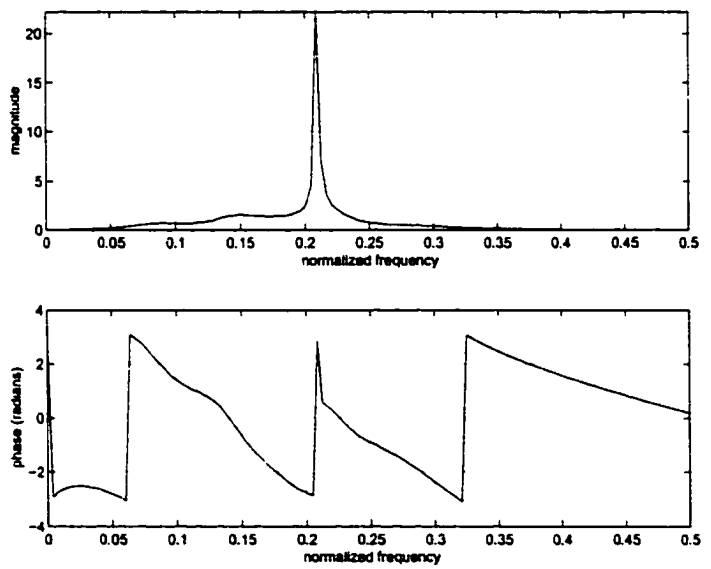

Figure 7.16: Open-Loop Block P_2 (control signal-to-pressure) Frequency Response.

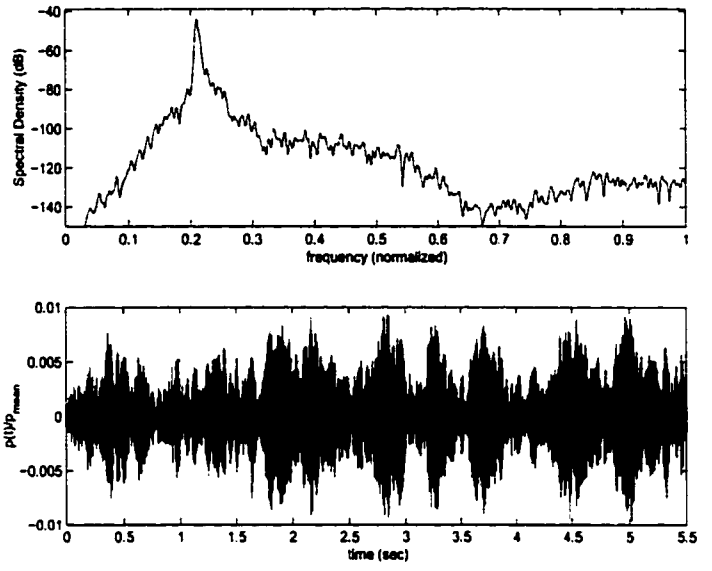

Figure 7.17: Simulation of Experimental Open-Loop Model (disturbance-to-pressure).

However, some mismatching could be due to nonlinear dynamics presented in the combustor which are disregarded in the proposed model.

7.4 Controller Synthesis

$\mathcal{H}_\infty$ design was chosen as control strategy since this technique has a desired frequency domain interpretation by minimizing the peak amplitude in the frequency response. Two control techniques were investigated: $\mathcal{H}_\infty$ Disturbance Rejection design and $\mathcal{H}_\infty$ Loop-Shaping technique [80]. First, a controller achieving the maximum attenuation in the frequency response peak was sought, so $\mathcal{H}_\infty$ Disturbance Rejection design was used. On the other hand, a controller that could achieve good performance and also maintain some robustness properties was investigated, thus $\mathcal{H}_\infty$ Loop-Shaping technique was applied.

In order to avoid numerical problems during the computation of the $\mathcal{H}_\infty$ controllers, the scale factor $\bar{\rho}\bar{c}$, see Figure 7.10, was removed from the experimental model during the control design. Therefore, the final controllers were rescaled by this factor.

7.4.1 $\mathcal{H}_\infty$ Disturbance Rejection Design

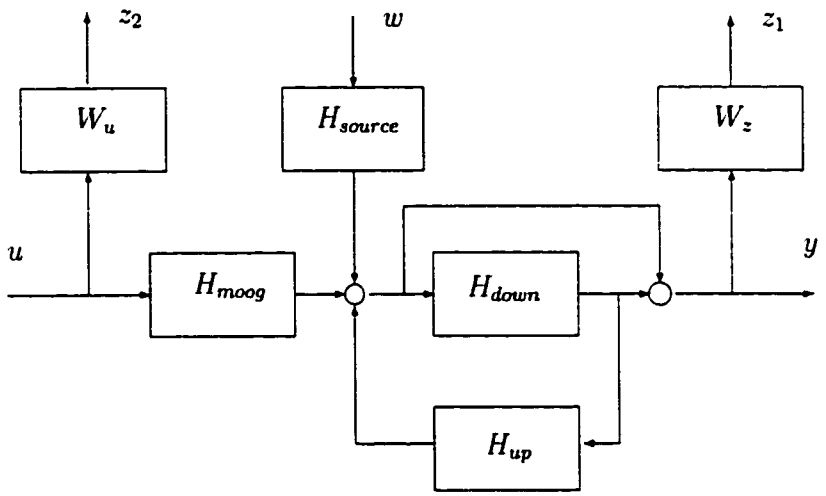

Figure 7.18: Setup for $\mathcal{H}_\infty$ Optimization.

From the model description in Figure 7.10, the objective of the controller is to minimize the effect of the noise coming from the flame into the combustor chamber, a *disturbance rejection problem.* In addition, there is also a requirement in the control signal since a saturation is limiting the actuator effect. Therefore, it is important to reduce the magnitude of the main harmonic peak, but keeping the control signal inside the saturation limits. In summary, all this requirements can be translated by solving a weighted $\mathcal{H}_\infty$ problem as shown in Figure 7.18 where the objective is to design a controller $u = Ky$ so that the $\mathcal{H}_\infty$ norm from w to $\begin{bmatrix} z_1 \\ z_2 \end{bmatrix}$ is minimized. W_z and W_u represent the pressure output and control signal weighting functions

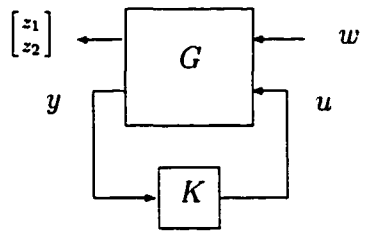

Figure 7.19: Generalized LFT Structure.

respectively:

$$W_z(\hat{s}) = \frac{0.082816(\hat{s}+4.4)^2(\hat{s}+0.01)^2}{(\hat{s}+0.32)^2(\hat{s}+0.16)^2}$$
$$W_u(\hat{s}) = \frac{25(\hat{s}+1.6)}{(\hat{s}+6)}$$

Their frequency responses are shown in Figure 7.20.

It is easy to see that the system shown in Figure 7.18 can be written in a general LFT form as in Figure 7.19. Thus, the generalized plant G for the LFT interconnection can be calculated from Figure 7.18

$$G = \left[\begin{array}{c|c} W_z T H_{source} & W_z T H_{moog} \\ 0 & W_u \\ \hline TH_{source} & TH_{moog} \end{array}\right] \tag{7.3}$$

where

$$T = \frac{1 + H_{down}}{1 - H_{down} H_{up}} \tag{7.4}$$

So, the control objective can be stated as

$$\gamma_{opt} = \min_{K \text{ stabilizing}} \|T_{zw}\|_\infty$$

where T_{zw} denotes the transfer matrix from w to z. Note that the space of search for the optimal $\mathcal{H}_\infty$ controller is the space of controllers that stabilize the closed-loop

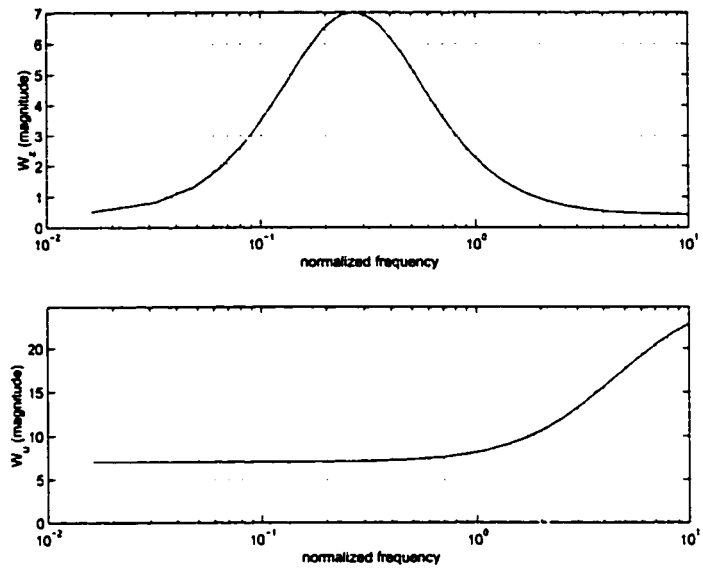

Figure 7.20: Weighting Functions of $\mathcal{H}_\infty$ Optimization: W_z (Top) and W_u (Bottom).

interconnection. There is no particular restriction on the stability of the controller itself. So, during the $\mathcal{H}_\infty$ control synthesis, it was found that the resulting controller was unstable. Obviously, this kind of controllers are not suitable in our application, due mainly to the high sensitivity and lack of robustness. Moreover, there is a saturation restriction on the control signal, so the tendency for the closed-loop system to go unstable is pretty high. This last statement was corroborated during simulation. Therefore a way to avoid this problem was investigated.

During the bisection algorithm used for the $\mathcal{H}_\infty$ optimization, it was noticed that after each iteration the pole with the largest real part of the resulting controller was moving continuously to the right-half-plane. Therefore, there was a limiting bound $\gamma_{stable} > \gamma_{opt} > 0$ such that the closed-loop $\mathcal{H}_\infty$ norm was less than γ_{stable} and the corresponding controller K was still stable. So, there was a limitation in the performance that could be achieved if a stable controller was required. In addition,

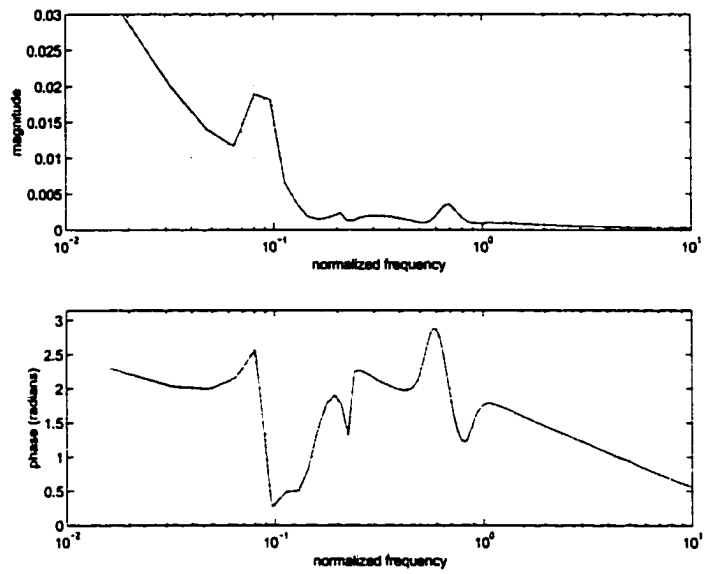

Figure 7.21: Frequency Response of $\mathcal{H}_\infty$ Disturbance Rejection Controller.

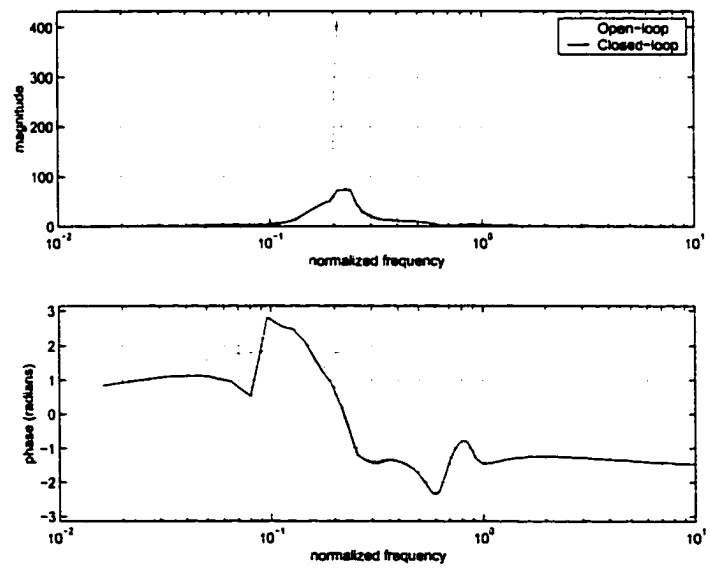

Figure 7.22: Frequency Responses for Open and Closed Loop with $\mathcal{H}_\infty$ Disturbance Rejection Controller.

it was also noticed that this limiting value $\gamma_{stable} > 0$ could be changed according with the weighting functions W_z and W_u. After the computation of the final $\mathcal{H}_\infty$ controller, balance truncation method was applied to disregard states without significant weight in the frequency response. The frequency response of the resulting $\mathcal{H}_\infty$ Disturbance Rejection controller is presented in Figure 7.21. In addition, the closed-loop and open-loop bode plots are shown in Figure 7.22. It is clear that the control feedback loop is able to reduce the peak in the pressure frequency response effectively. Note that this kind of controller does not have any robustness properties inherited from the controller synthesis.

7.4.2 $\mathcal{H}_\infty$ Loop Shaping Technique

The $\mathcal{H}_\infty$ Loop Shaping technique cannot handle direct constraints and disturbance descriptions as in the previous formulation. Therefore, the model of the noise coming from the flame H_{source} was not actually used in the designing stage and the control signal restriction had to be checked experimentally after the design was complete. From the experimental combustor representation (7.10), the equivalent open-loop plant is given by

$$P = H_{moog}\frac{1 + H_{down}}{1 - H_{up}H_{down}}$$

Now, the idea is to shape the open-loop in a certain way such that the objectives can be satisfied. In a general setting, in order to have a good frequency peak attenuation the controller must have enough control authority at that frequency. On the other hand, there is a hard limitation coming from the control saturation. So, the frequency gain at the main harmonic has to be limited to certain value. In addition to this, the actuator has a limited working frequency range. All these

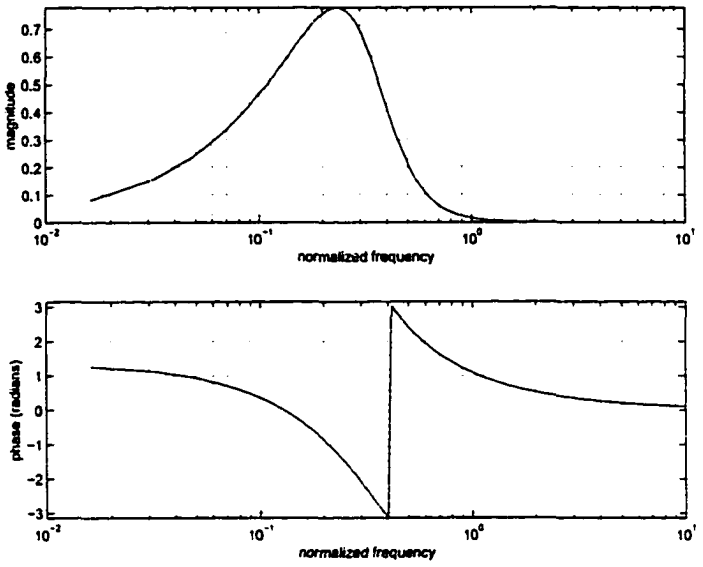

Figure 7.23: Loop-Shaping Compensator W.

specifications were translated into the weighting function

$$W(\hat{s}) = \frac{0.015088(\hat{s} + 0.0018)}{(\hat{s} + 0.16)(\hat{s}^2 + 0.384\hat{s} + 0.1024)(\hat{s}^2 + 0.48\hat{s} + 0.16)}$$

Its frequency response is shown in Figure 7.23. The corresponding optimal controller was obtained. Next, balance truncation was used to reduce the order of the resulting controller. The frequency response of the final $\mathcal{H}_\infty$ Loop-Shaping controller is shown in Figure 7.24. In Figure 7.25, a comparison between the closed and open loop frequency responses is presented.

The computation of the $\mathcal{H}_\infty$ controllers was carried out in MATLAB by using the *μ-synthesis* and *control* toolboxes [5, 28]. Hence, the commands *hinfsyn* and *ncfsyn* were applied to synthesize the $\mathcal{H}_\infty$ Disturbance Rejection and $\mathcal{H}_\infty$ Loop-Shaping controllers respectively. On the other hand, the commands *balreal* and *modred* were used to perform the balance truncation approximations.

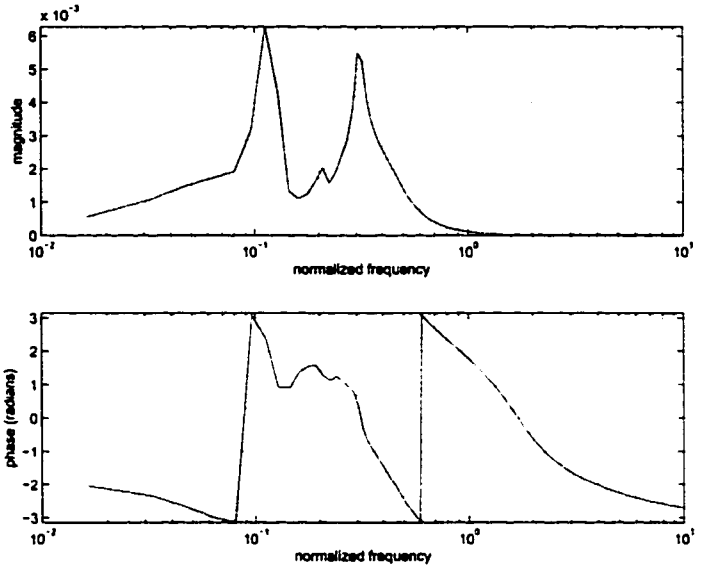

Figure 7.24: Frequency Response for $\mathcal{H}_\infty$ Loop-Shaping Optimal Controller.

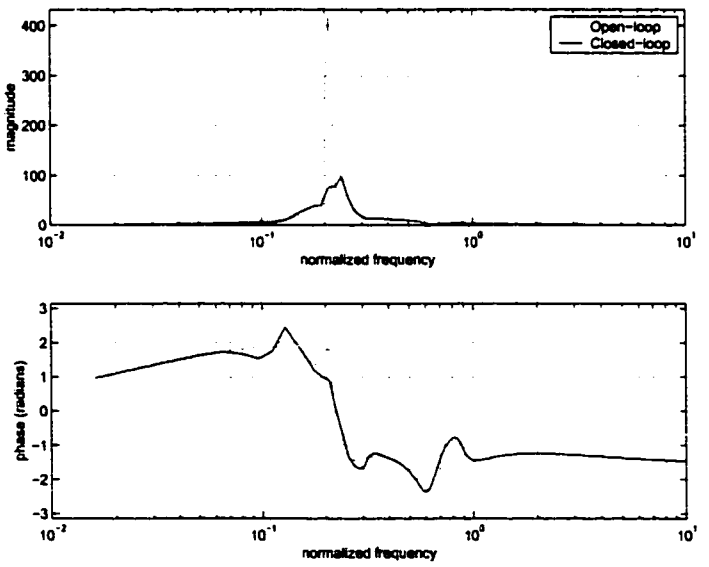

Figure 7.25: Frequency Responses for Open and Closed Loop with $\mathcal{H}_\infty$ Loop-Shaping Controller.

7.5 Optimization Using Evolution Algorithm

7.5.1 Motivation

The combustor chamber is a very complex system and presents changes in its dynamics according with the working conditions. For an unstable point, the dynamics inside of the chamber are highly nonlinear [73] and extremely difficult to describe accurately. However, for low amplitudes (stable conditions) the system is approximately linear [30]. Nevertheless, for a specific working condition a linear approximation can be very useful. Hence, a controller like $\mathcal{H}_\infty$ could be computed for this particular condition.

In a real combustor the operating conditions are varied continuously, thus it is necessary to obtain a whole set of models to derive the corresponding controllers. This procedure although effective, requires much engineering work. Thus, it is appealing to have a controller that could adapt to any given working condition. This motivates the idea of having a controller whose parameters could be adjusted on-line through an optimization process of some defined performance index. Consequently, the main advantage is that no-knowledge from the combustor is needed a priori. On the other hand, one restriction is the complexity of the proposed controller, since the number of control parameters will dictate the speed of the optimization process. Therefore, a controller with a few parameters, like first or second order compensator, is always preferred.

From previous published work [9, 31, 41], it is known that the basic controller that can stabilize the pressure pulsations inside the combustor is a simple phase-delay controller. Even though the performance achieved is not the best, a reasonable attenuation factor can be obtained. So, this simple phase-delay controller was taken

as a starting point. Thus, the control had only two parameters to adjust: k_0 (gain) and τ (delay)

$$K = k_0 \cdot e^{-s\tau}$$

Now, a performance index must be chosen that reflects the pressure changes over some given time. Thus, a measure of power was selected

$$Cost\ Function = \frac{1}{T}\int_{t_i}^{t_i+T} p'(t)^2 dt \tag{7.5}$$

where $p'(\cdot)$ is the pressure fluctuation measurement, t_i is the starting time of evaluation and T is the evaluation period. Lab tests showed that the variance of the cost function decays exponentially with T. However, some operating conditions needed longer evaluation times to obtain an acceptable level of the variance of the cost function. A compromise between reasonable evaluation time and acceptable variance was found for values of T between 5 to 7 seconds. This observation brought to us two important points:

1. The performance index is corrupted by turbulence noise, and
2. The convergence speed of the optimization algorithm is limited by the long evaluation process.

From the results obtained from simulation, the optimization process presents a convex shape but with a repetitive pattern as shown in Figure 7.26. Moreover, this result was verified through testings in the combustor test-rig. Therefore, the existence of a minimum for the pair of parameters was ensured. Now, it remains to choose an appropriate optimization technique, several strategies were explored at this stage. In order to benchmark the different strategies, the thermoacoustic model of the combustor shown in (7.10) was used. The *steepest descent* and *Lagrangian interpolation* [67] were tested in simulation with moderate results, for some iterations

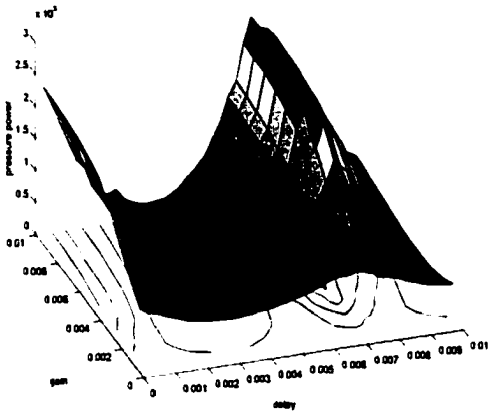

Figure 7.26: Gain-Delay Performance Index Surface.

the algorithms never converged to the optimum value. Nevertheless, an experimental test was performed and it corroborated the previous results, the convergence ratio was poor. A good explanation for this failure resides in the former observation made about the performance index, for the same pair (k_0, τ) evaluated at two different instants the performance index might change roughly 10% or more. This property of the system makes it difficult to establish a decreasing pattern for the parameters that leads to lack of convergence.

In order to solve this problem a change of perspective was needed since any of the well-known optimization techniques could not deal with noisy signals. Thus, the focus changed to a less mathematical optimization but more intuitive idea. In this way, evolution strategies came as a perfect choice due to their strong adaptation capabilities, see [67].

7.5.2 Evolution Algorithm

So far, *Evolution* has been responsible for developing optimal or at least very good structures in nature. In *evolution*, the mechanism of variation is the occurrence

of random exchanges, even "errors", in the transfer of genetic information from one generation to the next. *Evolution* as an optimization strategy has intrigued researchers since the 50's and 60's. Early work in this field is due to Box [10], Pask [60] and Schumer [69]. However, one of the main contributions came later by Rechenberg. In his book [63], he examined the analogy between natural evolution and technical optimization and presented a scheme for multimembered evolution.

Consider a function that has to be optimized with m inputs and one output. The output of this function is referred as its *fitness*. The idea is now to adjust the input parameters in order to find an optimum in the *fitness*. One combination of m input parameters is called an *individual*. A group of n individuals is a *population*. The idea is to start with a randomly selected initial population (*mutation*), creating a group of *children* out of their parents. The fitness of the children is now evaluated and compared with their parent's fitness, and the best of both are selected to be the next generation of parents. This procedure will go on until an optimum is found, or a given termination criterion is fulfilled.

Following these ideas, the following evolution algorithm was adopted in the optimization process

1. Initialize parameters of the evolution algorithm.
2. Select initial population (this can be a random selection, a guess or a results of a previous experiment).
3. Check if the conditions for termination of algorithm are satisfied: optimality, max. # of iterations or no-progress
    - **YES** : Set the best values obtained during the optimization process.
    - **NO** : Continue with Evolution Alg.

4. Adjust step (mutation range) according with progress achieved.

5. Create children from parents set.

   (a) Check mutation factor.

   (b) Determine new step.

   (c) Generate children by adding a random perturbation of variance 'step' to parents.

   (d) Check that children satisfy the parameters bounds.

6. Evaluate children fitness.

7. Compares children and parents performance, keep the best of both.

8. Compute progress velocity according with # of children better than parents.

9. Select the best solutions to judge optimality.

10. Go back to 3.

In order to judge the capabilities of this algorithm to deal with cost functions corrupted by noise, a test was carried out using a well-defined convex function with a global minimum, see Figure 7.27. An initial set of values was given by $\diamond$ and after 200 iterations the best solutions were plotted $*$. This example shows how the evolution strategy is capable of dealing effectively with noise during the optimization.

7.5.3 Controller Structure

Motivated by the idea that a simple lead filter plus a delay term could add enough damping to suppress the pressure pulsations, a rather simple controller was tested:

$$K(s) = k_0 \frac{s/a + 1}{s/b + 1} e^{-s\tau} \cdot \frac{1}{s/\omega_c + 1} \tag{7.6}$$

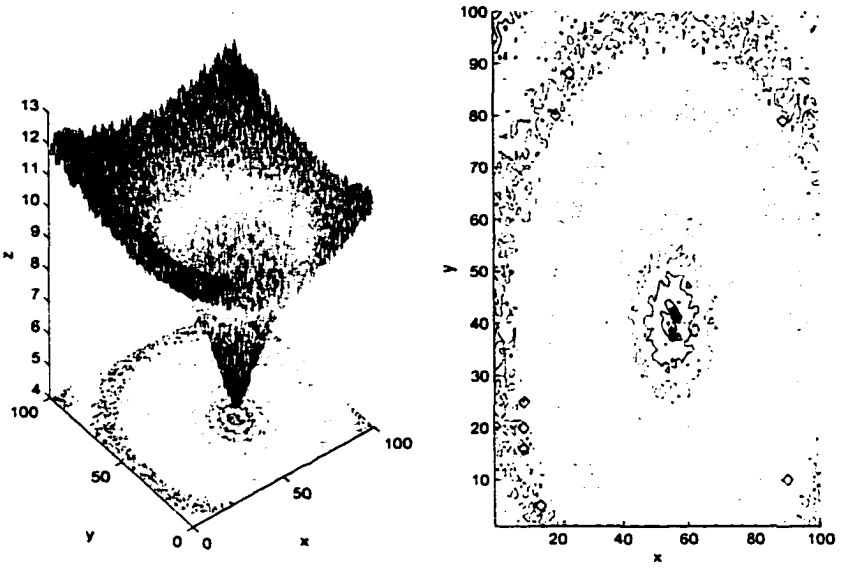

Figure 7.27: Evolution Algorithm Optimization with Noisy Cost Function.

where the parameters a and b were chosen to give a fixed damping factor at the instability frequency, k_0 and τ were tuned manually online and ω_c was chosen to filter high frequency noise, $\omega_c \approx 500$ Hz. Surprisingly, this simple idea gave very good results achieving a good suppression in the pressure pulsations of the test-rig.

On the other hand, this controller structure has only 4 parameters, so this makes it a good candidate for an online optimization since the complexity of the controller is limited. Moreover, if a closed interval of variation could be derived for each parameter the space of search would be largely reduced. Nevertheless, the final controller prototype has an extra zero and pole in order to have two more degrees of freedom

$$K(s) = k_0 \frac{s/a_1 + 1}{s/b_1 + 1} \frac{s/a_2 + 1}{s/b_2 + 1} e^{-s\tau} \cdot \frac{1}{s/\omega_c + 1} \tag{7.7}$$

where corresponding bounds were set to each parameter.

7.5.4 Optimization of Controller Parameters by Evolution

The evolution algorithm outlined earlier was used to tune the parameters of (7.7) online. A master-program was coded as an m-files in MATLAB and it was in charge of running the evolution strategy and to establish the communication directly with a DSP board which is in charge of running the controller online. Thus, the controller parameters were updated from MATLAB by direct access to the DSP.

On the other hand, to have some flexibility in the controllers, several controller structures were implemented on the DSP board

$$\begin{aligned}
K(s) &= k_0\, e^{-s\tau} \cdot \tfrac{1}{s/\omega_c+1} \\
K(s) &= k_0\, \tfrac{s/a_1+1}{s/b_1+1} \cdot \tfrac{1}{s/\omega_c+1} \\
K(s) &= k_0\, \tfrac{s/a_1+1}{s/b_1+1} \cdot e^{-s\tau} \cdot \tfrac{1}{s/\omega_c+1} \\
K(s) &= k_0\, \tfrac{s/a_1+1}{s/b_1+1}\, \tfrac{s/a_2+1}{s/b_2+1} \cdot \tfrac{1}{s/\omega_c+1} \\
K(s) &= k_0\, \tfrac{s/a_1+1}{s/b_1+1}\, \tfrac{s/a_2+1}{s/b_2+1} \cdot e^{-s\tau} \cdot \tfrac{1}{s/\omega_c+1}
\end{aligned} \tag{7.8}$$

where $(k_0, \tau, a_1, b_1, a_2, b_2)$ defines the overall set of parameters. The parameter ω_c was always set to a fixed value during the optimization process. Therefore, a 2 to 6 parameters optimization scheme could be chosen depending on the controller prototype. The choice of the number of parameters will generally be a trade-off between increased pressure reduction and increased convergence time for the controllers.

During the optimization some parameter combinations might be proposed that actually increase the pressure pulsations. This is of course very unfavorable in practical applications. For this reason, an *intermediate evaluation* of the cost function was introduced to speed up the convergence time of the algorithm. The underlying idea is that it is more important to have high accuracy during the evaluation

of a good parameter combination than a bad combination. Consequently, the cost function is evaluated twice: if the evaluation over a short period of time indicates pulsations higher than the no-control case, evaluation is stopped and a penalty on the fitness is imposed. If the first evaluation indicates pulsations lower than without control, the evaluation continues and the total cost function is returned as the fitness.

Generally, the pulsations levels are not the only parameters to be monitored. It might be possible that a certain combination of parameters could reduce the pressure oscillations but could also increase the emissions levels, like CO and NOx. Obviously, this is not desirable in a combustion chamber. However, the flexibility of the genetic algorithm allows to specify bounds to the emissions levels. If the emissions are higher than certain threshold, a penalty is given to the cost function. This last feature was noticed after tests, but it could not be actually implemented. So it could be the objective of future work, since this problem is critical due to the strict emissions regulations.

7.6 Active Control Implementation

The controllers were implemented in the test-rig using the dSpace system 'DS1103', which contains a DSP data acquisition board with 20 analog inputs and 10 outputs. This system has a direct interface with MATLAB/Simulink which facilitates the implementation of controllers using Simulink block diagrams. The sampling rate was specified at 12kHz, enough to capture the dynamics of the chaotic pressure measurement.

7.6.1 Active Control Performance Index

During the modeling stage, only the acoustic response of the combustor is considered. Consequently, the controller must be judged according with its capability to reduce pressure pulsations or noise in general inside of the chamber. So, the following two indices NRR (Noise Reduction Ratio) and PA (Peak Attenuation) are used to measure the controller performance

$$NRR = 10 \cdot \log_{10} \left[\frac{Pressure\ power_{on}}{Pressure\ power_{off}} \right] \ dB \tag{7.9}$$

$$PA = 20 \cdot \log_{10} \left[\frac{\max_{\omega} \hat{p}_{on}(\omega)}{\max_{\omega} \hat{p}_{off}(\omega)} \right] \ dB \tag{7.10}$$

where ω represents frequency, $\hat{p}(\cdot)$ Fourier Transform of the pressure measurement $p(t)$, the sub indices "on" and "off" indicate tests with controllers on and off respectively, and

$$Pressure\ power_{(\cdot)} = \frac{1}{N} \sum_{\omega} |\hat{p}_{(\cdot)}(\omega)|^2$$

with N denoting the number of samples in the pressure trace. It is important to notice that the definition of decibels (dB) is consistent with notation used in acoustics for sound power level [6].

Now, the actual computation of these two indices was carried out in MATLAB. Thus, measurements were recorded with and without control using the dSpace system and the final processing was computed in MATLAB. The *signal processing* toolbox was employed and the command *psd* was used to calculate the spectral density estimation of the pressure measurements.

7.6.2 Simulation

In order to obtain an estimation of the controller performance in the real combustor, closed-loop simulation was carried out using the experimental approximations,

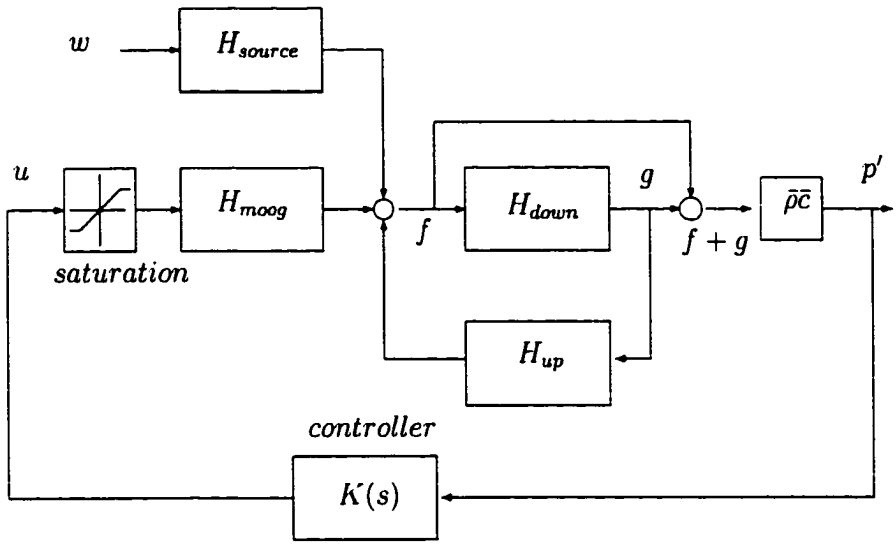

Figure 7.28: Combustor Closed-loop Simulation Model.

see Figure 7.28. The performance of the controllers previously computed with respect to the performance indices is summarized in Table 7.1. It is clear that $\mathcal{H}_\infty$ Disturbance Rejection and $\mathcal{H}_\infty$ Loop-Shaping controllers can achieve good attenuation factors at least during simulation. So, the next step was to test these controllers in the combustor test-rig to corroborate the performance.

Table 7.1: Simulation Results.

Controller Type	**PA** (dB)	**NRR** (dB)
$\mathcal{H}_\infty$ Disturbance Rejection	-16.15	-6.08
$\mathcal{H}_\infty$ Loop-Shaping	-13.95	-5.12

7.6.3 Test-Rig Results

Next, the controllers obtained through $\mathcal{H}_\infty$ optimization were tested in the experimental rig described earlier. In addition, the controllers optimized through the evolution algorithm, from now on referred as *Evolution controllers*, were also tested. Phase-delay control was used as baseline control strategy to judge the performance improvements with model-based and evolution controllers. The roots of phase-delay control strategy come from the *Rayleigh-Criterion*; thus fuel was modulated out-of-phase from the pressure measurement in order to disrupt the instability coupling. The phase-delay controller had the structure

$$K(s) = k_o e^{-s\tau} \tag{7.11}$$

where the parameters k_o and τ were updated manually during the experiment to obtain maximum suppression in the pressure pulsations.

The first test involved analyzing the response for each of the control strategies:

- Phase-Delay Control,
- $\mathcal{H}_\infty$ Disturbance Rejection,
- $\mathcal{H}_\infty$ Loop-Shaping, and
- Evolution Controllers

For this purpose, the same operating condition observed during modeling was achieved. Hence, without control the instability frequency was located at $\omega/\omega_0 = 0.2054$ and the amplitude of the pressure pulsations was about 2% the mean pressure. In the experimental testing, after the control was switched on the combustor was let reach a steady state response for about 30s. The response was then visualized using a

Table 7.2: Comparison between Baseline Controller, Model-Based and Evolution Controllers.

Controller Type	**PA** (dB)	**NRR** (dB)
Phase-Delay	-2.20	-2.69
$\mathcal{H}_\infty$ Disturbance Rejection	-19.79	-8.36
$\mathcal{H}_\infty$ Loop-Shaping	-19.42	-10.20
Evolution 2 param.	-18.00	-6.90
Evolution 4 param.	-18.70	-6.80
Evolution 5 param.	-26.20	-13.40
Evolution 6 param.	-26.70	-13.00

spectrum analyzer. The control was switched off and on again to check that the overall effect could be repeated. Next, experimental data was recorded with and without control for 15s, i.e. 180,000 samples. However, in order to facilitate the computation of the performance indices PA and NRR, only 2^{16} samples (i.e. 5.4s) were used. Nevertheless, this amount of samples is representative according with the time-scale associated with the instability. The results of this test are summarized in Table 7.2. From the table, it is clear that the proposed model-based and evolution controllers performed much better than simple phase-delay control. The evolution optimization was able to reach sets of parameters that led to large reduction of the pressure pulsations, even more than the model-based controllers in the case of 5 and 6-parameters controllers. The experimental responses for some of these controllers are plotted in Figures 7.29, 7.30, 7.31, 7.32 and 7.33.

During testing, a small delay-factor was added to the $\mathcal{H}_\infty$ Disturbance Rejection controller to maximize the pressure attenuation; so the frequency phase-variation of the controller was slightly adjusted. Consequently, this controller did not provide enough robustness to correct possible uncertainty during modeling. On the other hand, the $\mathcal{H}_\infty$ Loop-Shaping controller did not need any adjustment.

The structure of the resulting controllers coming from the evolution optimization for the 5 and 6-parameters cases is shown

$$K_{evolution_5}(\hat{s}) = 9.4 \times 10^{-4} \frac{(\hat{s}/0.2645 + 1)(\hat{s}/0.1047 + 1)}{(\hat{s}/0.5402 + 1)(\hat{s}/0.5284 + 1)(\hat{s}/1.2000 + 1)}$$

and

$$K_{evolution_6}(\hat{s}) = 1.28 \times 10^{-3} \frac{(\hat{s}/0.1100 + 1)(\hat{s}/0.1399 + 1)}{(\hat{s}/0.5262 + 1)(\hat{s}/0.3782 + 1)(\hat{s}/1.2000 + 1)} e^{-0.3142\hat{s}}$$

where $\hat{s} = s/\omega_0$. Essentially, from the pole-zero location of both controllers $K_{evolution_5}$ and $K_{evolution_6}$, it is clear they work as *lead* compensators. So they are providing

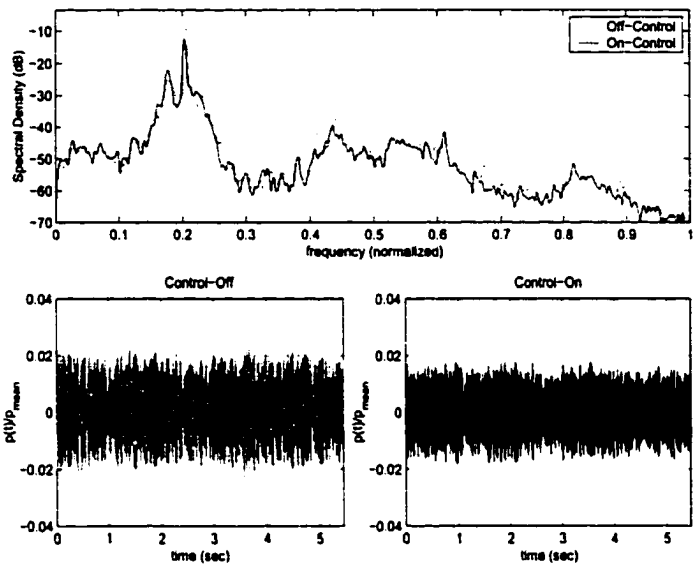

Figure 7.29: Test of Phase-Delay Control.

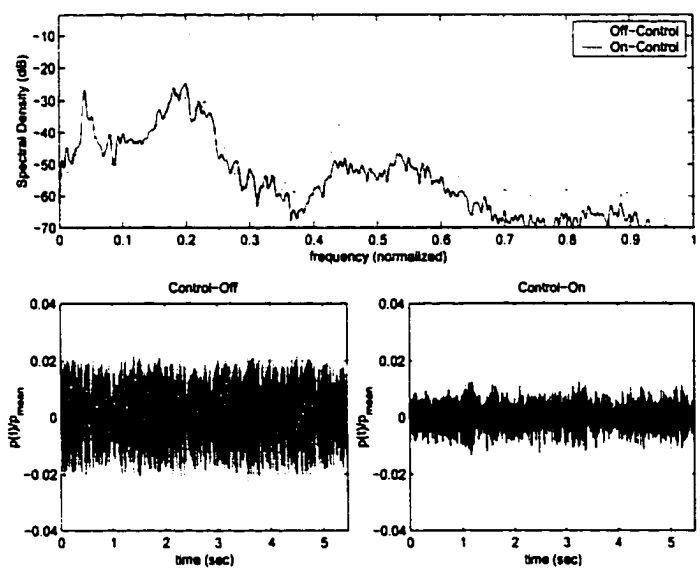

Figure 7.30: Test of $\mathcal{H}_\infty$ Disturbance Rejection Controller.

damping around the instability frequency. In Figure 7.34, the frequency responses of the $\mathcal{H}_\infty$ Disturbance Rejection and $\mathcal{H}_\infty$ Loop-Shaping are compared with the resulting controllers coming from the evolution optimization for the cases 5 and 6 parameters. From this plot, it is clear that all the controllers have a good agreement in magnitude and phase around the instability frequency $\omega/\omega_0 = 0.205$; explaining why the success of the evolution controllers.

Now, it was decided to investigate the robustness properties of the model-based controllers. For this purpose, a set of different operating conditions for the combustion chamber were used to test the controllers. First, the $\mathcal{H}_\infty$ Disturbance Rejection controller was set, including the delay factor added previously, and the parameters of the combustor were varied: λ, $\mathcal{P}$ and T_a. Four operating conditions were recorded. Again, measurements with and without control were acquired. The processing of the pressure measurements was carried out in MATLAB. The results are presented in Table 7.3. For each condition, the location of the pressure peak and the amplitude of the pressure pulsations changed. Therefore, a range of conditions starting from low to high pressure pulsations (stable to unstable) were tested. In Figures 7.35, 7.36 and 7.37, the responses for conditions I, II and IV are plotted.

Similarly, the $\mathcal{H}_\infty$ Loop-Shaping controller was tested thoroughly. Now, a set of 6 different working conditions was examined. Again, the model-based controller showed good robustness for changes in the chamber operating conditions, see Table 7.3. In Figures 7.38, 7.39 and 7.40, the experimental responses are presented for conditions II, III and IV.

Note that for different working conditions, the peak frequency did not change in a big range for the no-control case. This explains why both model-based $\mathcal{H}_\infty$ controllers were able to have a good performance for a wide range of operating

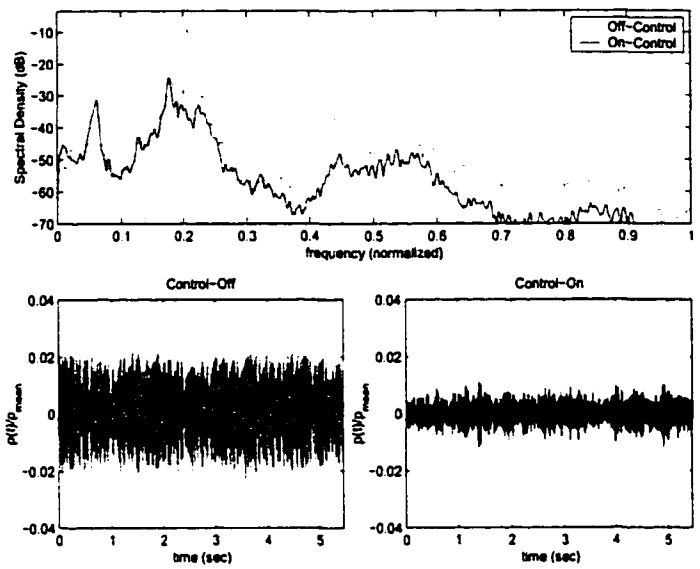

Figure 7.31: Test of $\mathcal{H}_\infty$ Loop-Shaping Controller.

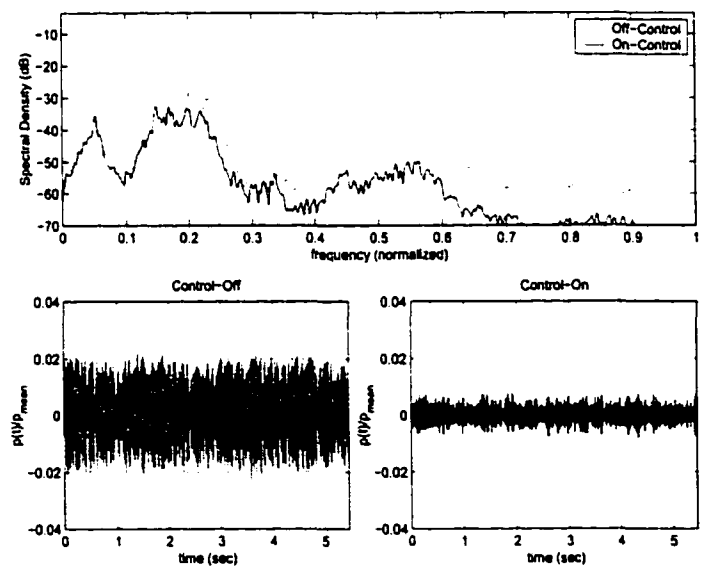

Figure 7.32: Test of Evolution Controller: 5-parameters.

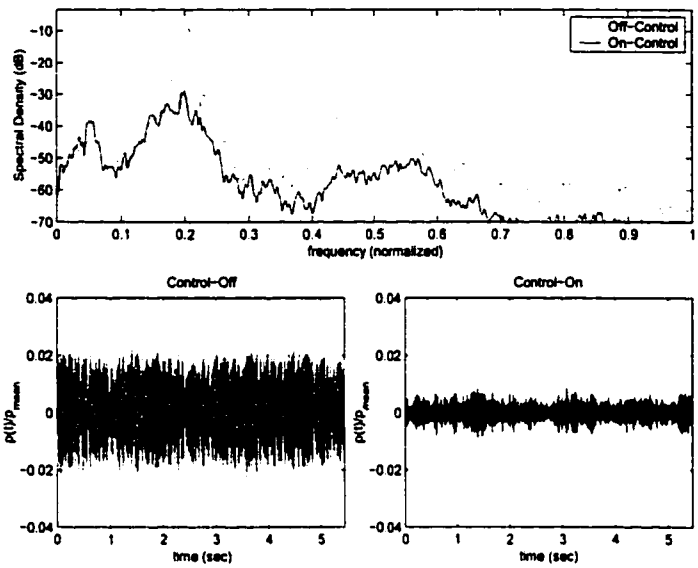

Figure 7.33: Test of Evolution Controller: 6-parameters.

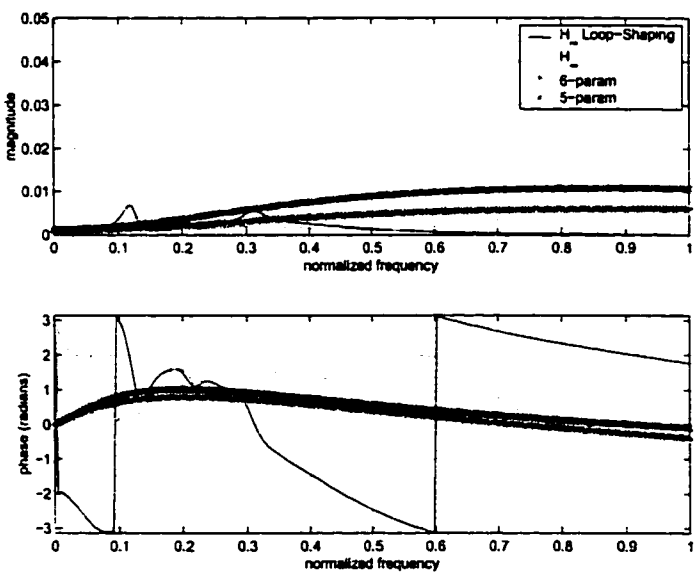

Figure 7.34: Frequency Response of Resulting Controllers.

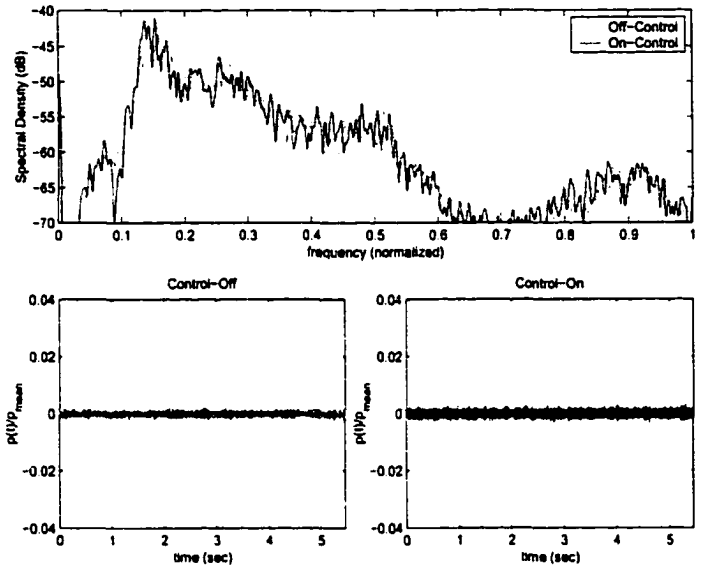

Figure 7.35: Test of $\mathcal{H}_\infty$ Disturbance Rejection Controller: Condition I.

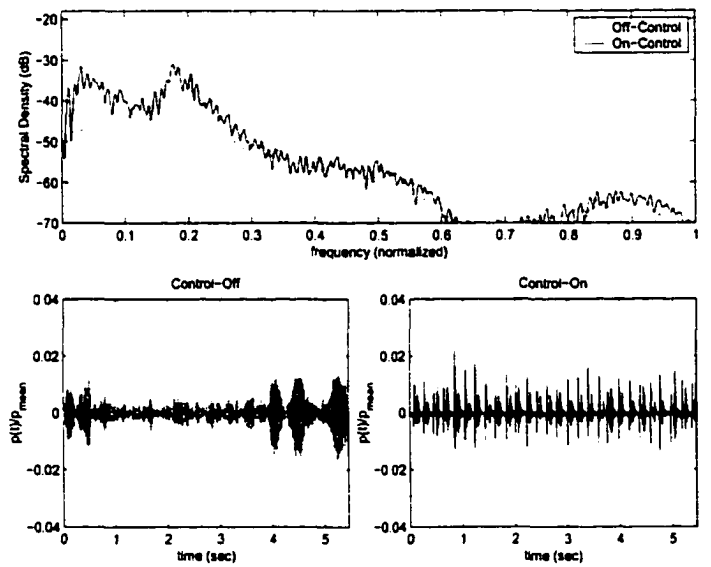

Figure 7.36: Test of $\mathcal{H}_\infty$ Disturbance Rejection Controller: Condition II.

conditions. At these different working points, the basic dynamics did not change much, only the intensity levels. Therefore, for unstable conditions (high pressure oscillations), the active-control strategy was able to reduce effectively the pressure pulsations. However, for the stable conditions, the control modulation had almost no effect in the pressure field. It was noticed that even though good attenuation for the pressure pulsations can be achieved for different conditions, the pollutant levels could raise for some operating conditions, especially the levels of UHC and CO. Meanwhile, the NOx level was almost always below the no-control level. The raise of UHC levels suggest that incomplete combustion was taking place inside of the chamber. On the other hand, it was not possible to identify a trend or pattern for this problem, or a relation between the working condition and the pollutants level. Clearly, this stands as the main drawback of the $\mathcal{H}_\infty$ formulation since in order to incorporate this parameter, a model describing the behavior of the pollutants must be derived, which is a very complicated task. However, there were some conditions where the UHC and CO were almost zero for the $\mathcal{H}_\infty$ controllers.

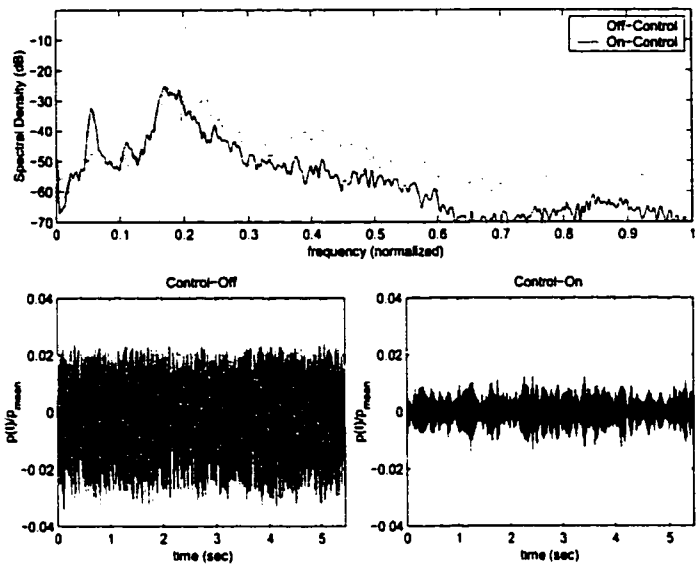

Figure 7.37: Test of $\mathcal{H}_\infty$ Disturbance Rejection Controller: Condition IV.

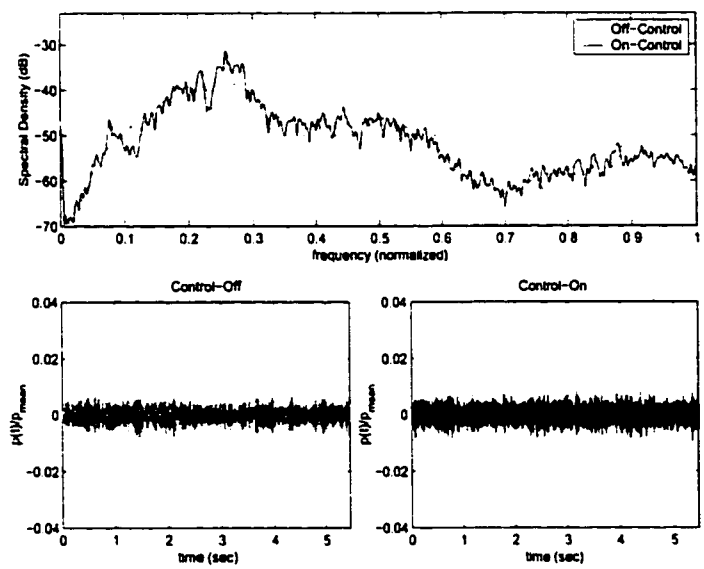

Figure 7.38: Test of $\mathcal{H}_\infty$ Loop-Shaping Controller: Condition II.

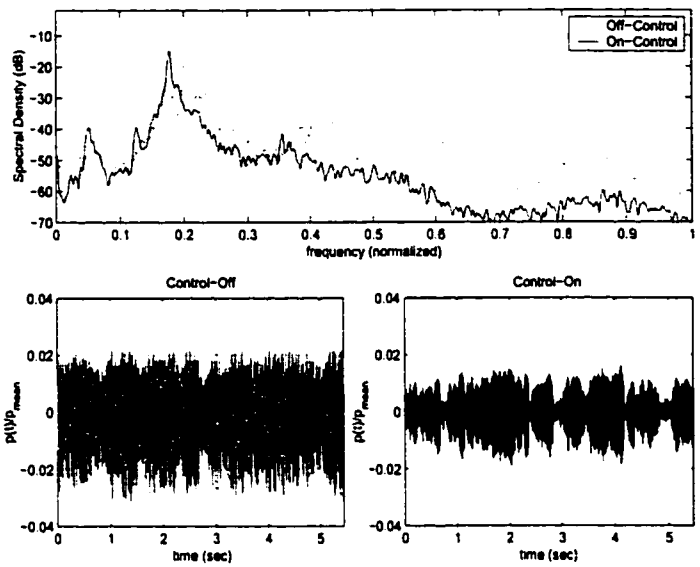

Figure 7.39: Test of $\mathcal{H}_\infty$ Loop-Shaping Controller: Condition III.

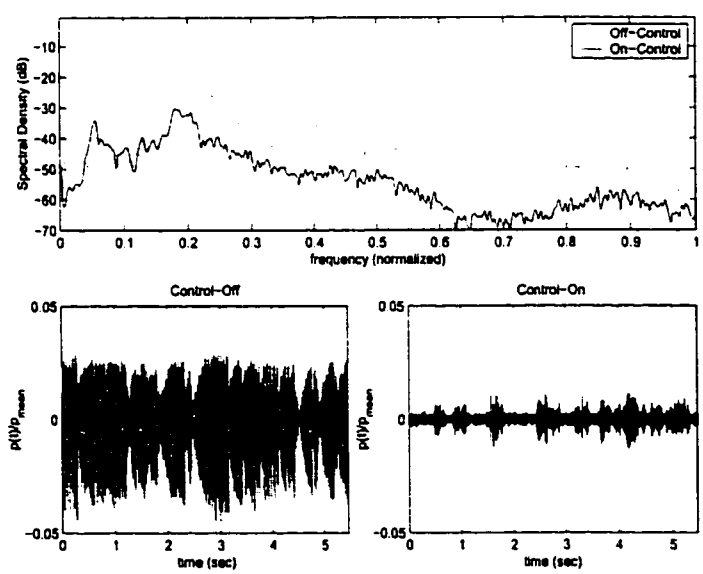

Figure 7.40: Test of $\mathcal{H}_\infty$ Loop-Shaping Controller: Condition IV.

Table 7.3: Test of Model-Based Controllers for Different Working Conditions.

Controller Type			**Control-Off**		**Control-On**	
	PA	**NRR**	**Peak freq.**	**Max. amp.**	**Peak freq.**	**Max amp.**
	(dB)	(dB)	(ω/ω_0)	$(p/\bar{p})$	(ω/ω_0)	$(p/\bar{p})$
$\mathcal{H}_\infty$ Dist. Reject. cond. I	2.16	0.59	0.16	0.0031	0.15	0.0034
$\mathcal{H}_\infty$ Dist. Reject. cond. II	-7.78	-3.36	0.18	0.0176	0.18	0.0219
$\mathcal{H}_\infty$ Dist. Reject. cond. III	-21.88	-10.95	0.20	0.0385	0.17	0.0279
$\mathcal{H}_\infty$ Dist. Reject. cond. IV	-20.00	-12.00	0.20	0.0398	0.17	0.0140
$\mathcal{H}_\infty$ Loop-Shaping cond. I	-17.30	-11.40	0.20	0.0421	0.05	0.0270
$\mathcal{H}_\infty$ Loop-Shaping cond. II	-3.32	-0.60	0.25	0.0109	0.26	0.0094
$\mathcal{H}_\infty$ Loop-Shaping cond. III	-8.08	-6.56	0.20	0.0373	0.18	0.0192
$\mathcal{H}_\infty$ Loop-Shaping cond. IV	-24.96	-16.17	0.21	0.0478	0.18	0.0135
$\mathcal{H}_\infty$ Loop-Shaping cond. V	-18.63	-13.28	0.21	0.0412	0.18	0.0134
$\mathcal{H}_\infty$ Loop-Shaping cond. VI	-19.44	-14.10	0.21	0.0372	0.21	0.0130

CHAPTER 8

ACTIVE CONTROL OF A LIQUID-FUELED COMBUSTOR

The work described in this chapter was carried out in the Mechanical Engineering Department at LSU. In this department, extensive experimental work have been carried for many years pursuing to understand the mechanisms and driving effects of thermoacoustic instabilities in test-rigs. Simple control strategies such as phase-delay control have been tested with success. However, the simplicity of these techniques makes them very sensitive to variations in the operating conditions. As a result, the performance of more advanced control techniques was not clear. In addition, compared to our previous application (Chapter 7) the combustor test-rig is now liquid fueled. The objective of this work was then to expand our previous work in this area. Identification techniques were proposed for modeling the combustor and different control actuators were also tested. LQG and $\mathcal{H}_\infty$ Loop-Shaping controllers were derived from the experimental models and implemented in the combustor achieving good attenuation factors for the pressure oscillations.

8.1 Experimental Setup

Active control tests were performed on a 125kW swirl-stabilized spray combustor. The combustor facility consists of two sections: the settling chamber and the combustion chamber. Two concentric pipes serve as the primary and secondary air settling chambers as shown in Figure 8.1. Each settling chamber has an array of

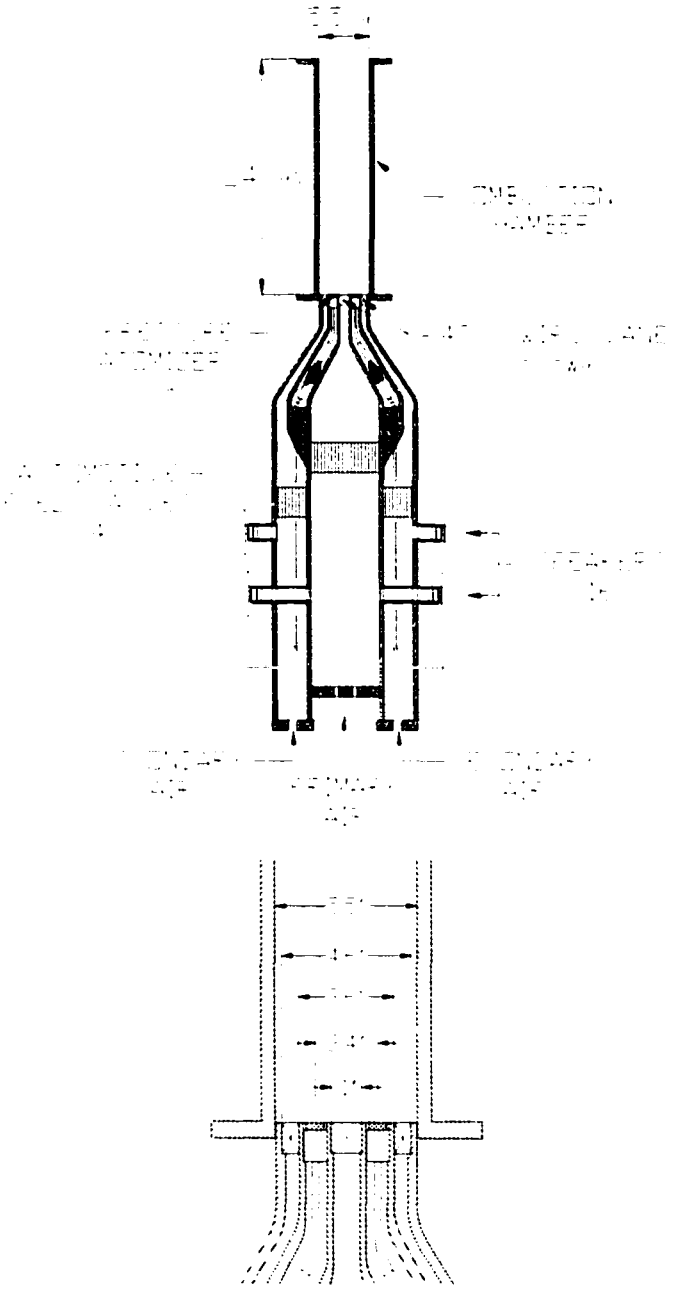

Figure 8.1: Experimental Test-Rig at Mechanical Department at LSU.

eight loudspeakers (Sanming 75A) that are mounted at equal polar angles about the chamber's circumference. The primary and secondary air from the settling chambers are accelerated into the combustion chamber through concentric large area ratio nozzles. Swirl vanes having a 45° co-swirl orientation are placed at the exit of the nozzles. Uniformly located between the coaxial air jets are eight pressure-fed atomizers. Four of the eight fuel sprays are operated at a constant fuel-rate and the other four are modulated using automotive-type fuel injectors.

The combustion chamber has a diameter of 5.5in and a length of 22in. The exit of the combustion chamber was unrestricted. In addition, the chamber was artificially cooled by using water. High frequency response pressure transducers (Kistler 6061B and 7061B) placed along the length of the combustion chamber wall were used to monitor the instability. A pressure sensor located at a distance of x/L=0.2 from the dump plane provided the feedback signal for the control implementation. The pressure signal was sampled at a rate of 10kHz and then processed using a dSPACE 'DS1103' PPC Control Board. The control algorithms were implemented in discrete time using MATLAB/Simulink programs in conjunction with the dSPACE software.

8.2 Fuel Modulation

First, control using fuel modulation was investigated. In this setup, four modulated fuel sprays were used for control purpose. So, the controller received the signal coming from the pressure transducer and processed it to produce the control signal for the automotive fuel-injectors. However, fuel injectors are not proportional actuators, i.e. they cannot open or close proportionally to the signal applied to their terminals. These actuators are just fully open or fully closed. If the control signal to the injectors is below certain threshold voltage ($\approx$ 11.8V) the injectors are

closed. Similarly, if the input signal is above the threshold, the injectors are fully open. Therefore, it was decided to send a discrete signal to the injectors 0V or 12V to close or open the valves respectively. Note that there are only two parameters that can be selected in the response of these actuators: frequency and duty cycle. However, by previous work by Allgood [1], the fuel injectors have a limited working response since the frequency bandwidth changes dramatically according with the duty cycle. Thus, the best response is achieved for a 25 to 75% duty cycle.

At this stage, only linear control theory was intended to be applied for the controller derivation and clearly this type of control actuators are adding a nonlinear behavior into the system. The approach taken was to apply a sign nonlinearity at the output of the controller producing then a discrete signal for the fuel injectors. Note that due to this sign nonlinearity, the injectors driving signal is pulse-width modulated according to the continuous time controller; the width of the pulses will depend on the zero-crossing of the control signal. This fact will compensate somewhat the nonlinear response of the actuators. However, the response of the linear controllers to this type of nonlinearity is not known,

8.2.1 Operating Condition

In the initial stage of the test, an operating condition that clearly presented a thermoacoustical instability in the combustor was selected. The amount of fuel into the chamber was set constant to 4.5gph. Therefore, the fuel through the four constant nozzles was fixed to 2.5gph and the modulated fuel-stream was set to 2.0gph. Now, the primary air flow was varied from 12 to 30cfm and the secondary was varied from 30 to 100cfm in order to find an operating condition that showed an instability. Thus, the chosen working condition is presented in Table 8.1. At this working

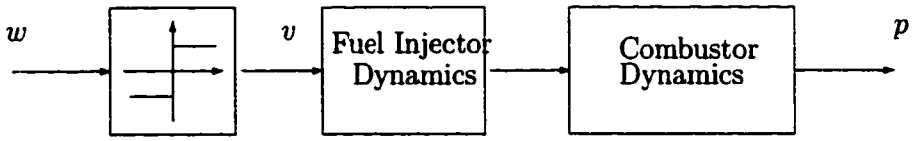

Figure 8.2: Fuel Modulation Identification Technique.

condition, the instability peak was dominant over the background turbulence in the chamber and it was at 280Hz.

Table 8.1: Parameters of Baseline Condition in the Fuel Modulation Test

Fuel-Flow Rate	$Q_{primary}$	$Q_{secondary}$	Pressure
4.5gph	22cfm	60cfm	atmospheric

8.2.2 Time-Domain Modeling

The first step towards the controller synthesis was to derive a model of the combustor that captured the basic interactions inside of the chamber. Thus, the objective of modeling is only control design. As a result, the combustor model should present the main dynamics from the control actuator signal to the pressure measurement. In the identification approach, band-limited (0 to 1kHz) white noise w was sent into the system and the pressure measurement was recorded as shown in Figure 8.2. As explained earlier, a sign nonlinearity was used to modulate the driving signal to the fuel injectors. Therefore, the actual signal going into the fuel injectors, v, is white noise, w, passed through a sign nonlinearity.

Frequency domain identification was disregarded due to the harmonics that the nonlinearities of the system are adding into the measurements. Thus, it was decided

to pursue the identification of the combustor in *time domain* using the input-output pair (v,p). The data was collected by the dSpace system 'DS1103' at a sampling rate of 10kHz. 2^{15} input-output samples ($\approx$ 3.3s) were used in the identification scheme. This amount of data is representative considering the time-scales related to the instability frequency. Four parametric model structures were considered

- ARX (Least-Square Approximation)

$$A(z^{-1})y[n] = B(z^{-1})u[n-k] + e[n] \tag{8.1}$$

- ARMAX (Least-Square Approximation)

$$A(z^{-1})y[n] = B(z^{-1})u[n-k] + C(z^{-1})e[n] \tag{8.2}$$

- State-Space (Sub-Space Method)

$$\begin{aligned} x[n+1] &= Ax[n] + Bu[n] \\ y[n] &= Cx[n] + Du[n] + v[n] \end{aligned} \tag{8.3}$$

where

$$\begin{aligned} A(z^{-1}) &= 1 + a_1 z^{-1} + \cdots + a_N z^{-N} \\ B(z^{-1}) &= b_0 + b_1 z^{-1} + \cdots + b_M z^{-M} \\ C(z^{-1}) &= c_0 + c_1 z^{-1} + \cdots + c_P z^{-P} \end{aligned}$$

(A, B, C, D) are real matrices, and $\{a_i, b_i, c_i\}$ are real coefficients. Six models in discrete time were derived using the experimental data (v,p). For this purpose, the *identification toolbox* of MATLAB was used. The commands *arx*, *armax* and *n4sid* computed the approximations from the experimental data pair using the ARX,

ARMAX and State-Space structures respectively. In each case, the parameters of each model structure were chosen to optimize the fitting to the input-output pair. These models were further transformed to continuous time by bilinear transformation with 'prewarping' at 280Hz (instability frequency). This transformation was carried out using the command *d2cm* from the *control* toolbox of MATLAB. The six models in continuous time G_1, G_2, G_3, G_4, G_5 and G_6 are presented next

$$G_1(s) = \frac{-0.00070426(s-2\times10^4)^4(s+1150)(s^2+1192s+1.678\times10^7)}{(s+9.239\times10^4)(s+2\times10^4)^3(s+1916)(s^2+787.2s+2.769\times10^6)} \cdot \frac{(s^2+1791s+2.335\times10^8)(s^2+7059s+6.847\times10^8)}{(s^2+8600s+1.807\times10^8)(s^2+1.58\times10^4s+9.469\times10^8)} \cdot \frac{(s^2+1.321\times10^4s+1.146\times10^{10})}{(s^2+7.297\times10^4s+2.66\times10^9)} \quad (8.4)$$

$$G_2(s) = \frac{-0.00042916(s+1922)(s+2\times10^4)^5(s-2\times10^4)^4}{(s+9.277\times10^4)(s+1918)(s^2+786.8s+2.767\times10^6)} \cdot \frac{1}{(s^2+8598s+1.806\times10^8)(s^2+1.58\times10^4s+9.469\times10^8)} \cdot \frac{1}{(s^2+7.27\times10^4s+2.652\times10^9)} \quad (8.5)$$

$$G_3(s) = \frac{1.7178\times10^{-5}(s-2\times10^4)(s-2114)(s-1134)}{(s+39.3)(s^2-4.834s+3.13\times10^6)} \quad (8.6)$$

$$G_4(s) = \frac{-9.8703\times10^{-5}(s-2\times10^4)(s-2187)(s-171.8)}{(s-21.51)(s^2+56.8s+3.13\times10^6)} \cdot \frac{(s^2+614.4s+1.175\times10^7)}{(s^2+2882s+3.395\times10^7)} \quad (8.7)$$

$$G_5(s) = \frac{-0.00021209(s-7.877\times10^4)(s+2\times10^4)(s+8953)(s-1637)}{(s+9.77\times10^4)(s+16.82)(s^2+27.28s+3.144\times10^6)} \cdot \frac{(s^2-1427s+8.229\times10^6)(s^2-3.612\times10^4s+8.746\times10^8)}{(s^2+9071s+7.753\times10^7)(s^2+2.09\times10^4s+1.051\times10^9)} \quad (8.8)$$

$$G_6(s) = \frac{-1.6035e-05(s-2\times10^4)(s-2694)(s^2-303.5s+6.57\times10^6)}{(s+1.149\times10^4)(s+18.34)(s^2+10.94s+3.138\times10^6)} \cdot \frac{(s^2+5.553\times10^4s+1.326\times10^{10})}{(s^2+4.42\times10^4s+1.159\times10^9)} \quad (8.9)$$

The frequency responses for these models are shown in Figures 8.3 and 8.4. Note that all the six models present similar characteristics around the instability frequency 280Hz.

8.2.3 Controller Synthesis

LQG and $\mathcal{H}_\infty$ Loop-Shaping controllers were derived for the six models obtained early. The following parameters for the LQG synthesis were chosen $Q = 1 \times 10^3$, $R = 1$, $Q_n = 10$ and $R_n = 10$. The synthesis was completed by using the commands *lqr* and *kalman* from the *control toolbox* [28] of MATLAB. During the LQG design some of the resulting controllers were unstable. So, the parameters of this design technique (Q, R, Q_n, R_n) were varied to obtain stable controllers, but in the cases of models 2 and 3 this was not possible. As a result, the controllers corresponding to these models were discarded. The frequency responses of the resulting controllers for LQG design are shown in Figure 8.5. Similarly, $\mathcal{H}_\infty$ Loop-Shaping was also applied. The weighting function

$$W(s) = \frac{928532.3821(s + 0.6283)}{(s + 188.5)(s^2 + 351.9s + 3.095 \times 10^6)}$$

was used in the shaping of the open loop plant. Its frequency response is plotted in Figure 8.6. This weighting function stresses the importance of the control authority at the instability frequency 280Hz. The command *ncfsyn* from the *μ-synthesis toolbox* [5] of MATLAB was used to compute the optimal $\mathcal{H}_\infty$ Loop-Shaping controllers. In Figure 8.7, the resulting controllers from the synthesis process are shown.

The facilitate the implementation of the controllers, model reduction by balance truncation was applied to the LQG and $\mathcal{H}_\infty$ Loop-Shaping controller [80]. Thus, states that were not relevant in the shape of the frequency response were disregarded. The commands *balreal* and *modred* were employed for this purpose [28].

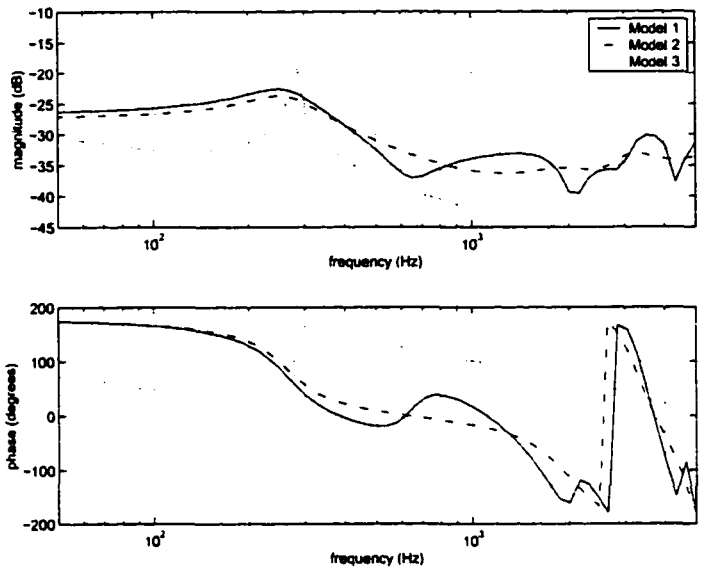

Figure 8.3: Models Obtained Through Fuel Modulation: 1, 2 and 3.

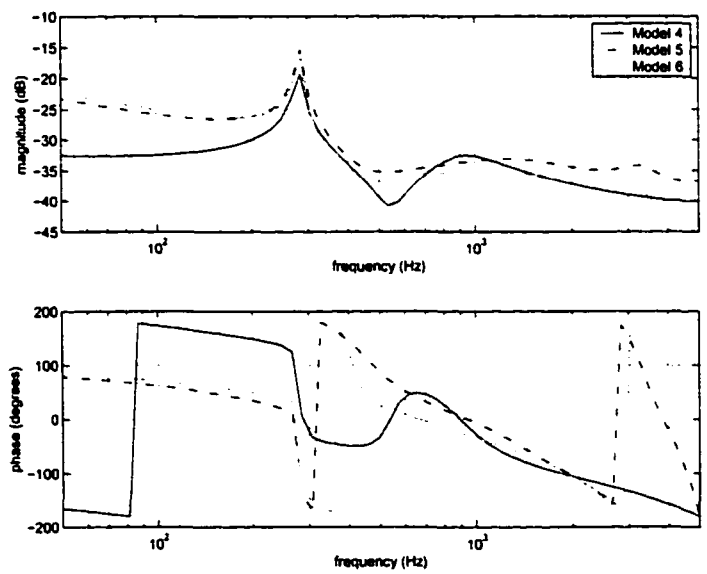

Figure 8.4: Models Obtained Through Fuel Modulation: 4, 5 and 6.

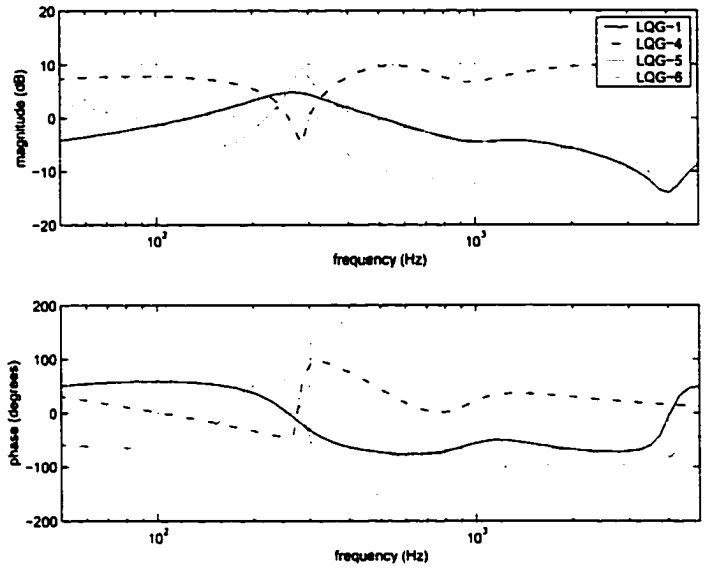

Figure 8.5: LQG Controllers for Fuel Modulation Test.

8.2.4 Controller Implementation

Now, the controllers derived were tested in the experimental rig. The controllers were implemented in the dSpace system 'DS1103' through a Simulink/MATLAB interface. Manually delays were added to the controllers to compensate any uncertainties coming from modeling; the phase roll-off was adjusted. On one hand, the LQG controllers synthesized from models 4, 5 and 6 did not attenuate the pressure oscillations even with the addition of the delay term. Meanwhile, the LQG controller for model 1 needed a delay adjustment of 0.5ms to improve its performance. On the other hand, all the $\mathcal{H}_\infty$ Loop-Shaping controllers produced good pressure attenuation. However, the controllers for models 1, 2, 4 and 5 needed a delay adjustment of 1.2ms, 1.2ms, 1.9ms and 0.95ms respectively. Note that the controllers coming from models 3 and 6 did not need any adjustment and also produced the highest pressure reductions.

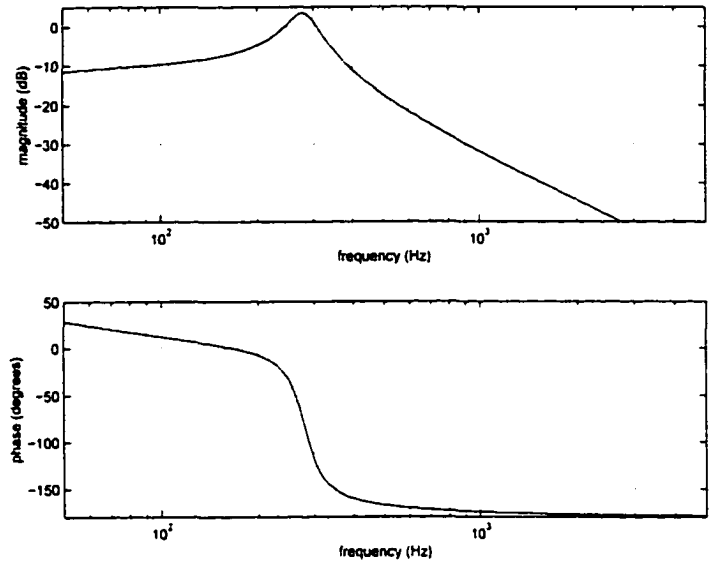

Figure 8.6: $\mathcal{H}_\infty$ Loop-Shaping Weighting Function for Fuel Modulation Test.

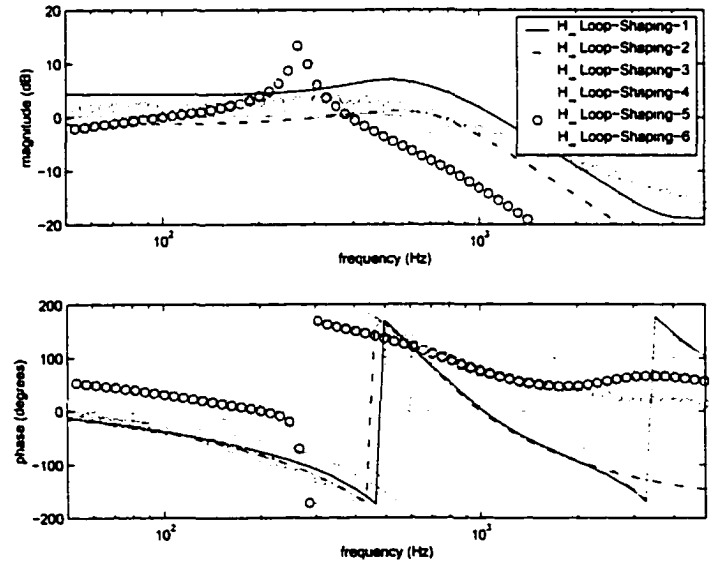

Figure 8.7: $\mathcal{H}_\infty$ Loop-Shaping Controllers for Fuel Modulation Test.

In addition, phase-delay control was tested as baseline control strategy. This controller was implemented using a band-pass filter from 80 to 500Hz in series with a gain and a delay factor. The band-pass filter was added to remove any low and high frequency noise coming in the pressure measurement. The delay and gain were manually adjusted until maximum suppression was achieved, the optimum delay was obtained at 0.6ms. In order to judge the response of the controllers, the performance indices PA (7.10) and NRR (7.9) previously defined in Chapter 7 were used. 2^{15} samples ($\approx$ 3.3s) of the pressure measurement were employed in the computation of PA and NRR. This pressure measurement is representative of the system, according with the time-scale associated with the instability. The processing of the data was carried out in MATLAB using the *signal processing toolbox*. A summary of the test results is presented in Table 8.2. Surprisingly, the phase-delay control performed almost as good as the LQG and $\mathcal{H}_\infty$ Loop-Shaping controllers. The experimental responses of the combustor with phase-delay, LQG and $\mathcal{H}_\infty$ Loop-Shaping controllers are shown in Figures 8.8, 8.9 and 8.10.

Remark 8.1 *A natural question arose, why the phase-delay controller performed almost equally well as the model-based controllers. If the frequency response of the successful model-based controllers (with the provided delay adjustment) is compared with the phase-delay control, see Figure 8.11, it is clear that all the controllers have a similar phase value and roll-off around the instability frequency* $280Hz$. *Now, since there is no proportional gain adjustment due to the type of control actuator used (fuel-injector), it can be argued that only the filtering and phase shift capabilities of the controllers are being applied.*

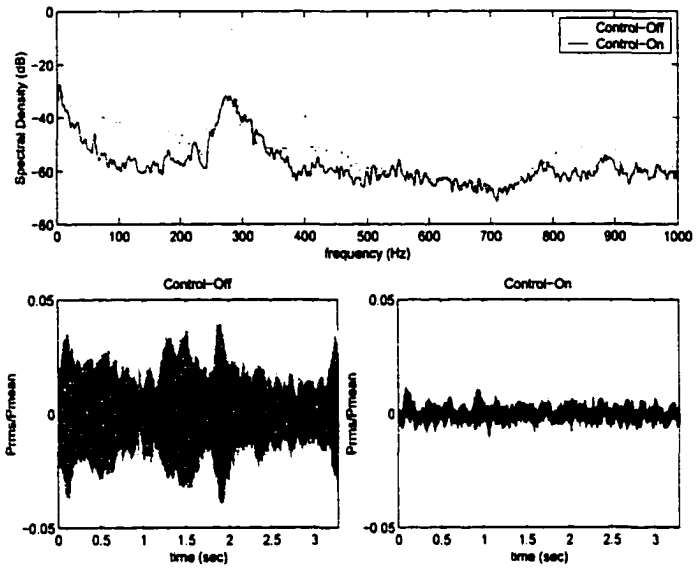

Figure 8.8: Experimental Pressure Spectra and Time Traces for Open-loop and Phase Delay Control in Fuel Modulation Test.

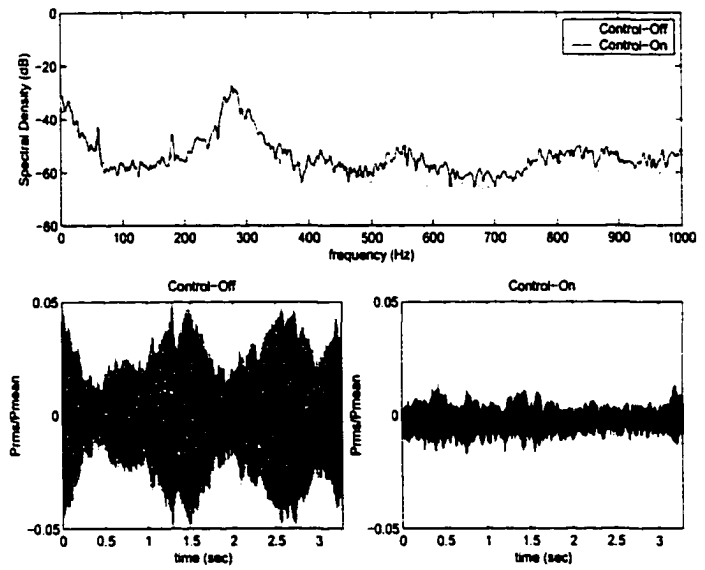

Figure 8.9: Experimental Pressure Spectra and Time Traces for Open-loop and LQG Control (Model 1) in Fuel Modulation Test.

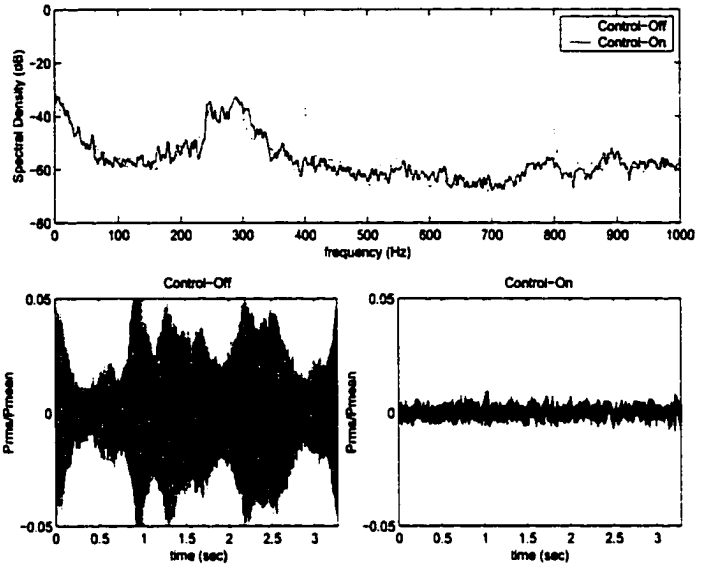

Figure 8.10: Experimental Pressure Spectra and Time Traces for Open-loop and $\mathcal{H}_\infty$ Loop-Shaping Control (Model 6) in Fuel Modulation Test.

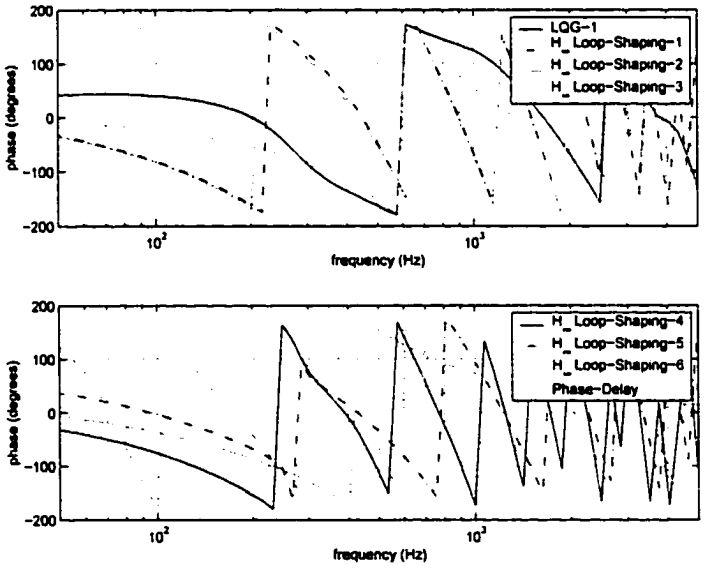

Figure 8.11: Resulting Controllers for Fuel Modulation Test after Delay Adjustment.

Table 8.2: Table Summary of Controllers Performance Using Fuel Modulation Control

Controller Type	**PA** (dB)	**NRR** (dB)
Phase-Delay	-25.77	-15.68
LQG-1	-24.88	-16.55
$\mathcal{H}_\infty$ Loop-Shaping-1	-17.57	-9.59
$\mathcal{H}_\infty$ Loop-Shaping-2	-22.02	-13.00
$\mathcal{H}_\infty$ Loop-Shaping-3	-23.18	-14.43
$\mathcal{H}_\infty$ Loop-Shaping-4	-21.22	-13.50
$\mathcal{H}_\infty$ Loop-Shaping-5	-19.47	-13.11
$\mathcal{H}_\infty$ Loop-Shaping-6	-29.77	-19.24

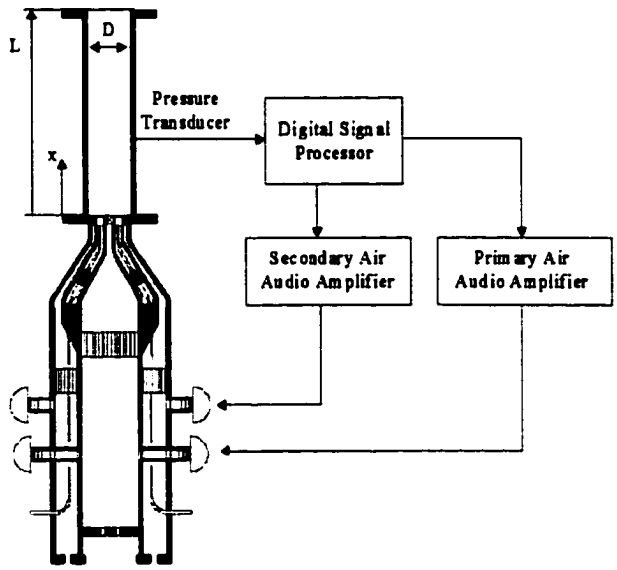

Figure 8.12: Combustor with Acoustic Control (Mechanical Department at LSU).

8.3 Acoustic Control

In our previous experiments, control using fuel modulation did not show any substantial difference between model-based controllers and phase-delay control. One possible explanation is the lack of proportional actuation by the fuel injectors. Therefore, it was decided to investigate active control using loudspeakers. These actuators present a proportional response to their input voltage. Thus, a conclusion could be drawn about the performance of fuel injectors as actuators in active control. Moreover, the performance of model-based controllers over phase-delay could also be fairly analyzed. In this new setup, the loudspeakers in the settling chamber of the combustor were used as control actuators as shown in Figure 8.12. The control signal coming from the dSpace board was first amplified by four 250 watt audio amplifiers (Radio Shack MPA-250) and then sent to the control loudspeakers. The

level of acoustic forcing was a function of the controller gain and the level of pressure oscillations. However, the audio amplifiers had a limitation of 0.6V input magnitude. At all forcing levels, there was no noticeable effect on the flame structure due to acoustic forcing.

8.3.1 Operating Condition

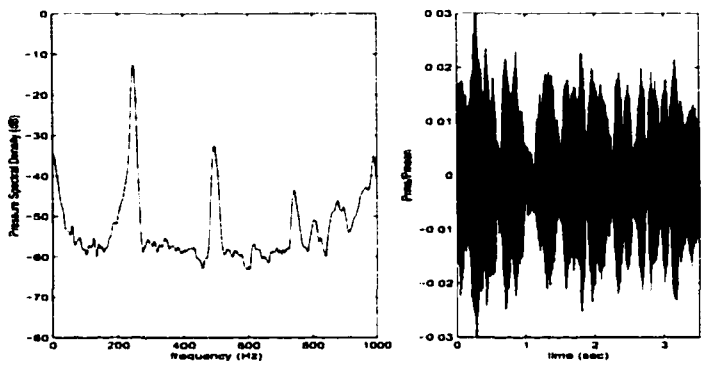

Figure 8.13: Pressure Spectra and Time Trace for the Open-loop Baseline Case ($Q_{primary}$ = 24cfm, $Q_{secondary}$ = 100cfm).

The primary and secondary air flowrates were varied from 12 to 30cfm and 30 to 100cfm respectively to determine the behavior of the instability. The fuel flowrate was maintained at 5gph throughout the testing. The combustor exhibited one dominant instability mode whose frequency changed with the air flowrates. This dominant mode varied with the secondary air flowrate roughly in the interval of 250 to 300Hz. The air flowrates chosen in this study were 24cfm for the primary air ($Q_{primary}$) and 100cfm for the secondary air ($Q_{secondary}$), see Table 8.3.1. This particular flow condition was chosen since it presented a clear dominant instability frequency. A sample time trace and power spectral density of the pressure fluctuations for this baseline condition are shown in Figure 8.13. The instability at the

baseline condition occurred at a frequency of 250Hz with the presence of a noticeable second harmonic at 500Hz. A low-frequency component in the pressure fluctuations is also noted in Figure 8.13. The origin of this low-frequency mode could not be exactly determined. Nevertheless, from the observations made in the test-rig, it was clear that this was not a Lean-Blow-Out effect. The levels of oscillations within the combustor were of the order of 2% of the mean (atmospheric) pressure for the baseline condition.

Table 8.3: Parameters of Baseline Condition in the Acoustic Modulation Test.

Fuel-Flow Rate	$Q_{primary}$	$Q_{secondary}$	Pressure
5.0gph	24cfm	100cfm	atmospheric

Acoustic forcing was used to identify the dynamics of the system from which experimental models were derived. Based on these models, feedback controllers were developed and implemented using the loudspeakers as control actuators.

8.3.2 Acoustic Modeling

Overall the combustor is modeled as a network of acoustic elements. Two strategies for acoustic forcing were explored and accordingly two combustor models were derived as shown in Figure 8.14. In this picture, u_p and u_s represent the control signals sent to the loudspeakers driving the primary and secondary air-streams respectively, u_{ps} denotes the control signal applied to both channels simultaneously, w represents white noise and p is the pressure measurement. In Figure 8.14, only the input and output signals are shown and the details of the complex thermo-acoustic processes inside the combustor are not explicitly represented; rather, their

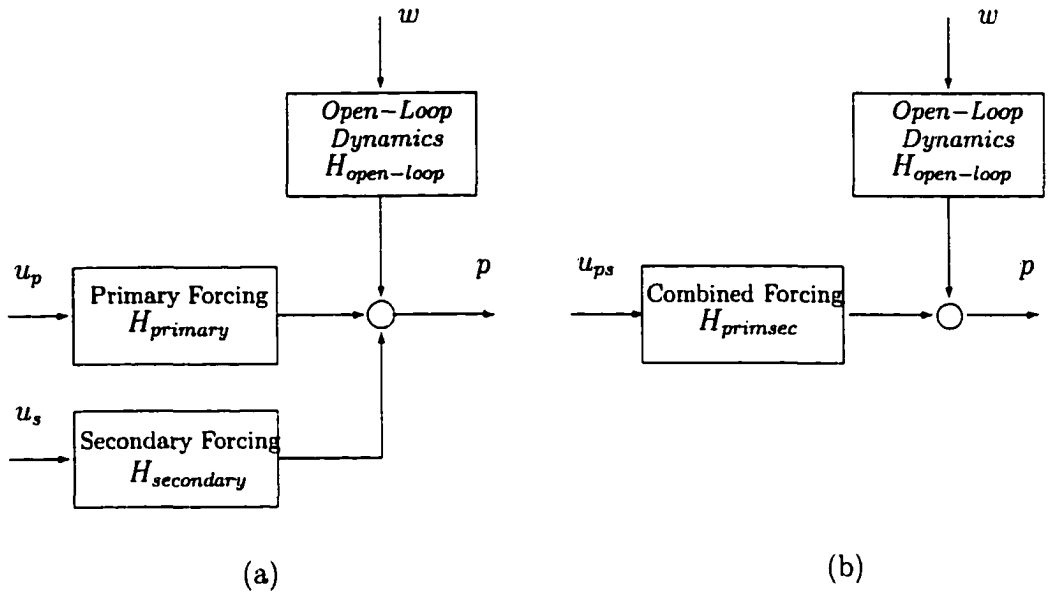

Figure 8.14: Combustor Model Structure (a) 2 Control Channels and (b) 1 Control Channel.

effects are represented by the transfer functions as $H_{primary}$, $H_{secondary}$ or $H_{primsec}$. In the open-loop case ($u_s = u_p = 0$ and $u_{ps} = 0$ in Figure 8.14), the model proposed is based on the assumption that the flame behaves as a noise source [39]. Consequently, the combustor is represented as a stochastic system. Hence, for this condition the combustor dynamics are presented as a continuous excitation source modeled as colored white noise. Due to this continuous excitation to the system, this block model was artificially assumed to be driven by a white noise source w. Thus in order to obtain this model, the pressure signal was recorded without control actuation applied to the combustor. A pressure trace of 2^{15} samples was taken at a sampling rate of 10kHz by the dSpace system. Note that this sampling rate is fast enough to capture the dynamics of the combustion instability (250Hz). The processing of the measurement was carried out in MATLAB by using the *signal processing* and *μ-synthesis* toolboxes [5]. The pressure data was transformed to

the frequency domain to obtain $\hat{H}_{openloop}(\omega)$ by the command *psd*. The experimental frequency data is shown in Figure 8.15. From this plot, the instability frequency is located around 250Hz. So, a model only in the interval 0 to 1kHz was chosen. Next, the command *fitsys* was applied to fit the magnitude of the frequency data with a stable transfer function $H_{openloop}(s)$. During the fitting process, the phase information was discarded since this block is assumed to be driven by a white noise source. A 12^{th} order transfer function was needed to accurately fit the data.

From the description of the test-rig, there are two control channels. The acoustic forcing of the primary and secondary airflows was achieved by a set of 8 loudspeakers in each channel. Thus, the identification of the combustor response to these actuators was now pursued. In the identification method, band-limited white noise (0 to 1kHz) was applied to the speakers and the corresponding pressure signal was recorded. To avoid clipping of the acoustic amplifiers, the level of the white noise was limited to 0.6V in magnitude. In addition, due to the continuous excitation coming from the flame interactions, the pressure signal must be correlated with the identification input signal to be able to extract the response of the combustor to this test signal. Thus, the experimental frequency response $\hat{H}(\omega)$ was computed by

$$\hat{H}(\omega) = \frac{S_{uy}(\omega)}{S_{uu}(\omega)} \tag{8.10}$$

where $S_{uy}(\omega)$ and $S_{uu}(\omega)$ denote the input-output cross-spectral density and the input auto-correlation respectively in frequency domain. The function *csd* from the *signal processing* toolbox was employed. The next step is to fit a rational transfer function $H(s)$ to this frequency data $\hat{H}(\omega)$. This fitting is again computed by the command *fitsys*, or alternatively could be done by using *invfreqs*. It is of particular interest to fit the frequency response data with a stable transfer function since this will simplify the control design and help to simulate the combustor

model accurately. In fact, the commands *fitsys* and *invfreqs* allow to restrict the fitting process to stable transfer functions. It is important to mention that this representation from control signal-to-pressure measurement contains information about the actuator response (loudspeakers), heat-release and pressure dynamics to control excitations. However, they are lumped in just one transfer function block.

Two identification strategies were taken. In the first one (cf. Figure 8.14a), each control channel was identified separately. So, the experimental frequency response corresponding to the mapping primary speakers to pressure measurement was computed as $\hat{H}_{primary}(\omega)$. Similarly, another mapping from the secondary control speakers to the pressure measurement was derived as $\hat{H}_{secondary}(\omega)$. Therefore, two pressure traces were recorded: one with excitation in the primary speakers and another one with excitation in the secondary speakers. 2^{15} samples at 10kHz were acquired in each case. Next, the identification method outlined earlier was applied to compute the experimental frequency responses. The corresponding frequency data for these two mappings $\hat{H}_{primary}(\omega)$ and $\hat{H}_{secondary}(\omega)$ are plotted in Figures 8.16 and 8.17. Note that from the phase plot of $\hat{H}_{secondary}(\omega)$, there was a large time-lag associated with the secondary forcing.

In the second approach (cf. Figure 8.14b), the same white noise signal was applied simultaneously to both primary and secondary speakers. Consequently, only one response $\hat{H}_{primsec}(\omega)$ from the control speakers to the pressure measurement was obtained. Thus, in this case just one pressure measurement was needed; again 2^{15} samples of the pressure signal were used in the identification process. In Figure 8.18, the frequency response of $\hat{H}_{primsec}(\omega)$ is shown. Note that the time-lag associated with the secondary forcing was still present in the frequency response.

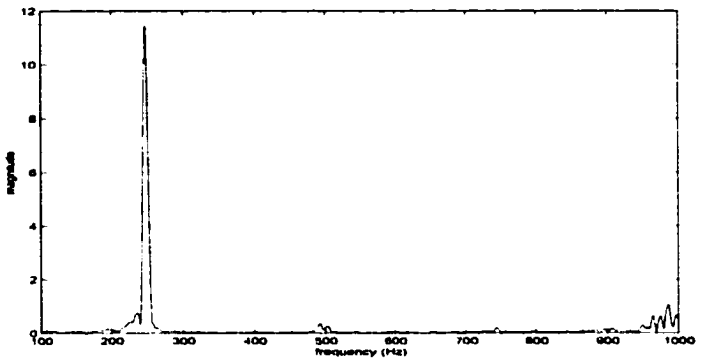

Figure 8.15: Experimental Frequency Response, $\hat{H}_{openloop}(\omega)$, of Combustor Dynamics.

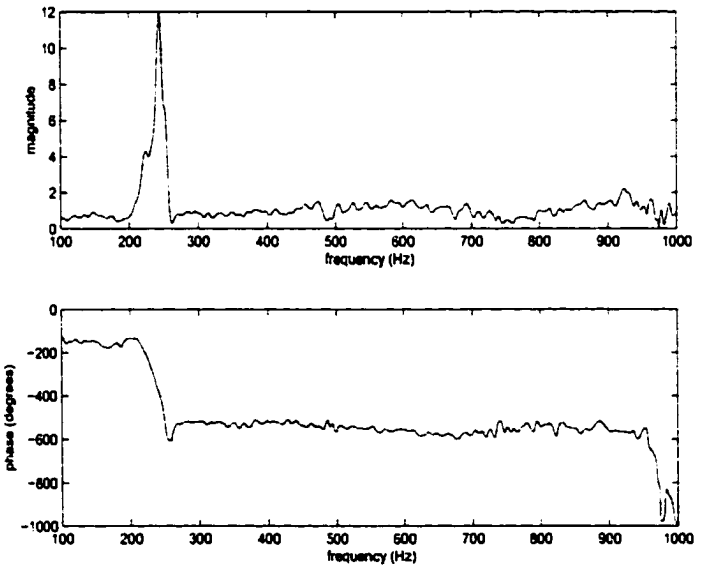

Figure 8.16: Experimental Frequency Response of Primary Control Speakers Channel $\hat{H}_{primary}(\omega)$.

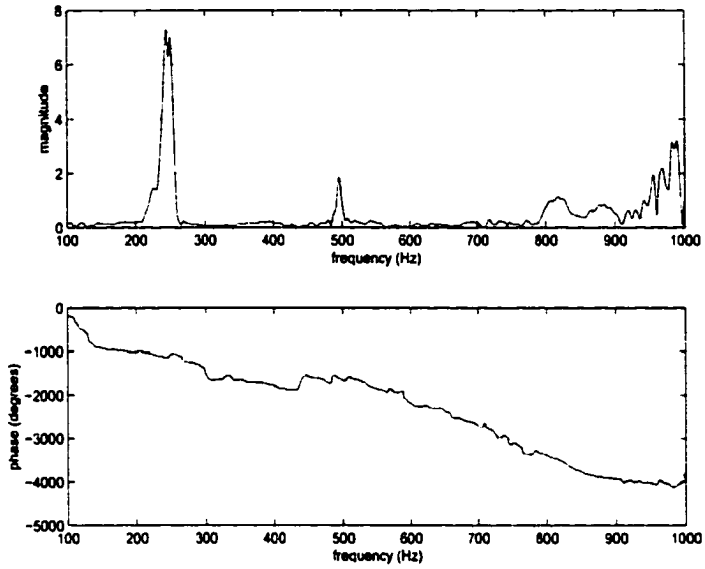

Figure 8.17: Experimental Frequency Response of Secondary Control Speakers Channel $\hat{H}_{secondary}(\omega)$.

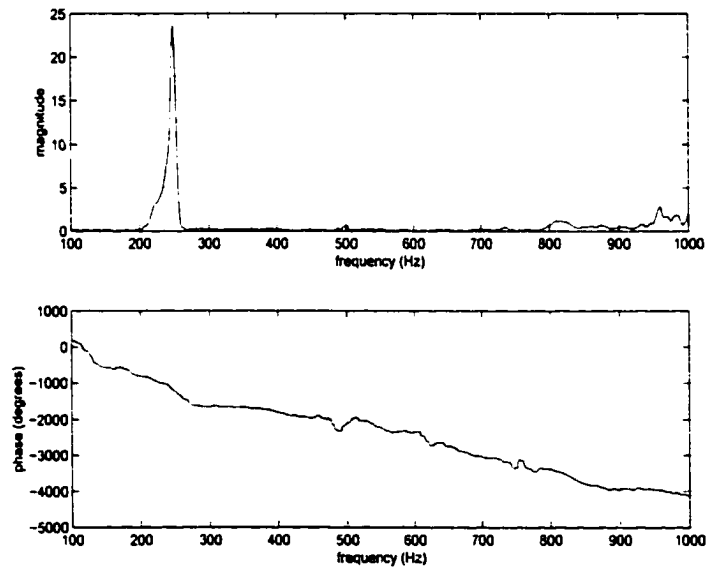

Figure 8.18: Experimental Frequency Response of Control Speakers Channel $\hat{H}_{primsec}(\omega)$.

The next step in the modeling process was to fit a rational transfer function to the frequency response data for each case (*fitsys* or *invfreqs*). All the data sets were SISO, thus the models were realized by a least square fit to the frequency data. A problem arose during the fitting process where the approximations to some of the data sets were unstable. To alleviate this problem, a weighting function was chosen $W(\omega)$ such that

$$W(\omega) = \begin{cases} 1 & 100\,Hz < w < 300\,Hz \\ 0 & elsewhere \end{cases}$$

to stress the relevance of the fitting in this working range and neglect the sudden changes in phase at high frequency. Therefore, each transfer function was an accurate description of the system in just the interval $100\,Hz < w < 300\,Hz$. The resulting model for $H_{primary}(s)$, plotted in Figure 8.19, was an 11^{th} order stable and proper transfer function with non-minimum-phase zeros:

$$H_{primary}(s) = \frac{-0.65404(s + 1.549 \times 10^4)(s^2 + 511.7s + 1.507 \times 10^6)}{(s + 9964)(s^2 + 119.8s + 2.056 \times 10^6}$$

$$\cdot\frac{(s^2 - 189.2s + 2.195 \times 10^6)(s^2 + 112.7s + 2.927 \times 10^6)(s^2 + 394.9s + 1.805 \times 10^7)}{(s^2 + 45.16s + 2.387 \times 10^6)(s^2 + 451.1s + 2.808 \times 10^6)(s^2 + 406.6s + 1.689 \times 10^7)}$$

$$\cdot\frac{(s^2 - 65.69s + 3.821 \times 10^7)}{(s^2 + 40.68s + 3.733 \times 10^7)} \tag{8.11}$$

The fitting of $\hat{H}_{secondary}(\omega)$ was more complicated, mainly due to time-lag presented in the frequency response. The final representation for $H_{secondary}(s)$, shown in Figure 8.20, was a strictly proper transfer function with 15 stable poles and 9 non-minimum phase zeros:

$$H_{secondary}(s) = \frac{-8.673246 \times 10^{18}(s + 2496)(s^2 - 0.1699s + 5.324 \times 10^5)}{(s + 870.3)(s^2 + 23.29s + 5.225 \times 10^5)(s^2 + 105.5s + 1.987 \times 10^6)}$$

$$\cdot\frac{(s^2 + 95.25s + 2.058 \times 10^6)(s^2 - 22.79s + 2.419 \times 10^6)(s^2 + 131.9s + 2.695 \times 10^6)}{(s^2 + 82.48s + 2.223 \times 10^6)(s^2 + 40.58s + 2.436 \times 10^6)(s^2 + 654.8s + 2.626 \times 10^6)}$$

$$\cdot \frac{1}{(s^2 + 56.49s + 2.658 \times 10^6)(s^2 + 16.18s + 1.304 \times 10^7)} \tag{8.12}$$

Finally, the model for the combined speakers response $\hat{H}_{primsec}(\omega)$ was obtained. The resulting approximation for $H_{primsec}(s)$, plotted in Figure 8.21, was a 14^{th} order stable and proper realization with non-minimum phase zeros:

$$H_{primsec}(s) = \frac{-0.54483(s^2 + 62.46s + 4.759 \times 10^5)(s^2 + 415.5s + 1.601 \times 10^6)}{(s^2 + 89.94s + 5.171 \times 10^5)(s^2 + 94.18s + 1.94 \times 10^6)}$$

$$\cdot \frac{(s^2 - 197.7s + 2.204 \times 10^6)(s^2 + 31.46s + 2.372 \times 10^6)(s^2 + 3.359s + 2.699 \times 10^6)}{(s^2 + 46.62s + 2.307 \times 10^6)(s^2 + 19.42s + 2.398 \times 10^6)(s^2 + 32.76s + 2.522 \times 10^6)}$$

$$\cdot \frac{(s^2 + 29.66s + 3.75 \times 10^6)(s^2 + 5.241s + 6.114 \times 10^6)}{(s^2 + 35.55s + 3.79 \times 10^6)(s^2 + 6.569s + 6.112 \times 10^6)} \tag{8.13}$$

8.3.3 Controller Synthesis

LQG and $\mathcal{H}_\infty$ Loop-Shaping design were applied to the combustor models: $H_{primary}(s)$, $H_{secondary}(s)$ and $H_{primsec}(s)$. From the description of the combustor model (7.10), the control formulation can be considered as an output disturbance attenuation problem. It is well known that the optimal controller tends to invert the dynamics of the plant, but the three models given in (8.11),(8.12) and (8.13) are non-minimum phase. In addition, in the case of $H_{secondary}(s)$ this transfer function is strictly proper. Consequently, it is expected that the controllers derived from LQG and $\mathcal{H}_\infty$ Loop-Shaping designs perform some kind of approximate inversion in a limited frequency range. However, special care was taken to obtain stable controllers for each design technique. As in the fuel modulation case, the synthesis of the model-based controllers was carried out by using the commands *lqr*, *kalman* and *ncfsyn* from MATLAB [28, 5].

The LQG controllers were designed based on the following design parameters: $Q = 1 \times 10^3$, $R = 1$, $Q_n = 10$ and $R_n = 10$. These set of parameters produced

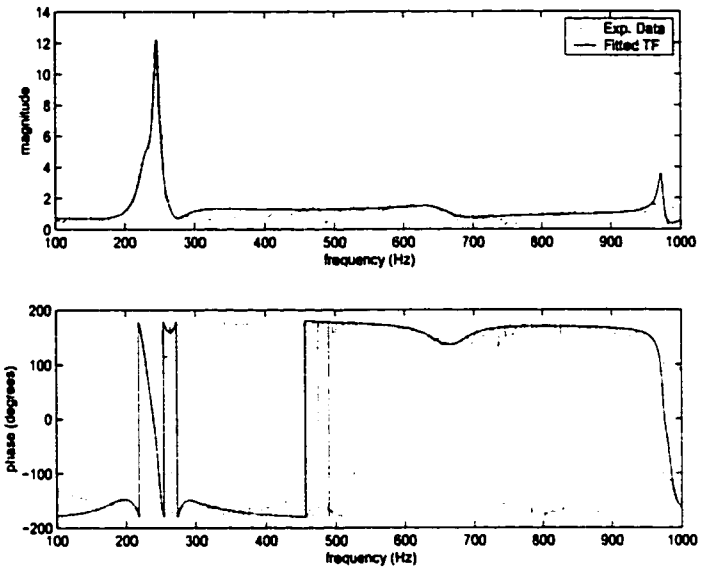

Figure 8.19: Comparison between Fitted Transfer Function $H_{primary}(s)$ and Experimental Data $\hat{H}_{primary}(\omega)$.

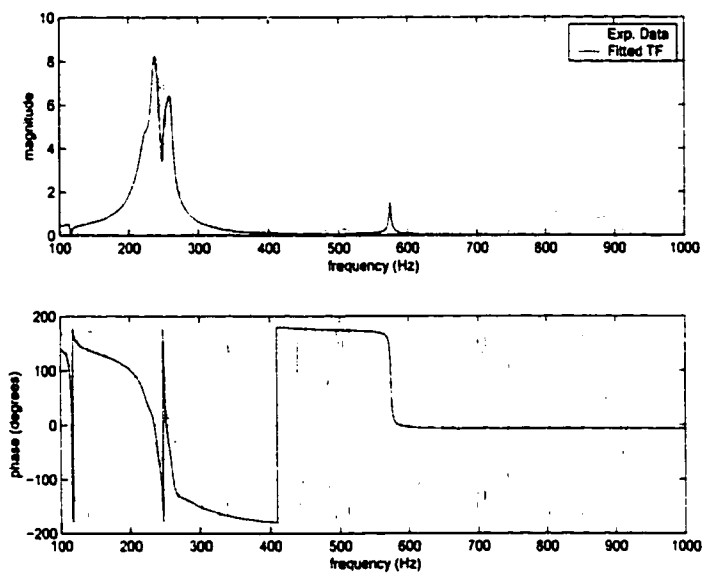

Figure 8.20: Comparison between Fitted Transfer Function $H_{secondary}(s)$ and Experimental Data $\hat{H}_{secondary}(\omega)$.

stable controllers for each model. The frequency responses of resulting controllers are plotted in Figure 8.22.

In the $\mathcal{H}_\infty$ Loop-Shaping design, the weighting function

$$W(s) = \frac{3947841.7604(s + 0.6283)}{(s + 314.2)(s^2 + 3016s + 6.317 \times 10^6)}$$

was used to stress the importance of the attenuation at the instability frequency 250Hz. Its frequency response is plotted in Figure 8.23. Now, the Bode plots of the resulting controllers are shown in Figure 8.24.

From the frequency responses of Figures 8.22 and 8.24, it is evident that the optimal controllers are doing approximate inversions of the corresponding plants, roughly in the frequency range 200 to 300Hz. Now, denote $K_{primary}$, $K_{secondary}$ and $K_{primsec}$ the controllers designed using the models $H_{primary}$, $H_{secondary}$ and $K_{primsec}$ respectively. Thus, the closed-loop transfer functions (cf. Figure 7.10) from w to p are given by

$$T_{p\&s} = \frac{H_{open-loop}}{1 + H_{primary}K_{primary} + H_{secondary}K_{secondary}} \tag{8.14}$$

$$T_{primsec} = \frac{H_{open-loop}}{1 + H_{primsec}K_{primsec}} \tag{8.15}$$

for separate and combined primary and secondary forcing respectively. In Figure 8.25, The frequency responses for these closed-loop transfer functions are shown for the LQG controllers. Similarly, the responses with the $\mathcal{H}_\infty$ Loop-Shaping controllers are presented in Figure 8.26. Note how the attenuation in the peak frequency are not substantial since the controllers are restricted to be stable.

On the other hand, in order to facilitate the controller implementation, the order of the controllers was limited to be 10^{th} order for all the strategies. For this purpose, balance truncation [80] was applied such that the shape of the frequency response

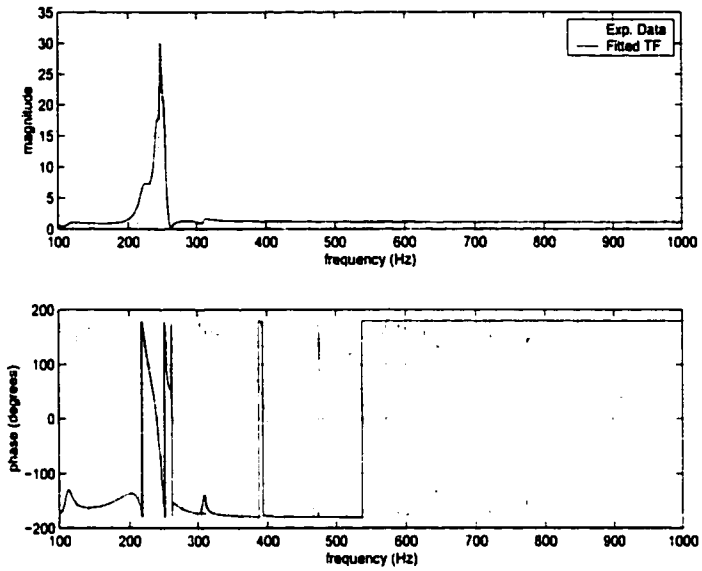

Figure 8.21: Comparison between Fitted Transfer Function $H_{primsec}(s)$ and Experimental Data $\hat{H}_{primsec}(\omega)$.

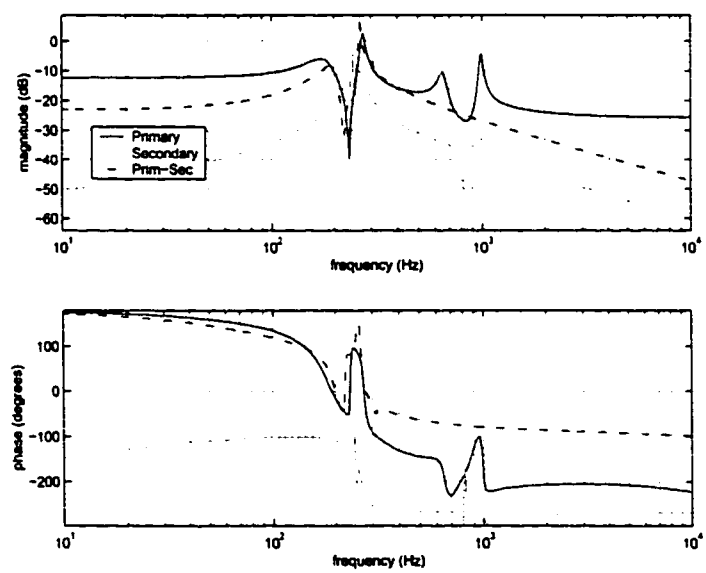

Figure 8.22: LQG Controllers Frequency Response.

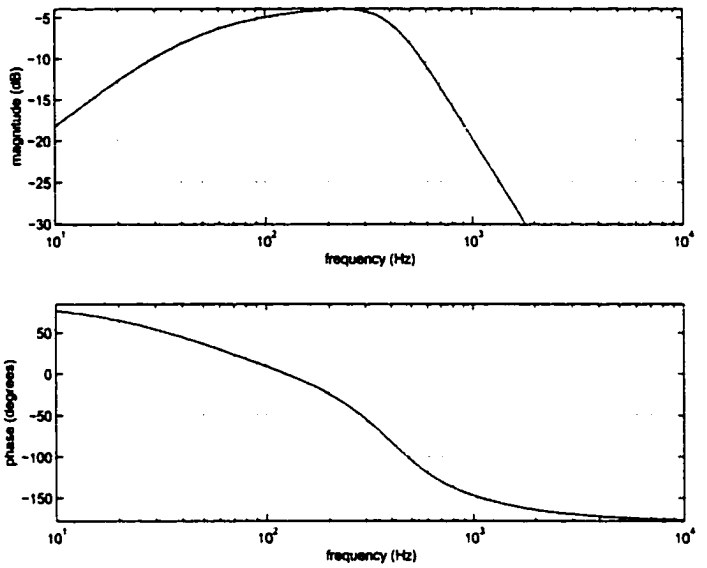

Figure 8.23: Weighting Function for $\mathcal{H}_\infty$ Loop-Shaping Design.

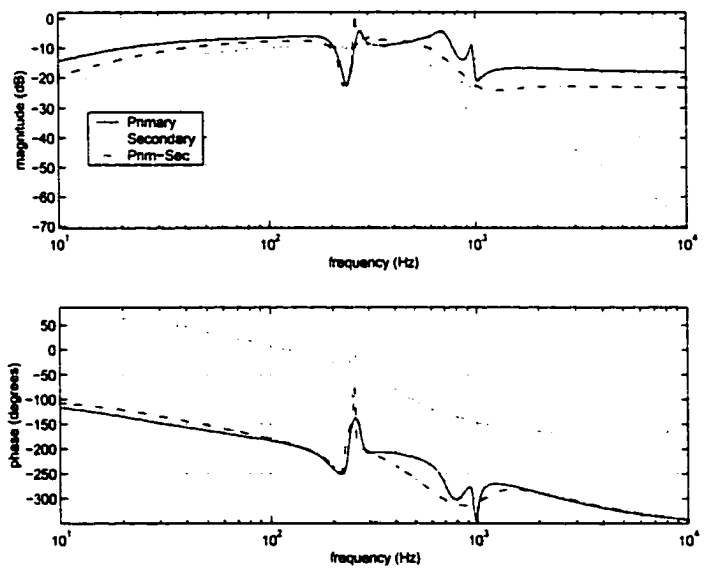

Figure 8.24: $\mathcal{H}_\infty$ Loop-Shaping Controllers Frequency Response.

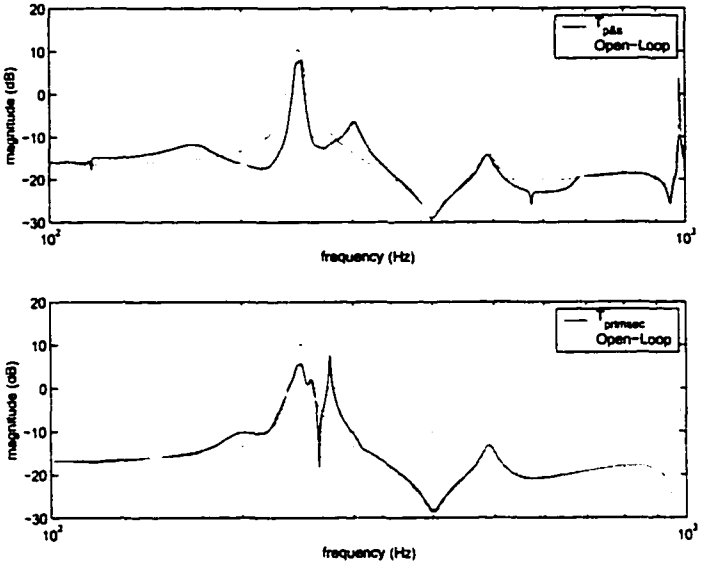

Figure 8.25: Closed Loop Transfer Functions for LQG Controllers.

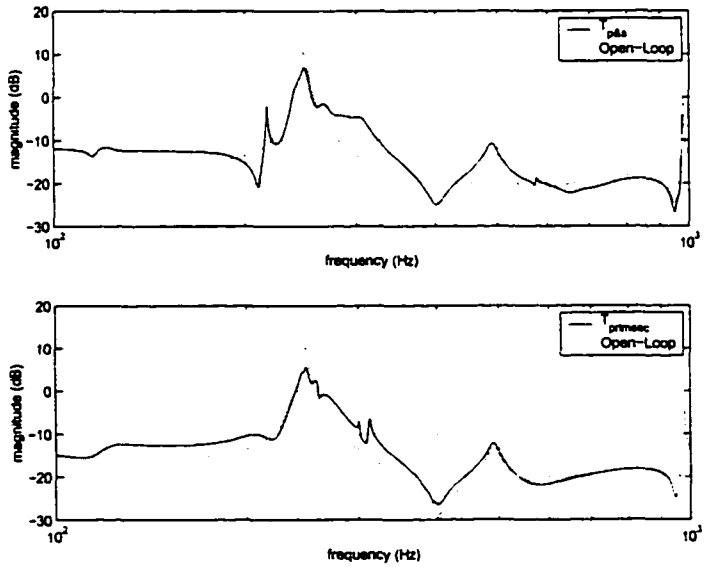

Figure 8.26: Closed Loop Transfer Functions for $\mathcal{H}_\infty$ Loop-Shaping Controllers.

was not significantly altered (*balreal* and *modred*). In addition, the continuous-time controllers were transformed to discrete by 'bilinear transformation' with 'pre-warping' at 250Hz and a sampling frequency of 10kHz (*c2d* command from *control* toolbox of MATLAB), and they were implemented by the dSPACE data-acquisition system.

8.3.4 Control Implementation

During the experimental testing of the control strategies, after active control was switched on the combustor was let reach a steady state response. The response was then visualized using a spectrum analyzer. The control was switched off and on again to check that the overall control effect could be repeated.

8.3.4.1 Phase Delay Control

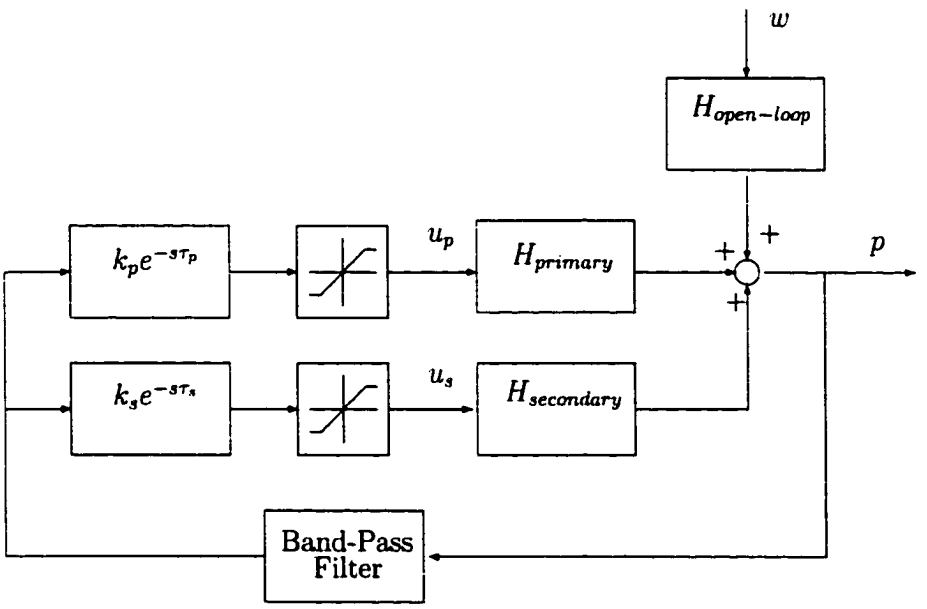

Figure 8.27: Simulation Block of Phase-Delay Control with Experimental Block.

In the experimental implementation of phase-delay control, a band-pass filter was used to reject noise coming from low and high frequency components. The computation of the band-pass filter was separated into a low-pass butterworth filter with cut-off frequency of 500Hz and a high-pass butterworth filter with cut-off frequency of 80Hz. Since these two cut-off frequencies are close to each other, there is some phase shift at the instability frequency ($\approx$ 250Hz) coming from the filtering process. In order to validate the accuracy of the experimental combustor model shown in Figure 7.10, simulation was performed to determine the effect of phase-delay control in the modeled pressure measurement. The simulation block diagram, presented in Figure 8.27, was implemented and numerically simulated in MATLAB/Simulink. To be able to compare the simulations with the experimental response, the same band-pass filter was used in the simulation control block. The simulation as well as the experimental testing was carried out by choosing independent delay factors for primary and secondary control channels as shown in Figure 8.27.

The relative phases and gains between the pressure oscillations and the primary, τ_p and k_p, and secondary, τ_s and k_s, air forcings were varied to find the optimum delays for maximum attenuation of the instability. Figures 8.28 and 8.29 show surface plots of the attenuation/amplification of the peak and power (evaluated in the interval 0-1kHz) of the pressure oscillations as functions of the forcing delays. The values in the plots are normalized by the maximum dB amplification. Thus, positive values represent amplification with a maximum value of 1 and negative values are indicative of attenuation of the instability. Control of the instability was seen to be less sensitive to secondary air forcing, and the majority of phases resulted in an amplification of the instability. The simulation of the experimental combustor model showed a great success in predicting the qualitative trend for

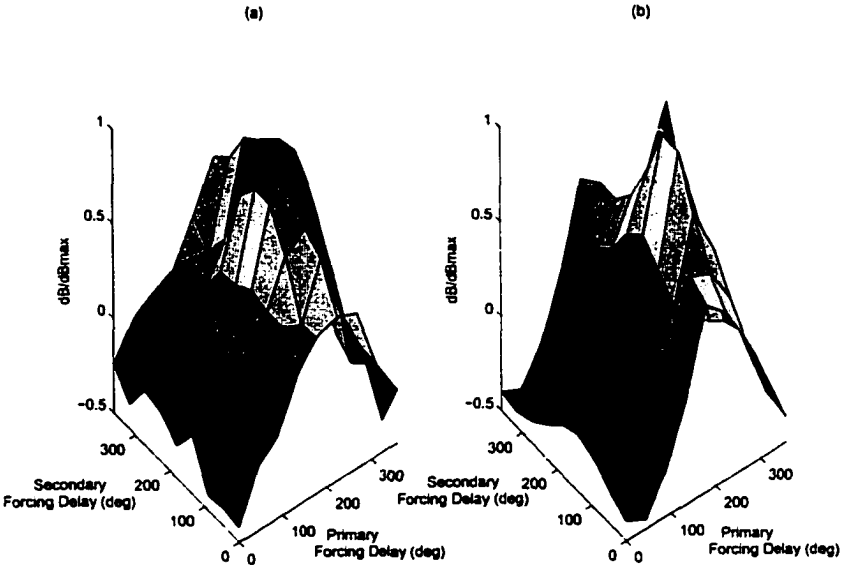

Figure 8.28: (a) Experimental and (b) Simulated Peak Amplification/Reduction as a Function of Primary and Secondary Forcing Delay.

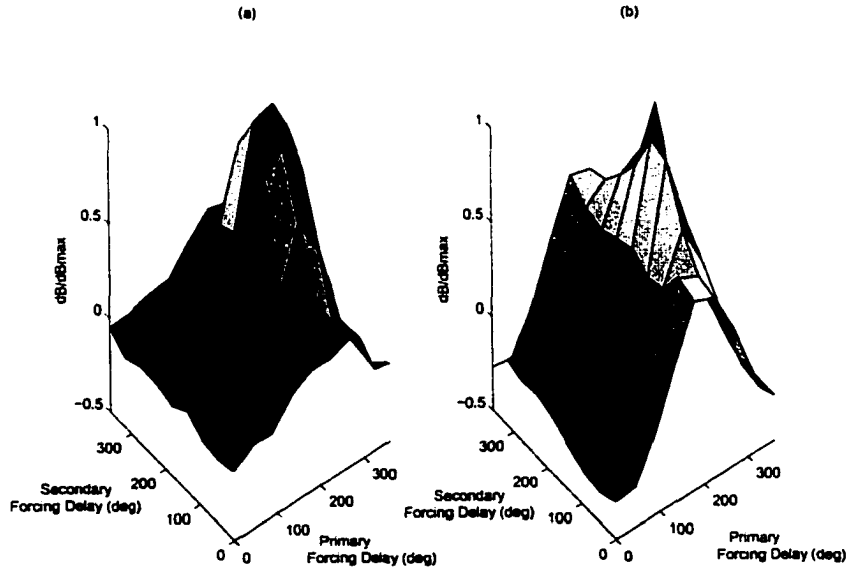

Figure 8.29: (a) Experimental and (b) Simulated Power Amplification/Reduction as a Function of Primary and Secondary Forcing Delay.

phase-delay control as seen in Figures 8.28 and 8.29. In both the simulations and experiments, the maximum reduction of the instability was found to occur at a primary and secondary phase delay of 0^o relative to the instability. Thus, the phase shift provided by the band-pass filter was optimum.

Figure 8.30 presents a plot of the experimental pressure spectra and time traces for the open-loop and optimal delay conditions. The open-loop condition corresponds to no acoustic forcing with the secondary fuel stream being modulated in an open-loop fashion at a fixed frequency of 400Hz. The fuel modulation remained constant at this condition during all tests and was not used to control the instability. Figure 8.30 shows that phase-delay control reduced both the peak and power of the pressure oscillations by approximately 3 dB.

8.3.4.2 Experimental Model-Based Controllers

In addition to the phase-delay control tests, controllers based on the LQG and $\mathcal{H}_\infty$ loop-shaping control techniques were tested. As mentioned earlier in the paper, system identification procedures were used to develop experimental models of the combustor for the cases of primary ($H_{primary}(s)$), secondary ($H_{secondary}(s)$) and combined primary/secondary ($H_{primsec}(s)$) forcing. For each of these three models, controllers were designed using the techniques outlined early. During the experimental testing, delays for the primary and secondary control signals were adjusted to obtain maximum attenuation of the pressure oscillations and compensate for any uncertainty coming from the modeling. The performance indices PA (7.10) and NRR (7.9) are employed to analyze the performance of each control strategy. Thus, the experimental response were recorded with and without control for 5s, i.e. 50,000 samples. However, the computation of the performance indices PA and

NRR required only 2^{15} samples (i.e. 3.3s). Note that this amount of samples is representative according with the time-scale associated with the instability. The command *psd* from the *signal processing* toolbox of MATLAB was used to compute the spectral density approximations. Table 8.4 summarizes the results obtained during experimental testing.

In the case of the LQG design, experiments showed that the best results were obtained when one controller designed from a combined primary/secondary model was used. Figure 8.31 shows the pressure spectra and time trace obtained from experiments when the LQG controller was applied. Both the fundamental (250Hz) and the second harmonic were reduced by about 10 dB and 14 dB respectively during the experimental test. The total power of the pressure oscillations was also reduced by 7 dB. This was substantially more than the phase-delay control, which at best resulted in 3 dB peak and power attenuation.

Control using the $\mathcal{H}_\infty$ loop-shaping technique was also implemented in the combustor. Using separate controllers for the primary and secondary air forcing, the experiments showed 11 dB peak attenuation and 8 dB power attenuation. The pressure data for this control case is shown in Figure 8.32. Note that applying control resulted in the peak instability being distributed between multiple frequencies all centered about the original instability frequency.

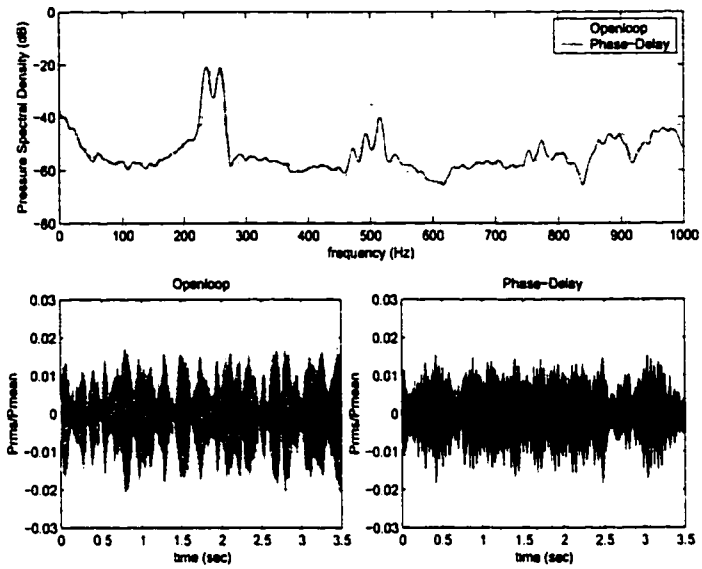

Figure 8.30: Pressure Spectra and Time Traces for Open-loop and Phase Delay Control (Primary Delay=0° and Secondary Delay=0°).

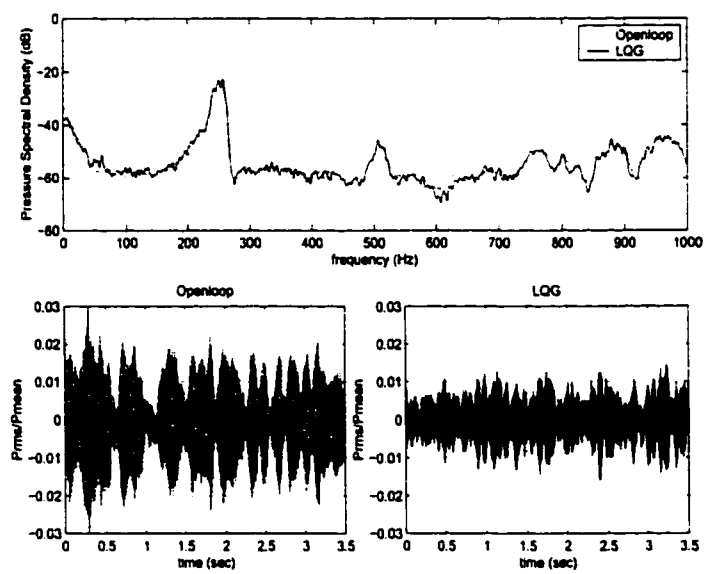

Figure 8.31: Experimental Pressure Spectra and Time Traces for Open-loop and LQG Control.

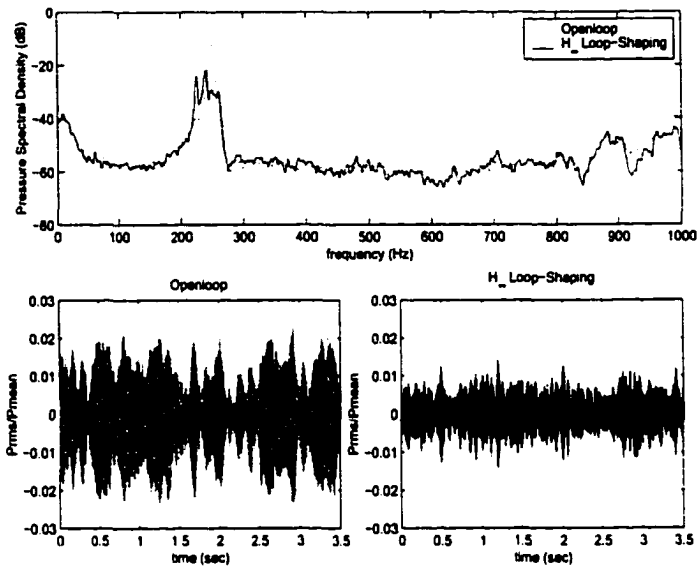

Figure 8.32: Experimental Pressure Spectra and Time Traces for Open-loop and $\mathcal{H}_\infty$ Loop-Shaping Control.

Table 8.4: Table Summary of Controllers Performance Using Acoustic Control.

Controller Type	**PA** (dB)	**NRR** (dB)
Phase-Delay	-3	-3
LQG	-10	-7
$\mathcal{H}_\infty$ Loop-Shaping	-11	-8

CHAPTER 9

ONGOING RESEARCH WORK

The recent advances in control of thermoacoustical instabilities in liquid fueled combustors are introduced in this chapter. The collaboration with researchers from the Mechanical Engineering Department at LSU has continued through the spring of 2001. Recently some alternative combustor configurations and fuel modulation schemes have been suggested.

9.1 Heat Release Visualizations

As explained in Chapter 8, four constant fuel sprays are alternated with four modulated at the burner. These fuel streams are then mixed with the primary and secondary swirling air flows to generate the reactants mixture going to the flame. In this configuration, the modulated fuel sprays are used for control purpose. One disadvantage of this configuration is that the modulated fuel is actually affected by the mixing process produced by the primary and secondary swirling air flows. Consequently the control modulation is damped in this process. Moreover, it was not known if the modulated fuel was reaching the zone of maximum heat release in the flame front.

In order to answer some of the previous questions and to have a better visualization of the flame dynamics, a new combustor chamber was machined. This new chamber has a square shape and provide lateral quartz windows for a complete visualization of the combustion process, see Figure 9.1. Therefore, advanced diagnostic

techniques to measure three-dimensional velocity profiles, such as PIV and PDPA, and heat release patterns, visualization of CH emissions, can be applied.

In early work by Allgood [1], he performed semi-quantitative measurements of the heat release by visualizing the CH chemiluminescent emissions at 430nm wavelength in the combustor. The images were acquired using a Princeton Instruments 512x512 ICCD camera with an Electrophysics UV lens and a 430nm bandpass filter (DIOP). A pressure transducer provided a measurement of the pressure fluctuations. He computed the spatial variations of the Rayleigh Integral, which is the integration over time of the product of the pressure and heat release fluctuations. Figure 9.2 shows the distribution of the Rayleigh Integral for an unstable condition of the combustor. Due to symmetry of the flame front, only one side (3in x 3in) of the combustion chamber is being shown. Locations having positive values (red) indicate that the pressure and heat release fluctuations are in phase and thus the instability is being amplified. Similarly, locations associated with negative values (blue) indicate regions of attenuation (out of phase). Thus from Figure 9.2, important conclusions can be drawn: amplification of the instability occurred along the centerline of the combustor where strong heat release fluctuations were present, damping of the instability occurred in the outer portions of the flame where the heat release oscillations were not as strong.

9.2 Modified Control Configuration

As a result, by these heat-release visualizations it is evident that the control fuel must reach this middle zone of the combustor in order to have a more efficient actuation. Moreover, this control fuel has to be applied in such a way that it can overcome the recirculation zone induced by the swirl dynamics and it can also

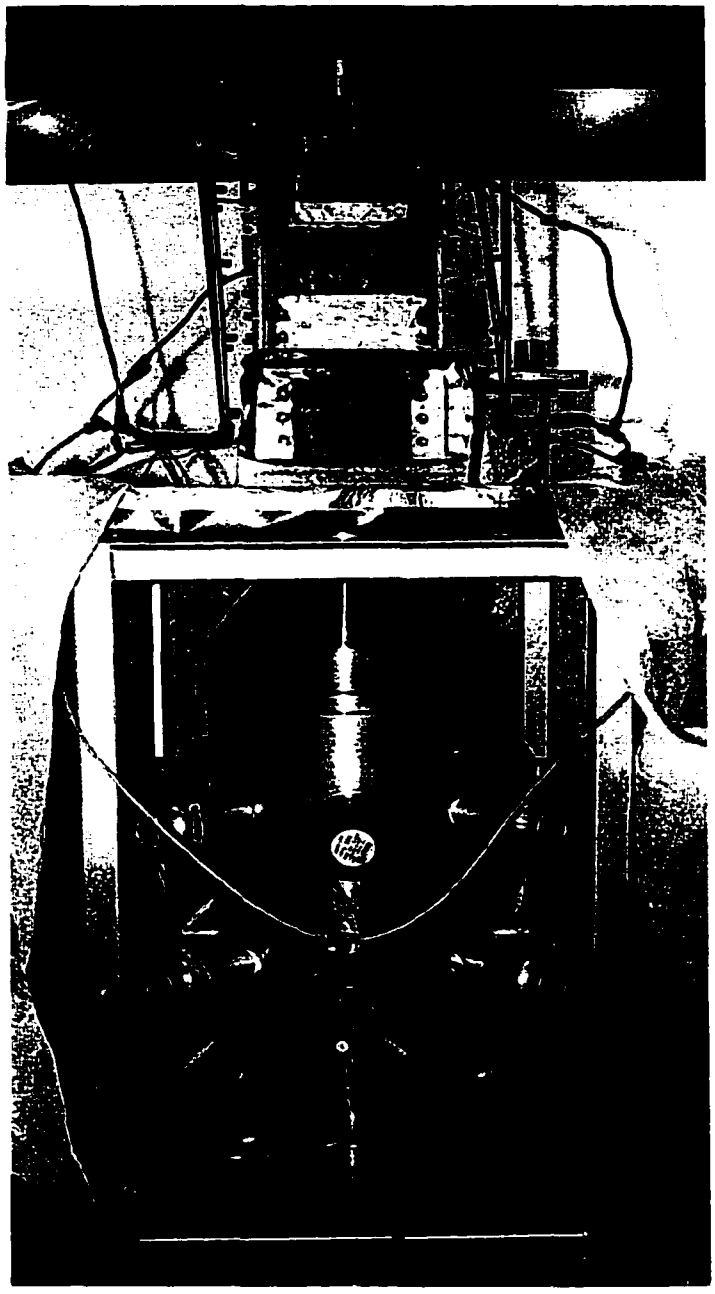

Figure 9.1: Test-Rig with Square Chamber, Mechanical Department at LSU.

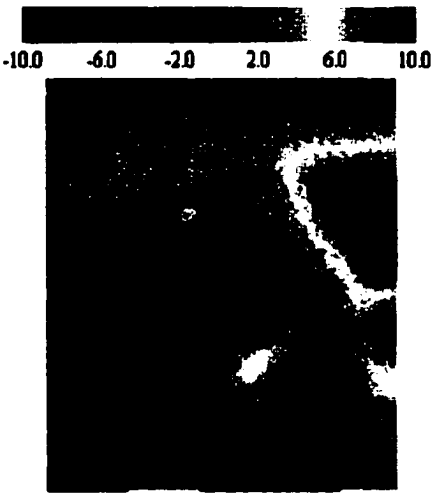

Figure 9.2: Rayleigh Index for Unstable Condition.

maintain its modulation properties. Therefore, parameters such as droplet size and fuel pressure must be chosen carefully. In this way, it was suggested to add an extra fuel line just for control purpose in the centerline of the combustor as shown in Figure 9.3. A fuel injector was used in order to modulate this fuel stream line. Thus a control nozzle was mounted on top of the swirl vanes corresponding to the primary air flow. Intuitively, the primary air-flow rate should have an important role in the effectiveness of the control, since higher or lower rates can rise or squeeze the flame shape respectively.

This modification was carried out and an initial study of active control with phase-delay control was performed. Thus, the control improvements with this new combustor setup could be judged. First, an operating condition that presented a clear instability was obtained. Table 9.1 shows the chosen operating condition. The instability frequency was located at 242Hz. In Figure 9.4, the frequency content of the pressure signal at this operating condition is shown. The baseline fuel-flow rate

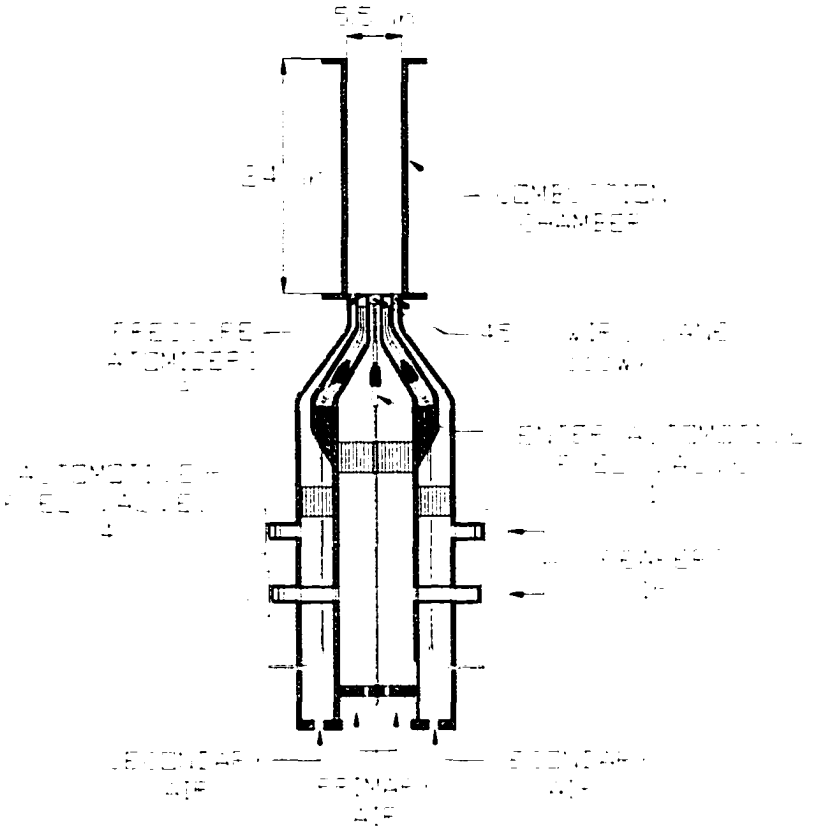

Figure 9.3: Experimental Test-Rig with New Control Configuration, Mechanical Department at LSU.

was set to 2.7gph, where 1.0gph was injected constantly and 1.7gph were modulated at 600Hz (much larger than the instability frequency).

Phase-delay control was then implemented. The structure of this simple controller was given by

$$K(s) = e^{-\tau s} H_{band-pass}(s) \tag{9.1}$$

where $H_{band-pass}$ is a butterworth band-pass filter with passing band 80Hz to 500Hz. The delay parameter, τ, was tuned manually to obtain the largest suppression in the instability. The signal of the controller was sent to a sign-type of nonlinearity

Table 9.1: Operating Condition for Initial Study (New Control Setup).

Fuel-Flow Rate				
Baseline	Control	$Q_{primary}$	$Q_{secondary}$	Pressure
2.7gph	0.2gph	24cfm	157cfm	atmospheric

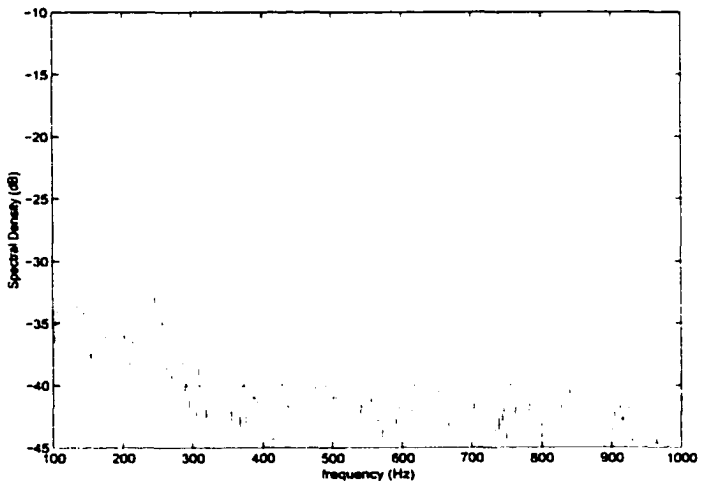

Figure 9.4: Spectra of Pressure Measurement without Control.

in order to provide a discrete signal to the control fuel injector. The optimum delay was found at 2ms. The pressure measurement was recorded with and without control. During testing, active control was switched on and off for a few times in order to check that the overall attenuation effect could be repeated. 2^{15} samples at 10kHz were acquired with and without control to judge the response. Active control produced a peak attenuation (PA) of 13.21dB and a noise reduction (NRR) of 5.80dB with just 7% of control fuel. The response with and without control is shown in Figure 9.5.

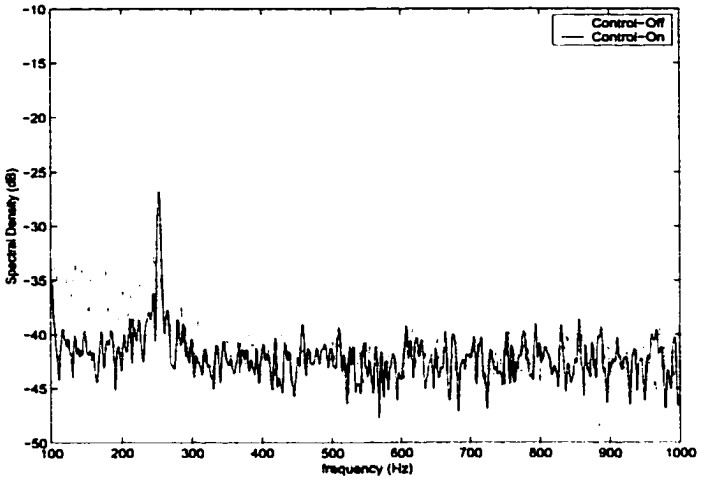

Figure 9.5: Pressure Measurement with Phase-Delay Control.

During the experimental test, it was noticed that the primary air-flow rate, $Q_{primary}$, had a big impact in the combustor response with control. If $Q_{primary}$ was changed in a span of 2cfm down the operating condition, the control effectiveness was drastically diminished. This behavior corroborated the previous comment about the effect of the primary air-flow rate in the control behavior.

The results obtained with this new setup are very encouraging and proved that with just a small amount of control fuel the instability could be suppressed. As a result, the location of the modulated fuel stream is a critical factor in the control scheme. Now, a question naturally arises, could model-based control techniques improve the performance of phase-delay control in this new setup ? The question has not been answered yet, so this is the objective of future research work in the Mechanical Department at LSU. Moreover, automotive fuel injectors have been used for fuel modulation so far. Thus a continuous variation of the control fuel has not been directly investigated. So the response of model-based controllers with a proportional fuel valve as actuator is also an open question. However the cost of

these fuel valves makes them a rather difficult option for control. Nevertheless, this option is actively pursued at the Mechanical Department.

9.3 New Research Trends

Now, part of the fuel stream is modulated by four fuel injectors at the burner. This modulation could be set fixed or variable according with the control scheme. However, in the new control setup, the control fuel was injected only by the centerline fuel injector. So, during experiments the four fuel injectors were modulated constantly at 600Hz. Although, this frequency is larger than the instability frequency ($\approx$ 242Hz), it is not possible to establish if this modulation can affect directly or indirectly the control stream. Consequently, it was suggested to by-pass these injectors. Thus, the eight fuel streams in the burner could run constantly without modulation.

So far only linear identification techniques have been used during modeling. Consequently, the identification of the nonlinear interactions in the system come as a natural extension of our previous work. Thus, a better understanding of the combustor dynamics could be achieved and even nonlinear control strategies could be suggested. The basic idea in this process is to be able to record measurements of the instability mechanisms such as pressure and heat release for stable and unstable conditions. Obviously, these two conditions should correspond to the same operating point (air/fuel ratio) of the chamber. For this purpose, it was suggested to change the boundary condition at the exit of the chamber. A stainless steel plate with a smaller diameter than the exit area was mounted on top of the combustor chamber to partially reflect the acoustic field and then modify the exit boundary condition. This modification was tested in the experimental rig with excellent results. An operating

condition of the chamber was selected such that a clear instability was presented. Thus, the fuel stream was set to 3.0gph, $Q_{primary}$ = 20cfm and $Q_{secondary}$ = 140cfm. The instability was presented at $\approx$ 240Hz. So, without the exit plate an unstable condition of the chamber was seen. Once the plate was mounted the strong pressure oscillations completely disappeared. The pressure measurement was recorded for these two conditions. 2^{16} samples at 20kHz were acquired by the DSP board. Figure 9.6 presents the pressure spectra for both conditions. It is clear how the exit plate completely attenuate the pressure oscillations. Now, the next step in this work is to propose the structure of a nonlinear combustor model. Moreover, an identification scheme based on the stable and unstable measurements must be carefully planned. These two issues are currently being investigated in detail.

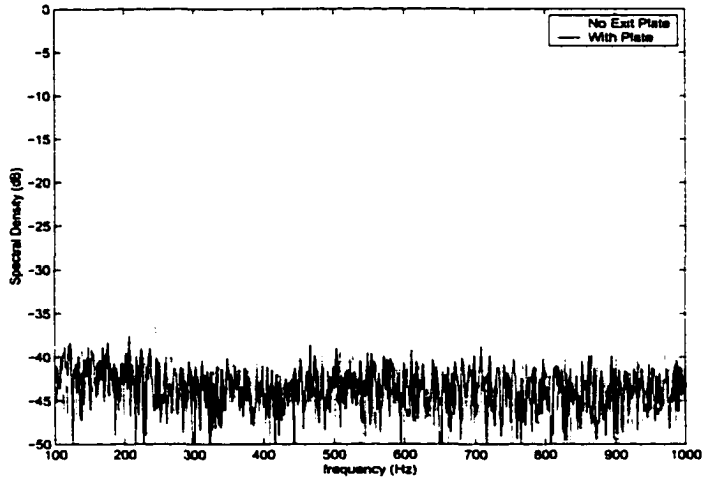

Figure 9.6: Spectra of Pressure Measurement with and without Exit Plate.

CHAPTER 10

$\mathcal{H}_\infty$ STRONG STABILIZATION

An alternative design algorithm for the $\mathcal{H}_\infty$ Strong Stabilization control problem is introduced in this chapter. The proposed approach pursues to overcome the conservativeness of previous formulations presented in literature. Numerical examples are given to show the effectiveness of the design algorithm.

10.1 Motivation

Most standard optimal control problems are formulated by minimizing some performance indices or cost functions while keeping the stability of the closed-loop systems. Little attention has been paid towards the stability of the resulting controllers themselves. This is at least partially because the stability constraints on the controllers are very hard to reflect on the cost functions. On the other hand, the issue of controller stability is of a big concern in the real world implementations of optimal control since unstable controllers are highly sensitive, and in case of sensor-faults and plant uncertainties/nonlinearities, the response is unpredictable.

It is known from [74, 77] that a necessary and sufficient condition for the existence of a stable stabilizing controller for a given plant is the so-called parity interlacing property (p.i.p.). Consequently, a rational plant P is strongly stabilizable (i.e., stabilizable by a stable controller) if and only if its number of unstable poles (counted according with their McMillan degrees) between every pair of right-half plane blocking zeros is even.

Since the $\mathcal{H}_\infty$ controller is in general not unique, it is reasonable to expect that even if the $\mathcal{H}_\infty$ central controller is unstable, there might still be a stable controller that could satisfy the $\mathcal{H}_\infty$ norm bound if the p.i.p. condition is satisfied. In [13, 78, 79], an approach for designing such high order stable $\mathcal{H}_\infty$ controller has been suggested based on the parameterization of all suboptimal $\mathcal{H}_\infty$ controllers. This approach converts conservatively the stable $\mathcal{H}_\infty$ controller design problem into another 2-block standard $\mathcal{H}_\infty$ problem. Hence, the existence of a solution to the two-block $\mathcal{H}_\infty$ problem assures the existence of a strong stabilizing $\mathcal{H}_\infty$ controller. However, there is no guarantee in general for the existence of a solution to this alternative 2-block problem because of the significant conservativeness introduced in this conversion process. In addition, the order of the resulting controller may be twice as high as the order of the central controller.

10.2 $\mathcal{H}_\infty$ Suboptimal Parameterization

Assume that the generalized plant G is given by:

$$G = \left[\begin{array}{c|cc} A & B_1 & B_2 \\ \hline C_1 & D_{11} & D_{12} \\ C_2 & D_{21} & D_{22} \end{array}\right] \tag{10.1}$$

with some suitable assumptions. The following are two standard $\mathcal{H}_\infty$ control problems:

- Optimal $\mathcal{H}_\infty$ control: *find all internally stabilizing controllers* $K(s)$ *such that* $\|\mathcal{F}_l(G,K)\|_\infty$ *is minimized.*
- Suboptimal $\mathcal{H}_\infty$ control: *given* $\gamma > 0$, *find all internally stabilizing controllers* $K(s)$, *if there is any, such that* $\|\mathcal{F}_l(G,K)\|_\infty < \gamma$.

It should be noted that the optimal $\mathcal{H}_\infty$ controller is not unique for MIMO systems. Obviously, this is also true for the suboptimal case. In general, solving the optimal $\mathcal{H}_\infty$ control problem is numerically and theoretically complicated. Thus from now on, the focus will be on the $\mathcal{H}_\infty$ suboptimal problem ($\gamma > \gamma_{opt}$). Moreover, it has been proved by Doyle et al. [21], that all controllers $K(s)$ satisfying the suboptimal restriction can be parameterized by $Q \in \mathcal{RH}_\infty$, $\|Q\|_\infty < \gamma$ such that $K = \mathcal{F}_l(M_\infty, Q)$

$$M_\infty = \left[\begin{array}{c|cc} \hat{A} & \hat{B}_1 & \hat{B}_2 \\ \hline \hat{C}_1 & \hat{D}_{11} & \hat{D}_{12} \\ \hat{C}_2 & \hat{D}_{21} & \hat{D}_{22} \end{array}\right] = \left[\begin{array}{cc} M_{11} & M_{12} \\ M_{21} & M_{22} \end{array}\right] \tag{10.2}$$

where M_∞ is constructed from the solutions of two Riccati equations [21, 80]. In the case of $Q = 0$, the solution, $K = M_{11}$, is called the *central controller*. Note that the central controller could be unstable since there is no guarantee that M_∞ is itself stable even though the closed-loop stability is maintained.

10.3 $\mathcal{H}_\infty$ Strong Stabilization Problem

For practical considerations, it is always desirable to have stable controllers in closed-loop control. Hence, a *strong stabilization* problem is to design a controller $K \in \mathcal{RH}_\infty$ such that the closed-loop is internally stabilized and some performance specifications are satisfied. Consequently, combining the $\mathcal{H}_\infty$ suboptimal design with the *strong stabilization* requirement the following problem is formulated

- $\mathcal{H}_\infty$ Strong Stabilization: *given* $\gamma > 0$, *find a stabilizing controller* $K \in \mathcal{RH}_\infty$ *such that* $\|\mathcal{F}_l(G, K)\|_\infty < \gamma$.

It can be seen from the parameterization of the all suboptimal $\mathcal{H}_\infty$ controllers that to find a stable stabilizing K, it is enough to find a $Q \in \mathcal{RH}_\infty$ with $\|Q\|_\infty < \gamma$ such that Q stabilizes M_∞. It is not hard to see that this can be achieved if and only if Q stabilizes M_{22}. This gives the next result [78, 79].

Lemma 10.1 *Assume that a solution to the suboptimal $\mathcal{H}_\infty$ control problem exists for a given $\gamma > 0$, i.e. $\exists M_\infty$ such that $\|\mathcal{F}_l(G,K)\|_\infty < \gamma$ and $K = \mathcal{F}_l(M_\infty, Q)$ where $Q \in \mathcal{RH}_\infty$ and $\|Q\|_\infty < \gamma$. Then, the $\mathcal{H}_\infty$ Strong Stabilization is solvable if and only if $\exists Q$, with $\|Q\|_\infty < \gamma$, such that*

$$\left(\hat{M} - Q\hat{N}\right)^{-1} \in \mathcal{RH}_\infty \tag{10.3}$$

where $\hat{N}$ and $\hat{M}$ are coprime factorization factors of M_{22}, $M_{22} = \hat{N}\hat{M}^{-1}$.

This condition (10.3) is further relaxed in [78, 79] by using small gain condition: condition (10.3) is guaranteed if $\|\hat{M} - I - Q\hat{N}\|_\infty < 1$ since $\hat{M} - Q\hat{N} \in \mathcal{RH}_\infty$. In summary, the $\mathcal{H}_\infty$ strong stabilization conditions in Lemma 10.1 can be conservatively guaranteed by the following two $\mathcal{H}_\infty$ norm conditions:

$$\begin{aligned} \|\hat{M} - I - Q\hat{N}\|_\infty &< 1 \\ \|\frac{1}{\gamma}Q\|_\infty &< 1 \end{aligned} \tag{10.4}$$

The above problem of finding a Q to satisfy both inequalities is known as a *two-disk problem* which is usually very difficult to solve. A standard technique is to combine the two inequalities into one so that a *two-block* $\mathcal{H}_\infty$ problem can be obtained:

$$\left\| [\hat{M} - I \quad 0] + Q[-\hat{N} \quad \frac{1}{\gamma} I] \right\|_\infty < 1 \tag{10.5}$$

Unfortunately, relaxing condition (10.3) using small gain condition and changing a two-disk problem into a two block problem can introduce significant conservativeness

into the solution and the opportunity to obtain Q for a given $\gamma > 0$ may be diminished. The purpose of this Chapter is to propose an alternative characterization so that some conservativeness can be alleviated.

Remark 10.1 *It should be noted that even if the Q obtained from minimizing the left-hand side of (10.5) does not satisfy the inequality (10.5), it does not imply that the resulting controller K obtained by substituting this Q is not stable or the closed-loop norm is not satisfied since condition (10.5) is not a necessary and sufficient condition. Hence, it is always important to check the conditions in Lemma 10.1 directly even though (10.5) may not be fulfilled.*

10.4 Stable Controller Design Algorithm

It is critical to note that the stability condition of the controller imposed in Lemma 10.1 can take some alternative form. Let W be any suitably dimensioned transfer matrix such that $W, W^{-1} \in \mathcal{RH}_\infty$. Then it is clear that

$$\left(\hat{M} - Q\hat{N}\right)^{-1} \in \mathcal{RH}_\infty \quad \Leftrightarrow \quad \left[(\hat{M} - Q\hat{N})W\right]^{-1} \in \mathcal{RH}_\infty \tag{10.6}$$

The following key result follows immediately.

Lemma 10.2 *There is a $Q \in \mathcal{RH}_\infty$ with $\|Q\|_\infty < \gamma$ such that $\left(\hat{M} - Q\hat{N}\right)^{-1} \in \mathcal{RH}_\infty$ if and only if there are a $W \in \mathcal{RH}_\infty$ with $W^{-1} \in \mathcal{RH}_\infty$ and a Q with $\|Q\|_\infty < \gamma$ such that*

$$\|(\hat{M} - Q\hat{N})W - I\|_\infty < 1.$$

Now the main results of this Chapter follow immediately from Lemma 10.1 and Lemma 10.2.

Theorem 10.3 *Suppose that there exist a $W(s)$ with $W, W^{-1} \in \mathcal{RH}_\infty$ and a $Q(s) \in \mathcal{RH}_\infty$ such that*

$$\|[\hat{M}W - I \quad 0] + Q[-\hat{N}W \quad 1/\gamma I]\|_\infty < 1 \tag{10.7}$$

Then the resulting suboptimal controller $K = \mathcal{F}_l(M_\infty, Q)$ *is stable and satisfies* $\|\mathcal{F}_l(G,K)\|_\infty < \gamma$.

It is important to emphasize that the selection of the weighting function $W(s)$ is not a trivial task and plays a critical role in the solvability of (10.7). So, the question now is how to select a biproper $W(s)$. The following design procedure presents an intuitive way of obtaining $W(s)$ based on an *inner-outer* factorization.

$\mathcal{H}_\infty$ Strong Stability Design Method:

1. Select $\gamma > \gamma_{opt}$ and obtain the parameterization of all suboptimal controllers.

2. Solve the $\mathcal{H}_\infty$ optimization problem

$$\min_{Q \in \mathcal{RH}_\infty} \left\| [\hat{M} - I \quad 0] + Q[-\hat{N} \quad \frac{1}{\gamma} I] \right\|_\infty \tag{10.8}$$

   where $M_{22} = \hat{N}\hat{M}^{-1}$.

3. Construct the controller $K = \mathcal{F}_l(M_\infty, Q)$ and $T_{zw} = \mathcal{F}_l(G,K)$. Next, check if $K \in \mathcal{RH}_\infty$ and $\|T_{zw}\|_\infty < \gamma$

   (a) **YES**: $\mathcal{H}_\infty$ Strong Stability Problem is solved.

   (b) **NO**: continue

4. Use the Q obtained through solving (10.8) to compute an inner-outer factorization of

$$\hat{M} - Q\hat{N} = UV^{-1} \tag{10.9}$$

   where U is inner and V is outer, i.e. $V, V^{-1} \in \mathcal{RH}_\infty$. (See [80] for inner-outer factorization formulas.)

5. Use $W = V$ to solve the optimization problem

$$\min_{Q \in \mathcal{RH}_\infty} \left\| [\hat{M}W - I \quad 0] + Q[-\hat{N}W \quad \frac{1}{\gamma} I] \right\|_\infty \tag{10.10}$$

6. Check the controller stability and $\mathcal{H}_\infty$ closed-loop performance. If both are satisfied:

   (a) **YES**: stop, the $\mathcal{H}_\infty$ Strong Stability Problem is solved.

   (b) **NO**: use the new Q to compute (10.9) and solve again (10.10) or stop and adjust γ.

Note that if the order of the generalized plant $G(s)$ is n, then the resulting controller by the preceding method will be $2n + order(W(s))$. But, the order of $W(s)$ will be related to the number of iterations needed to satisfy the requirements. Consequently, it is not recommendable to run the algorithm for more than 2 iterations.

On the other hand, once the $\mathcal{H}_\infty$ Strong Stability condition is satisfied, the controller could be reduced by some model-reduction technique. However, the reduced controller must always be stable and maintain the closed-loop performance.

Remark 10.2 *The weighting function W selected here is by no means the best. It is quite possible that a different selection of $W(s)$ may reduce the conservativeness even further for specific problems.*

10.5 Controller Order Reduction

Since the order of the stable controller obtained by the proposed algorithm can be much higher than the order of the generalized plant, the order of the controller could be a major concern in any practical implementation. We now propose a two-stage controller reduction algorithm:

1. Given $Q \in \mathcal{RH}_\infty$, obtain $\hat{Q}$ such that

   - $order(\hat{Q}) < order(Q)$,
   - $\|\hat{Q}\|_\infty < \gamma$ and

- $\mathcal{F}_l\left(M_\infty, \hat{Q}\right) \in \mathcal{RH}_\infty$.

2. Given $K = \mathcal{F}_l\left(M_\infty, \hat{Q}\right)$, obtain $\hat{K} \in \mathcal{RH}_\infty$ such that

   - $order(\hat{K}) < order(K)$ and
   - $\|\mathcal{F}_l(G, K)\|_\infty < \gamma$.

The algorithm presented above pursues first, to obtain the lowest order Q such that the controller stability and closed-loop performance are jointly satisfied, and second, to reduce the order of the resulting overall controller while keeping the attained performance. It was observed that the controller could be reduced more with the preceding algorithm than trying to attack the problem with the overall controller $K_0 = \mathcal{F}_l(M_\infty, Q)$. The first step of the reduction algorithm is computed based on the next theorem.

Theorem 10.4 *Suppose that $Q \in \mathcal{RH}_\infty$ solves the $\mathcal{H}_\infty$ Strong Stability Problem and $\hat{Q} \in \mathcal{RH}_\infty$ is a lower order model. Let*

$$\Delta := \hat{Q} - Q, \quad W_r := \hat{N}\left(\hat{M} - Q\hat{N}\right)^{-1}$$

Then the controller $K = \mathcal{F}_l\left(M_\infty, \hat{Q}\right)$ is stable and the closed-loop performance is maintained if

$$\|(\hat{Q} - Q)W_r\|_\infty < 1 \quad and \quad \|\frac{1}{\gamma}\hat{Q}\|_\infty < 1 \tag{10.11}$$

where $\hat{N}, \hat{M}$ is a right coprime factorization of M_{22}, i.e. $M_{22} = \hat{N}\hat{M}^{-1}$.

Proof: Since

$$\hat{M} - \hat{Q}\hat{N} = \hat{M} - Q\hat{N} - \Delta\hat{N} = \left(I - \Delta\hat{N}(\hat{M} - Q\hat{N})^{-1}\right)(\hat{M} - Q\hat{N})$$

by 'Small Gain' theorem, the controller is stable if $\|\Delta W_r\|_\infty < 1$. The norm condition comes from the standard $\mathcal{H}_\infty$ parameterization.

□

Thus, the first step in the controller reduction is performed by *Weighted Balance Truncation* [80], limiting the order of $\hat{Q}$ to satisfy (10.11). Secondly, the controller is further reduced to $\hat{K}$ while maintaining closed-loop performance and controller stability by the *Block Balanced Truncating Algorithm* [75] (or the structured truncation approach in [12]).

10.6 Numerical Examples

10.6.1 Example 1

In order to judge the possible improvements achieved with this proposed algorithm, the benchmark example used in [79] was examined. The generalized plant is described by:

$$\begin{aligned} z_1 &= \frac{0.03s^7 + 0.008s^6 + 0.19s^5 + 0.037s^4 + 0.36s^3 + 0.05s^2 + 0.18s + 0.015}{s^8 + 0.161s^7 + 6s^6 + 0.582s^5 + 9.984s^4 + 0.407s^3 + 3.9822s^2} \cdot (w_1 + u) \\ z_2 &= \beta u \\ y &= w_2 + \frac{0.0064s^5 + 0.0024s^4 + 0.071s^3 + s^2 + 0.1045s + 1}{s^8 + 0.161s^7 + 6s^6 + 0.582s^5 + 9.984s^4 + 0.407s^3 + 3.982s^2} \cdot (w_1 + u) \end{aligned} \tag{10.12}$$

where the parameter $\beta > 0$ was introduced to include some penalty on the control signal. The generalized plant is nonminimum-phase and it has a double pole at the origin, but it satisfies the p.i.p. condition, so it could be strongly stabilized. Hence, the solutions with and without weighting function were evaluated with just one iteration in the new algorithm. The resulting controllers were reduced by the two-stage algorithm outlined in the last section. The controller parameterization M_∞ was of 8^{th} order. For the no weighting-case, the parameter Q was of 8^{th} order also. The weighting W was always obtained of 8^{th} order for all $\beta's$. Therefore, the resulting controller obtained through solving (10.10) was of 24^{th} order.

Table 10.1: Example 1, Computational Results.

β	**Weight**	γ	**order** $\mathcal{F}_l(M_\infty, Q)$	$\|T_{zw}\|_\infty$	**order** $\hat{Q}$	**order** $\hat{K}$	$\|T_{zw}\|_\infty$
0.1	YES	0.2372	24	0.23719	2	10	0.2371
($\gamma_{opt} = 0.2324$)	NO	0.2451	16	0.24490	2	10	0.2449
0.01	YES	0.1511	24	0.15105	2	8	0.1511
($\gamma_{opt} = 0.1415$)	NO	0.1801	16	0.17820	2	8	0.1782
0.001	YES	0.1321	24	0.13205	2	10	0.1320
($\gamma_{opt} = 0.1223$)	NO	0.1731	16	0.17310	2	8	0.1730

Note that for $\beta = 0.1$ and $\gamma = 0.2561$ ($\gamma_{opt} = 0.2324$) the resulting central controller from the direct $\mathcal{H}_\infty$ optimization is stable. This means that it is possible to obtain a stable controller if the closed-loop performance requirement is relaxed. However, for the cases $\beta = 0.01$ and 0.001 there was no given $\gamma > 0$ to solve the suboptimal $\mathcal{H}_\infty$ problem that could lead to a stable central controller.

It is shown clearly from Table 9.1 that the addition of a weighting function improved greatly the controller design and much less conservative results were obtained. So, there is no need to sacrifice much performance for using stable controllers. In the overall, an improvement ranging from 62% to 80% was observed. On the other hand, note that the controller reduction strategy produced pretty good results. The final controllers had an order comparable with the no-weighting case. So, there was also no need to increase the controller order to improve performance.

Remark 10.3 *The generalized plant given in (10.12) was deduced directly from [7], since the description given in [79] is not correct.*

10.6.2 Example 2

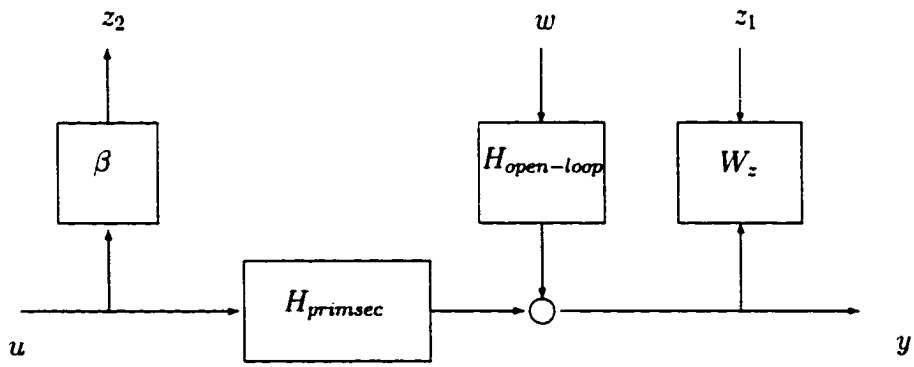

Figure 10.1: Combustor $\mathcal{H}_\infty$ Synthesis Block Diagram

The next example was taken from the description of the combustor with acoustic control for a liquid-fueled combustor, see Figure 8.12. Moreover, for the case with primary and secondary speakers having a common driving signal as shown in Figure 9.1. Now, the generalized plant $G(s)$ for the $\mathcal{H}_\infty$ control problem is given by

$$G(s) = \left[\begin{array}{c|c} W_z H_{open-loop} & W_z H_{primsec} \\ 0 & \beta \\ \hline H_{open-loop} & H_{primsec} \end{array}\right]$$

where W_z is a weighting function to stress the working condition

$$W_z(s) = \frac{1.234 \times 10^6 (s + 0.6283)}{(s + 314.2)(s^2 + 314.2s + 2.467 \times 10^6)}$$

and β is the control penalty imposed to regularize the problem. In this problem, $order(M_\infty)$ is 29. Since the setup in Figure 9.1 presents a disturbance attenuation problem, it is well known that the optimal controller tends to invert $H_{open-loop}$ which is non-minimum phase. So, the optimal solution produces an unstable controller. The computational results are summarized in Table 9.2. For the two tested β's, there was no $\gamma > 0$ that could lead to a stable central controller. An improvement on γ, ranging from 50% to 70%, was observed during the control design by using the suggested approach with weighting function. Moreover, it is shown that the order of the controller can be drastically reduced while still maintaining the closed-loop performance. Note that the addition of the weighting function in the controller design is not noticeable in the final controller order.

Table 10.2: Example 2, Computational Results.

β	**Weight**	γ	**order** $\mathcal{F}_l(M_\infty, Q)$	$\|T_{zw}\|_\infty$	**order** $\hat{Q}$	**order** $\hat{K}$	$\|T_{zw}\|_\infty$
1.0	YES	4.75	85	2.8098	8	16	3.1039
($\gamma_{opt} = 1.2964$)	NO	9.5	55	7.8000	8	28	7.36
2.0	YES	2.9	85	2.8760	17	24	2.8780
($\gamma_{opt} = 1.7365$)	NO	6.5	55	3.4980	6	21	3.3041

CHAPTER 11

CONCLUSIONS

The overall results presented in this dissertation show a major progress in the suppression of thermoacoustic instabilities in combustion chambers. It is important to mention that this is the first successful application of model-based optimal controllers to large size liquid and gaseous fueled combustors (> 100kW). The results so far published in literature were mainly simulations and only an application to a small-size combustor (1kW) was reported.

The combustor system is clearly a complex nonlinear system; especially in an unstable condition (high pressure pulsations). However, linear identification techniques based on acoustic characterizations (pressure measurements) were able to provide the basic dynamics of the instability coupling needed for model-based control design. Obviously, these linear models are only valid for the combustor operating condition used in the identification process.

In the gaseous fueled application, the identification scheme based on the Riemann-Invariants showed to give a good description of the instability mechanism in the combustor. Linear $\mathcal{H}_\infty$ controllers were capable of attenuating the pressure pulsations effectively in the experimental rig. In addition, simple controllers optimized via an evolution algorithm also proved to be a good alternative in combustion control. These resulting controllers are simple and sometimes perform as well or better than model-based techniques. It is shown that the frequency characteristics of these optimized controllers resembled the dynamics of the $\mathcal{H}_\infty$ controllers around the in-

stability frequency. Overall there were clear improvements with these proposed techniques compared to classical phase-delay control. Furthermore, $\mathcal{H}_\infty$ controllers could attenuate the pressure pulsations in the chamber for a range of different operating conditions of the combustor test-rig. Therefore, active control using proportional fuel modulation showed to be a viable strategy for large scale combustors.

The liquid fueled application reported particular features. Linear and time-invariant controllers such as LQG and $\mathcal{H}_\infty$ were tested successfully. However, model-based controllers implemented using fuel modulation with automotive fuel injectors did not present clear improvements over phase-delay control. Contrary to this, acoustic modulation with loudspeakers presented noticeable advantages with model-based techniques over the baseline phase-delay control. As a result, it can be argued that the lack of proportional response of fuel injectors is limiting the performance of active control strategies in liquid fueled combustors; the advantages of model-based controllers were almost lost. On the other hand, a new control configuration in the test-rig proved that with only a small amount of control fuel the pressure pulsations could be largely attenuated. Consequently, the location of the control fuel played an important role in the effectiveness of the control actuation. These last results leave an open door to continue the research work in this field.

In addition, during the controller synthesis a problem was addressed: optimal control strategies could lead to unstable controllers. Obviously, this feature is not desirable in practical applications due to high sensitivity and lack of robustness in the presence of nonlinearities in the system. An alternative approach was suggested for the $\mathcal{H}_\infty$ Strong Stabilization problem. This algorithm showed advantages in the achievable closed-loop performance.

REFERENCES

[1] D. Allgood. Active Control of Thermoacoustic Instabilities, Master's Thesis, Mechanical Engineering Department at LSU, Baton Rouge, December 2000.

[2] A.M. Annaswamy and A.F. Ghoniem. Active Control in Combustion Systems, *IEEE Control Systems*, pp. 49-63, December 1995.

[3] A.M. Annaswamy, M. Fleifil, J.P. Hathout and A.F. Ghoniem. Impact of Linear Coupling on the Design of Active Controllers for Thermoacoustic Instability, *Combust. Sci. Tech* , Vol. 128, pp. 131-180, 1997.

[4] A.M. Annaswamy, M. Fleifil, J.W. Rumsey, R. Prasanth, J.P. Hathout and A.F. Ghoniem. Thermoacoustic Instability: Model-Based Optimal Control Designs and Experimental Validation, *IEEE Transactions on Control Systems Technology*, Vol. 8, No. 6, November 2000.

[5] G.J. Balas, J.C. Doyle, K. Glover, A. Packard and R. Smith. *μ-Analysis and Synthesis Toolbox: User's Guide*, The MathWorks Inc., 1998.

[6] L.L. Beranek and I.L. Ver. *Noise and Vibration Control Engineering: Principles and Applications*, John Wiley & Sons, Inc., 1992.

[7] D.S. Bernstein and W.M. Haddad. LQG Control with and $\mathcal{H}_\infty$ Performance Bound: A Riccati Equation Approach, *IEEE Transactions on Automatic Control*, Vol. 34, No. 3, pp. 293-305, March 1989.

[8] G.J. Bloxsidge, A.P. Dowling and P.J. Langhorne. Reheat Buzz: An Acoustically Coupled Combustion Instability, Part 2: Theory, *J. Fluid Mech*, Vol. 193, pp. 445-473, 1988.

[9] G.J. Bloxsidge, A.P. Dowling, N. Hooper and P.J. Langhorne. Active Control of Reheat Buzz, *AIAA Journal*, Vol. 26, No. 7, July 1988.

[10] G.E.P. Box. Evolutionary operation- a method for increasing industrial productivity, *Appl. Stat.*, Vol. 6, pp. 81-101, 1957.

[11] S.M. Candel. Combustion Instabilities Coupled by Pressure Waves and Their Active Control, *Twenty-Fourth Symposium on Combustion*, pp. 1277-1296, 1992.

[12] J.C. Chen, K. Zhou, and B.C. Chang. Closed-loop controller reduction by a structured truncation approach, *Proceedings of the 33rd Conference on Decision and Control*, Lake Buena vista, Florida, pp. 2726-2731, December 1994.

[13] Y. Choi and W.K. Chung. On the Stable $\mathcal{H}_\infty$ Controller Parameterization under Sufficient Condition, Submitted to *IEEE Transactions on Automatic Control*, 2000.

[14] Y.C. Chu, A.P. Dowling and K.Glover. Robust Control of Combustion Oscillation, *IEEE International Conference on Control Applications*, Trieste, Italy, September 1998.

[15] J.F. Cohen, N.M. Rey, C.A. Jacobson and T.J. Anderson. Active Control of Combustion Instability in a Liquid-Fueled Low-NOx Combustor, *International Gas Turbine and Aeroengine Congress and Exhibition*, June 2-5, 1998.

[16] F. Culick. Nonlinear Behavior of Acoustic Waves in Combustion Chambers, *Acta Astronautica*, Vol. 3, pp. 715-756, 1976.

[17] F.E.C. Culick. Combustion Instabilities in Liquid-Fueled Propulsion Systems - An Overview, *AGARD Conference on Combustion Instabilities in Liquid-Fueled Propulsion Systems*, Bath, 1988.

[18] P. Cvitanovic. Universality in Chaos, *Institute of Physics Publishing, Bristol and Philadelphia*, Second Edition 1996.

[19] A.P. Dowling. Nonlinear Self-Excited Oscillations of a Ducted Flame, *Journal of Fluid Mechanics*, Vol. 346, pp. 271-290, 1997.

[20] A.P. Dowling. A Kinematic Model of a Ducted Flame, *Journal of Fluid Mechanics*, 1999.

[21] J.C. Doyle, K. Glover, P. Khargonekar and B. Francis. State-space solutions to standard H_2 and $\mathcal{H}_\infty$ control problems, *IEEE Transactions on Automatic Control*, Vol. 34, No. 8, pp. 831-847, 1989

[22] S.M.N. Evesque and A.P. Dowling. Adaptive Control of Combustion Oscillations, *4th AIAA/CEAS Aeroacoustics Conference*, June 2-4, 1998.

[23] M. Fleifil, A.M. Annaswamy, Z.A. Ghoneim and A.F. Ghoniem. Response of a Laminar Premixed Flame to Flow Oscillations: A Kinematic Model and Thermoacoustic Instability Results, *Combustion and Flame* , Vol. 106, pp. 487-510, 1996.

[24] M. Fleifil, A.M. Annaswamy, J.W. Rumsey, A. Kojic and A.F. Ghoniem. A Physically Based Nonlinear Model of Combustion Instability and Active Control, *Proceedings of the 1998 IEEE International Conference on Control Applications*, September 1-4, 1998.

[25] M. Fleifil, A.M. Annaswamy, J.P. Hayhout and A.F. Ghoniem. Reduced-Order Dynamic Models for Control of Reactive Fluid-Flows, *Proceedings of the 38th Conference on Decision and Control*, December, 1999.

[26] Y.T. Fung, V. Yang and A. Sinha. Active Control of Combustion Instabilities with Distributed Actuators, *Combust. Sci. and Tech.*, Vol. 78, pp. 217-245, 1991.

[27] Y.T. Fung and V. Yang. Active Control of Nonlinear Pressure Oscillations in Combustion Chambers, *Journal of Propulsion and Power*, Vol. 8, No. 6, pp. 1282-1289, 1992.

[28] A. Grace, A.J. Laud, J.N. Little and C.M. Thompson. *Control System Toolbox: User's Guide*, The MathWorks Inc., 1992.

[29] I. Glassman. *Combustion*, Academic Press, San Diego, CA 1996.

[30] D. Gstohl. Thermoacoustic Characterization of a Premixed-Burner, Diplomarbeit, Eidgenossische Technische Hochschule Zurich, Institut fur Energietechnik-LVV, February 2000.

[31] A. Gulati and R. Mani. Active Control of Unsteady Combustion-Induced Oscillations, *Journal of Propulsion and Power*, Vol. 8, No. 5, pp. 1109-1115, 1992.

[32] E. Gutmark, K.J. Wilson, K.C. Schadow, R.A. Stalnaker, R.A. Smith. Combustion Characteristics and Passive Control of an Annular Dump Combustor, *AIAA Paper* 93-1772, 1993.

[33] E.J. Gutmark, T.P. Park, K.J. Wilson, K.H. Yu, R.A. Smith, D.M. Hanson-Parr and K.C. Schadow. Compact Waste Incinerator Based on Vortex Combustion, *Combust. Sci. and Tech.*, Vol. 121, pp. 333-349, 1996.

[34] J.P. Hathout, M. Fleifil, J.W. Rumsey, A.M. Annaswamy and A.F. Ghoniem. Model-Based Analysis and Design of Active Control of Thermoacoustical Instability, *Proceedings of the 1997 IEEE International Conference on Control Applications*, October 5-7, 1997.

[35] E.W. Hendricks and K.C. Schadow. Recent Progress in the Implementation of Active Combustion Control, 1992.

[36] J.R. Hibshman, J.M. Cohen, A. Banaszuk, T.J. Anderson and H.A. Alholm. Active Control of Combustion Instability in a Liquid-Fueled Sector Combustor, *International Gas Turbine and Aeroengine Congress and Exhibition*, June 7-10, 1999.

[37] B. Hong, A. Ray and V. Yang. Robust Feedback Control of Combustion Instability, *Proceedings of the American Control Conference*, June, 1998.

[38] S.A. Klein and J.B.W. Kok. Acoustic Instabilities in SynGas Fired Combustion Chambers, *International Gas Turbine and Aeroengine Congress and Exhibition*, June 7-10, 1999.

[39] S.A. Klein. *On the Acoustics of Turbulent Non-premixed Flames*, Ph.D. Thesis, University of Twente, Netherlands, February, 2000.

[40] M. Krstic, A. Krupadanam, C.A. Jacobson. Self-Tuning Control of a Nonlinear Model of Combustion Instabilities, *Proceedings of the 1997 IEEE International Conference on Control Applications*, October 5-7, 1997.

[41] P.J. Langhorne, A.P. Dowling and N. Hooper. Practical Active Control System for Combustion Oscillations, *Journal of Propulsion*, Vol. 6, No. 2, pp. 324-333, 1990.

[42] A.H. Lefebvre. *Gas Turbine Combustion*, Taylor & Francis, Philadelphia, PA 1998.

[43] F.L. Lewis and V.L. Syrmos. *Optimal Control*, Jonh Wiley & Sons Inc., 1995.

[44] T. Lieuwen, H. Torres, C. Johnson and B.T. Zinn. A Mechanism of Combustion Instability in Lean Premixed Gas Turbine Combustors, *International Gas Turbine and Aeroengine Congress and Exhibition*, June 7-10, 1999.

[45] L. Ljung. *System Identification Toolbox: User's Guide*, The MathWorks Inc., 1991.

[46] G.H. Markstein. *Nonsteady Combustion Propagation*, The Macmillan Company, Pergamon Press. Oxford, England 1964.

[47] K.R. McManus, T. Poinsott, and S.M. Candel. A Review of Active Control of Combustion Instabilities, *Progress in Energy and Combustion Science*, Vol. 19, pp. 1-29, 1993.

[48] K.R. McManus, J.C. Magill, M.F. Miller and M.G. Allen. Closed-Loop System for Stability Control in Gas Turbine Combustors, *35th Aerospace Sciences Meeting and Exhibit*, January 6-10, 1997.

[49] R.M. Murray, C.A. Jacobson, R. Casas, A.I. Khibnik, C.R. Johnson Jr., R. Bitmead, A.A. Peracchio and W.M. Proscia. System Identification for Limit Cycling Systems: A Case Study For Combustion Instabilities, *Proceedings of the American Control Conference* , pp. 2004-2008, June, 1998.

[50] S. Murugappan, S. Acharya, E. Gutmark and T. Messina. Characteristics and Control of Combustion Instabilities in a Swirl-Stabilized Spray Combustor, *35th AIAA/ASME/SAE/ASEE Joint Propulsion Conference and Exhibit*, June 20-24, 1999.

[51] T. Myint-U and L. Debnath. *Partial Differential Equations for Scientists and Engineers*, Prentice Hall, 1987.

[52] Y. Neumeier and B.T. Zinn. Active Control of Combustion Instabilities Using Real Time Identification of Unstable Combustor Modes, *IEEE* 0-7803-2550-8, 1995.

[53] Y. Neumeier and B.T. Zinn. Active Control of Combustion Instabilities with Real Time Observation of Unstable Combustor Modes, *34th Aerospace Sciences Meeting and Exhibit*, January 15-18, 1996.

[54] Y. Neumeier, N. Markopoulos and B.T. Zinn. A Procedure for Real-Time Mode Decomposition, Observation, and Prediction for Active Control of Combustion Instabilities, *Proceedings of the 1997 IEEE International Conference on Control Applications*, October 5-7, 1997.

[55] C.O. Paschereit and W. Polifke. Investigation of the Thermoacoustic Characteristics of a Lean Premixed Gas Turbine Burner, *ASME Turbo Expo '98*, June 2-5, 1998.

[56] C.O. Paschereit, E. Gutmark and W. Weisenstein. Flow-Acoustic Interactions as a Driving Mechanism for Thermoacoustic Instabilities, *4th AIAA/CEAS Aeroacoustics Conference*, June 2-4, 1998.

[57] C.O. Paschereit, E. Gutmark and W. Weisenstein. Acoustic Control of Combustion Instabilities and Emissions in a Gas-Turbine Combustor, *Proceedings of the 1998 IEEE International Conference on Control Applications*, September 1-4, 1998.

[58] C.O. Paschereit, E. Gutmark, W. Weisenstein. Control of Thermoacoustical Instabilities in a Premixed Combustor by Fuel Modulation, *37th AIAA Aerospace Sciences Meeting and Exhibit*, January 11-14, 1999.

[59] C.O. Paschereit. B.B.H. Schuermans, W. Polifke and O. Mattson. Measurement of Transfer Matrices and Source Terms of Premixed Flames, *ASME Turbo Expo '99*, June 7-10, 1999.

[60] G. Pask. Physical and Linguistic Evolution in Self-Organizing Systems, *Proceedings of the 1st. IFAC Symposium on Optimization and Adaptive Control*, April 1962, pp. 199-227.

[61] A.A. Peracchio and W.M. Proscia. Nonlinear Heat-Release/Acoustic Model for Thermoacoustic Instability in Lean Premixed Combustors, *International Gas Turbine and Aeroengine Congress and Exhibition*, June 2-5, 1998.

[62] S.L. Rayleigh. *Theory of Sound II*, Dover Publications, Second Edition, Vol. 2, June 1976.

[63] I. Rechenberg. *Evolutionsstrategie*, Stuttgart, Germany 1973.

[64] G.A. Richards and M.C. Janus. Characterization of Oscillations During Premix Gas Turbine Combustion, *International Gas Turbine and Aeroengine Congress and Exhibition*, June 2-5, 1997.

[65] G. Roy. *Propulsion Combustion: Fuels to Emissions*, Taylor & Francis, Bristol, PA 1998.

[66] S.S. Sattinger, D.J. Amos, D.D. Darling, Y. Neumeier, A. Nabi and B.T. Zinn. Sub-Scale Demonstration of the Active Feedback Control of Gas-Turbine Combustion Instabilities, *International Gas Turbine and Aeroengine Congress and Exhibition*, June 2-5, 1998.

[67] H.P. Schwefel. *Evolution and Optimum Seeking*. John Wiley & Sons, Inc., 1995.

[68] B.B.H. Schuermans, C.O. Paschereit, W. Polifke, and J.H. van der Linden. Prediction of the acoustic pressure spectra in Gas Turbines based on measured transfer matrices, *ASME Turbo Expo '00*, May 8-11, 2000.

[69] M.A. Schumer and K. Steiglitz. Adaptive Step Size Random Search, *IEEE Trans.* AC-13, pp. 270-276, 1968.

[70] R. Smith, A. Banaszuk and G. Dullerud. Model Validation Approaches for Nonlinear Feedback Systems using Frequency Response Measurements, *Proceedings of the 38th Conference on Decision and Control*, December 1999.

[71] J.R. Stephens, S. Acharya and E.J. Gutmark. Controlled Swirl-Stabilized Spray Combustor, *35th Aerospace Sciences Meeting and Exhibit*, January 6-10, 1997.

[72] N. Syred and J.M. Beer. Combustion in Swirling Flows: A Review, *Combustion and Flame*, Vol. 23, pp. 143-201, 1974.

[73] B. van Roon. *Modeling of Lean Premixed Combustion Acoustics*, Diploma Thesis Report, The Process and Energy Department of the Technical University of Delft, Netherlands, June 2000.

[74] M. Vidyasagar. *Control System Synthesis: A Factorization Approach.* Cambridge, MA, MIT Press, 1985.

[75] G. Wang, V. Sreeram and W.Q. Liu. Balanced Performance Preserving Controller Reduction, Preprint, University of Western Australia, Nedlands, Australia, 2000.

[76] V. Yang, A. Sinha and Y.T. Fung. State-Feedback Control of Longitudinal Combustion Instabilities, *Journal of Propulsion*, pp. 66-73, Jan-Feb. 1992.

[77] D.C. Youla, J.J. Bongiorno and N.C. Lu. Single-loop Feedback Stabilization of Linear Multivariable Dynamical Plants, *Automatica*, Vol. 10, pp. 159-173, 1974.

[78] M. Zeren and H. Özbay. On Stable $\mathcal{H}_\infty$ Controller Design. *Proceedings of the American Control Conference*, Albuquerque, New Mexico, pp. 1302-1306, June 1997.

[79] M. Zeren and H. Özbay. On the Synthesis of Stable $\mathcal{H}_\infty$ Controllers, *IEEE Transactions on Automatic Control*, Vol. 44, No. 2, pp. 431-435, February 1999.

[80] K. Zhou and J. C. Doyle. *Essentials of Robust Control*, Prentice-Hall Inc., 1998.

VITA

The author, Daniel Campos-Delgado, was born on October 14^{th} of 1973 in San Luis Potosi, Mexico. He received his bachelor of science degree with a major in electronics from the University of San Luis Potosi, Mexico, in March of 1996. He joined the Graduate Program at the Louisiana State University in August 1996 and obtained a master of science degree in electrical engineering in May of 1999. He is currently a candidate for the degree of Doctor of Philosophy.

DOCTORAL EXAMINATION AND DISSERTATION REPORT

Candidate: Daniel Campos-Delgado

Major Field: Electrical Engineering

Title of Dissertation: Active Control of Thermoacoustical Instabilities

Approved:

Major Professor and Chairman

Dean of the Graduate School

EXAMINING COMMITTEE:

Date of Examination:

03/20/01